UNIVERSITY OF CALIFORNIA,
IRVINE

# The Thermochemical Degradation of Hot Section Materials for Gas Turbine Engines in Alternative-Fuel Combustion Environments

DISSERTATION

submitted in partial satisfaction of the requirements
for the degree of

DOCTOR OF PHILOSOPHY

in Materials Science and Engineering

by

Timothy Montalbano

Dissertation Committee:
Professor Daniel R. Mumm, Chair
Professor James Earthman
Professor Timothy J. Rupert

2015

## DEDICATION

**To my family…**
For providing an environment during my childhood and adolescence that allowed me to discover and nurture an interest in science. Thank you for your encouragement of my academic pursuits both before and during my graduate work.

**To my wife Regina…**
Who has had to undergo many nights, weekends, and activities alone so that I could accomplish my work for this dissertation. She stood by me and supported me tremendously during the past five years. Thank you for your patience and understanding during this stressful and time-intensive process.

## TABLE OF CONTENTS

## LIST OF FIGURES

## ACKNOWLEDGEMENTS

I would like to thank my advisor Professor Daniel Mumm for allowing me to join his group and perform research in his lab. I thank him for providing the financial support and lab resources to perform this research. In addition, his constructive criticism of my work has helped me grow as a scientist.

I would like to thank Dr. Jian-Guo Zheng for allowing me to be an assistant in The Laboratory for Electron and X-ray Instrumentation (LEXI). This provided a means to additional financial support as well as a way to learn advanced electron microscopy techniques. Also, he took the time to have several one-on-one sessions with me outside of a formal training that allowed me to understand many high-level techniques.

In a similar fashion, I would like to thank Dr. Qiyin Lin who went above and beyond his role as a staff scientist in helping me understand the complex phenomena involved in several characterization techniques. I will miss having such a friendly and patient expert to discuss matters related to x-rays and photoelectrons.

I would like to thank the members of the Mumm group who came before me and paved the way for a lot of the work performed here. In particular, Dr. Matthew Weeks, Joe Horwath, and Randall Schubert designed, built, and set-up the burner rig used to generate some of the results in this dissertation. Also, Dr. Matthew Sullivan's design and set-up of a furnace to perform thermal exposure of samples in humid environments was the model used to perform the humid exposures in this dissertation. His procedures for performing humid environment testing were also largely implemented in this dissertation.

I would like to thank program manager Patcharin Burke of the Department of Energy (cooperative agreement # DE-FE0004727) and program manager Dr. David Schiffler of the Office of Naval Research (contract N00014-10-1-0591 and N00014-08-1-1172) for providing partial funding for the work in this dissertation.

A special thanks to Dr. Lou Aprigliano for taking the time to show me techniques related to the evaluation of materials after exposure in the burner rig. Also, I would like to thank Dr. Martha Mecartney for offering critiques of my research and advice about future work to pursue.

I would like to thank my family for their love and constant encouragement of me to pursue my dreams. They helped instill in me the work ethic and toughness required to make it through the rigors of obtaining this doctorate.

I can not thank my wife Regina enough for her unwavering support during this time taken to achieve my doctorate. She has helped me in innumerable ways and has had to sacrifice so much so that I could perform the work in this dissertation. I am truly indebted to her and could not have made it through this long journey without her.

# CURRICULUM VITAE

## TIMOTHY J. MONTALBANO

**Current Address**
6206 Adobe Cir
Irvine, CA 92617

**Contact Info**
Cell Phone: 631-742-9111
tmontalb@uci.edu

**Education**

**University of California, Irvine (UCI), Fall 2010 – Fall 2015, Ph.D.**
- Materials Science and Engineering, PI: Dr. Daniel Mumm, Cumulative GPA: 3.95

**Villanova University, Fall 2004 - Spring 2010, B.S. and M.S., Mechanical Engineering**
- M.S. Cumulative GPA: 3.63, B.S. Cumulative GPA: 3.36

**Ph.D. Research Projects**

**Controlled Environment Aging of Air Plasma Sprayed (APS) 8 wt% Yttria-Stabilized Zirconia (YSZ), October 2013 - Present**
- APS 8YSZ was aged above 2400 °F at varying times in either a dry $O_2/N_2$ environment or in a humid $O_2/N_2$ environment with 45% water vapor content.

- Humid-aged samples showed an increased rate of decomposition of the parent *t'* phase relative to that of the dry-aged sample as shown by Rietveld refinement of XRD spectra and Raman spectroscopy.

- Scanning transmission electron microscopy and transmission electron microscopy analysis are currently being used to determine the role of 8YSZ domain sizes on the stability of the *t'* phase in different environments.

**Low Velocity Burner Rig (LVBR) Design and Experimentation, August 2012 - Present**
- The LVBR was designed and built in collaboration with the Mumm group and staff members of the Advanced Power and Energy program at UCI. This test rig was funded by the Office of Naval Research to study the material degradation characteristics of hot-section gas turbine components in a combustion environment.

- The LVBR is capable of combusting fuel into a furnace heating up to 27 rotating samples that can be thermally cycled out of the hot zone by a custom-made LabVIEW program.

- Two 700 h tests were carried out to certify a renewable diesel fuel that was proposed to be used in the United States Navy.
    - Imaging, chemical analysis, and measurements on the extent of corrosive attack on industry-grade turbine coatings were performed to evaluate

differences in degradation between the proposed fuel and the conventional fuel used in Navy surface ships.

- A second LVBR is currently being designed and built to simulate turbine engine combustion conditions ranging from hot corrosion to oxidizing environments.

**Extracurricular Activities**

**Laboratory for Electron and X-ray Instrumentation (LEXI), July 2013 – Present**

- Perform electron microscopy analysis for local industry clientele—e.g. IJ Research, Henkel Electronics, Biostructures, and Glidewell Laboratories.
    - The analysis includes backscatter imaging, chemical analysis using energy dispersive x-ray spectroscopy, and focused ion beam milling to image sub-surface features

- Train academic and industry personnel for performing imaging and chemical analysis on high resolution scanning and transmission electron microscopes.
    - The instruments I have trained users on include:
        - FEI Magellan 400 XHR SEM
        - FEI Quanta 3D FEG Dual Beam
        - FEI/Philips CM-20 conventional TEM

**Graduate InterConnect Peer Mentor, June 2013 – October 2014**

- Provided support to international graduate students transitioning to graduate school at UCI by providing sessions for English instruction, helping students secure housing, sending out weekly informational e-mails about graduate life at UCI, and answering questions in regards to the procedures and policies of the School of Engineering.

**Graduate Student Association, ChEMS Department, September 2012 – June 2013**

- Served as an Ambassador to the Faculty by identifying and raising concerns of the graduate community at faculty departmental meetings.

- Created and conducted a poll of ChEMS graduate student about the state of graduate education in the department and co-presented the results to an Academic and Industrial Advisory Committee.
    - The Committee evaluated the research and teaching merits of the ChEMS department partly based on our presentation and reported their evaluation to the Dean of Engineering.

**ASM International, Society for Materials Scientists and Engineers, July 2011 – July 2013**

- Served as an executive committee member in the Orange Coast Chapter.

- Planned and organized an ASM International-sponsored symposium on materials challenges in aerospace fasteners in the fall of 2012.

- Planned the 2011 Symposium on *Biomaterials, Medical Devices and Tools:* Challenges *with Design, Fabrication and Testing* and ran the associated poster competition for this symposium.
- Planned and attended monthly group meetings hosting industry and academic speakers from the materials science community.

**Papers**

- Montalbano, T.J. , Horwath, J.P. , Mumm, D.R., Accelerated Aging of Yttria-Stabilized Zirconia Thermal Barrier Coatings in High Water Vapor Content, Elevated Temperature Environments: X-Ray Diffraction and Raman Spectroscopy Measurements, *J. Am. Ceram*, In Progress

- Montalbano, T.J. , Horwath, J.P. , Mumm, D.R., Accelerated Aging of Yttria-Stabilized Zirconia Thermal Barrier Coatings in High Water Vapor Content, Elevated Temperature Environments: STEM and TEM Analysis, *J. Am. Ceram*, In Progress

- Montalbano, T.J., McDonell, V., Mumm, D.R., Burner Rig Evaluation of the Type I Hot Corrosion of Marine Gas Turbine Coatings in Traditional and Synthetic-Blend Fuel Combustion Environments, *Surface & Coatings Technology*, In Progress

**Presentations/Posters**

- Presentation: Aging of Yttria-Stabilized Zirconia in Controlled Environments, *Materials Science & Technology*, Pittsburgh, PA, October 15$^{th}$, 2014 [T. J. Montalbano, J.P. Horwath, and D.R. Mumm]

- Poster: Hot Corrosion of Shipboard Turbine Components in a Low Velocity Burner Rig Using Alternative Fuels, *Engineering Conferences International Series: Thermal Barrier Coatings IV*, Irsee, Germany, June 25$^{th}$, 2014 [T. J. Montalbano and D. R. Mumm]

- Presentation: Hot Corrosion of Shipboard Turbine Components in High Water Vapor Combustion Environments, *Materials Science & Technology*, Montreal, Canada, October 29$^{th}$, 2013 [T. J. Montalbano, J. P. Horwath, and D. R. Mumm]

- Presentation: Evaluation of CMAS Reactivity with Ceramic Oxides for Thermal Barrier Coating Applications, *The Minerals, Metals & Materials Society*, San Antonio, TX, March 5$^{th}$, 2013 [T. J. Montalbano, J. P. Horwath, M. H. Sullivan, D. R. Mumm]

- Poster: Evaluation of CMAS Reactivity with Ceramic Oxides for Thermal Barrier Coating Applications, *University Turbine Systems Research Workshop*, University of California, Irvine, CA, October 2$^{nd}$, 2012 [Ç. B. Iyi, T. J. Montalbano, M. H. Sullivan, M. L. Mecartney, J. P. Horwath and D. R. Mumm]

**Awards**

**2013 TMS International Symposium on Superalloys Scholarship, July 2013**

- One of two students selected nationwide to be awarded this $2,000 scholarship for research on high-performance materials used in the gas turbine industry.

**Awarded a TMS Student Travel Grant to Attend the 2013 Materials Science & Technology (MS&T) Conference, July 2013**

- One of thirteen students nationwide to receive a $350 grant to travel to and attend the 2013 MS&T conference in Montreal, Canada.

**Awarded Best Student Poster at the 2013 Southern California Society for Microscopy and Microanalysis (SCSMM), March 2013**

**Measurement Science Conference Scholarship Recipient, March 2012**

- Awarded a $2,000 scholarship for my experience and accomplishments in the application and advancement of measurement science and technology.

**Graduate Student Research and Travel Grant Recipient, February 2012**

- Awarded a $500 grant from The Henry Samueli School of Engineering at UCI to pursue professional travel opportunities related to research activities.

## ABSTRACT OF THE DISSERTATION

The Thermochemical Degradation of Hot Section Materials for

Gas Turbine Engines in Alternative-Fuel Combustion Environments

By

Timothy Montalbano

Doctor of Philosophy in Materials Science & Engineering

University of California, Irvine, 2015

Professor Daniel R. Mumm, Chair

Gas turbine engines remain an integral part of providing the world's propulsion and power generation needs. The continued use of gas turbines requires increased temperature operation to reach higher efficiencies and the implementation of alternative fuels for a lower net-carbon footprint. This necessitates evaluation of the material coatings used to shield the hot section components of gas turbines in these new extreme environments in order to understand how material degradation mechanisms change. Recently, the US Navy has sought to reduce its use of fossil fuels by implementing a blended hydroprocessed renewable diesel (HRD) derived from algae in its fleet. To evaluate the material degradation in this alternative environment, metal alloys are exposed in a simulated combustion environment using this blended fuel or the traditional diesel-like fuel. Evaluation of the metal alloys showed the development of thick, porous scales with a large depletion of aluminum for the blend fuel test. A mechanism linking an increased solubility of the scale to the blend fuel test environment will be discussed.

For power generation applications, Integrated Gasification Combined Cycle (IGCC) power plants can provide electricity with 45% efficiency and full carbon capture by using a synthetic gas (syngas) derived from coal, biomass, or another carbon feedstock. However, the

combustion of syngas is known to cause high water vapor content levels in the exhaust stream with unknown material consequences. To evaluate the effect of increased humidity, air-plasma sprayed (APS), yttria-stabilized zirconia (YSZ) is thermally aged in an environment with and without humidity. An enhanced destabilization of the parent phase by humid aging is revealed by x-ray diffraction (XRD) and Raman spectroscopy. Microstructural analysis by transmission electron microscopy (TEM) and scanning-TEM (STEM) indicate an enhanced coarsening of the domain structure of the YSZ in the humid environment. The enhanced destabilization and coarsening in the humid aging environment is explained mechanistically by water-derived species being incorporated into the YSZ structure and altering the anion sublattice. The characterization of the metal alloy and ceramic coatings exposed in these alternative environments allows for a deeper understanding of the mechanisms behind the material evolution in these environments.

# 1. Chapter 1: Introduction

## 1.1 The Protection of Hot Section Components in Gas Turbines

Gas turbine engines play a significant role in modern transportation and power generation needs. Gas turbines are responsible for meeting the propulsion needs of civilian and military aircraft, helicopters, and many ships worldwide. Gas turbines also generate one-fifth of the world's electricity as well as one-quarter of the United States' electricity [1]. Their wide-spread use is in part due to their favorable combination of high power output and efficiency in relation to other power generation systems as shown in Fig. 1.1. The drive to improve the efficiency of the gas turbine engine is dictated by the Carnot efficiency as shown in Eq. 1.1.

$$\mu_C = (T_i - T_o) / T_i \qquad \text{[Eq. 1.1]}$$

Here $\mu_C$ is the efficiency of the Carnot cycle, $T_i$ is the temperature at the engine inlet, and $T_o$ is the temperature at the engine exhaust. As the temperature at the engine inlet is limited by the ambient conditions of the engine's location, all that can be done to increase the efficiency of the gas turbine is to increase the temperature at which the engine operates. The effect of increasing the temperature on gas turbine efficiency is significant, as an increase in temperature by 100°F will result an increase of 1.5% in efficiency [2]. Thus, there is a constant push in the gas turbine community to increase the engine operation temperature.

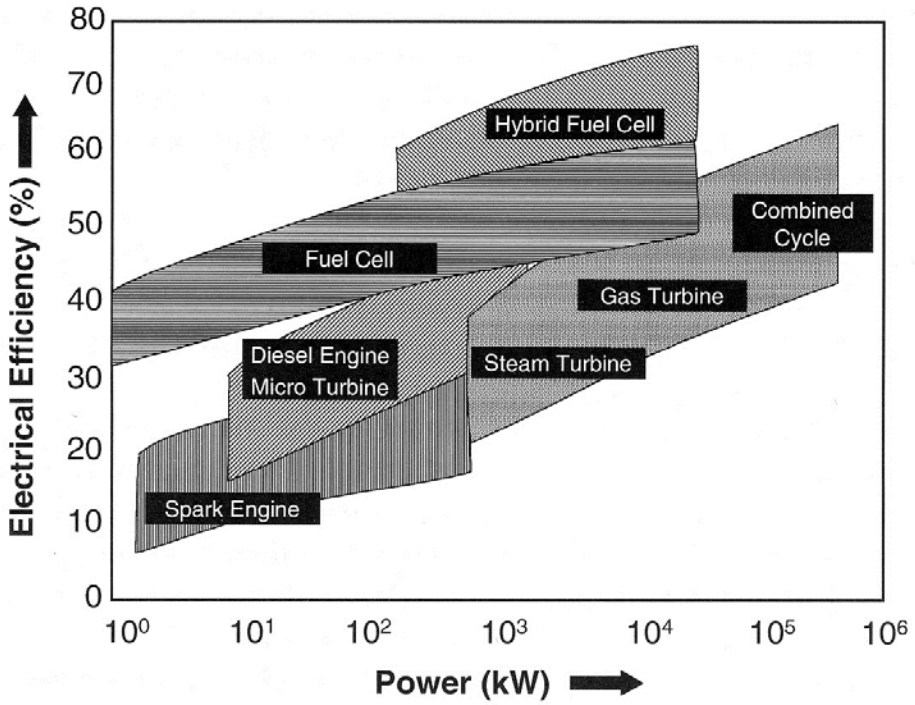


**Figure 1.1 The electrical efficiency of power generation systems as a function of power output.**

In order to understand the relation between gas turbine efficiency and material reliability, it is necessary to understand how a gas turbine can transfer energy. A gas turbine pulls in air at its inlet and compresses it through a succession of rotating blades—as shown in Fig. 1.2— in order to increase the pressure of the air. A liquid or gaseous fuel is then introduced into the high-pressure gas in a specific ratio depending on the application and combusted in order to increase the temperature of the high-pressure gas. The acceleration and expansion of the combusted gases is captured by the rotating turbine blades downstream to perform thermodynamic work. The transfer of energy from the combustion gases to rotational energy—for either power or propulsion applications— requires the use of protective coatings for the hot section materials. These hot section materials must be able to withstand the high temperatures and extreme environments of the combustion gases in order to allow the transfer of energy to the rotating

shaft of the engine. The coatings used on the hot section materials of gas turbine engines are known as thermal barrier coatings or TBCs. TBCs are therefore vital to the efficiency of gas turbine engines and the continued use of these engines in both power generation and propulsion applications.

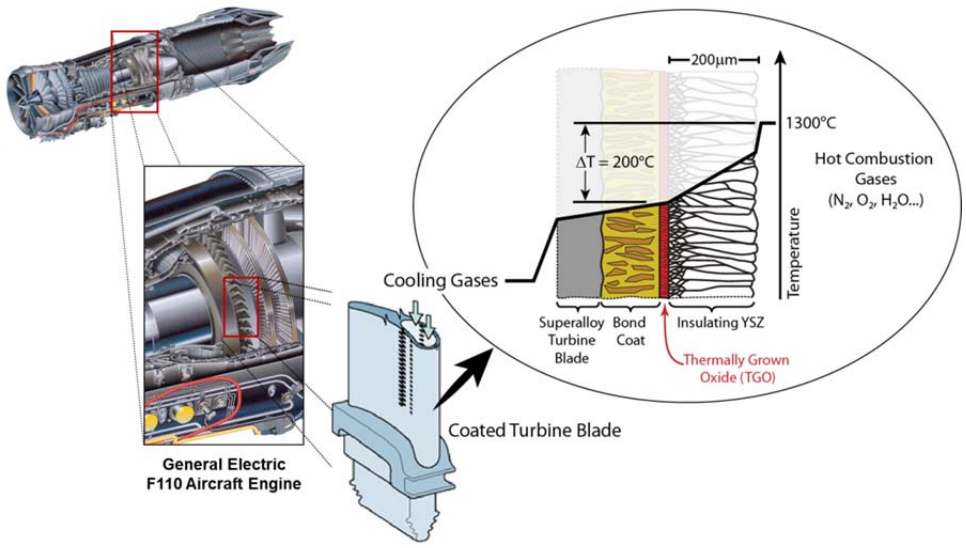


**Figure 1.2 A schematic of the TBC system on the turbine blade as it relates to its location in an aero-turbine engine.**

The demand for higher efficiency has also come with the implementation of alternative fuel sources to replace the traditional fossil fuels used in both power generation and propulsion gas turbine engines. Commercial partnerships with the National Energy Technology Laboratory (NETL) have implemented integrated gasification combined cycle (IGCC) power plants in the United States as a means to provide efficient power generation with a low carbon footprint. IGCC power plants can take feedstock derived from biomass or coal and refine it into a synthetic gas (syngas) that can be used in power generation turbines. The efficiency of the power generation conversion with syngas can be 45% with full carbon capture from the exhaust system.

However, a study done by NETL indicates that the use of syngas in gas turbines causes an increase in the water vapor content of the combustion stream [3]. The combustion of syngas coupled with the injection of steam to suppress $NO_x$ emissions can cause up to a four-fold increase in water content compared with the combustion of traditional natural gas. Increased water vapor or humidity can influence the stability of the hot section materials at temperatures relevant to gas turbines. Recent work in our lab demonstrated that heating the metallic coating of the TBC isothermally in humid environments caused the volatilization of non-ideal oxides as a function of time and water vapor content [4]. This prompted a separate study to investigate the role of increased humidity on the stability of the ceramic coating of the TBC when heated at temperatures relevant to gas turbines. Chapters 4 and 5 of this dissertation will show that an increased humidity will cause an enhanced destabilization of the parent phase in the ceramic coating at temperatures relevant to gas turbines as compared to that of a dry environment. The destabilization behavior will be explained by a proton incorporation mechanism that allows the coherently bound phases to become unconstrained more rapidly by increasing the rate at which the lattice parameters relax to their equilibrium positons.

There has also been action taken to implement alternative fuels into gas turbines used for propulsion. The United States Navy has the goal of reducing its petroleum use by 50% by 2020 [5]. The Navy has proposed to use a blended fuel consisting of a 50-50 blend of its traditional NATO grade F76 fuel and a hydroprocessed renewable diesel fuel (HRD) derived from algae—referred to as the Blend fuel hereafter. The composition of the Blend and F76 fuels are similar but differences in the density and viscosity between the fuels may alter the combustion characteristics of the fuel [5]. This in turn can influence the thermochemical stability of hot section materials used in shipboard turbines. To investigate the influence of the fuel on the

material degradation of the hot section materials, our lab designed and built an experimental test rig to simulate the combustion zone of a shipboard turbine. Chapter 3 will show how changing the combustion environment through the use of an alternative fuel can alter the thermochemical stability of hot section materials used in shipboard gas turbines. The change in the thermochemical stability will be explained in terms of the Blend fuel properties creating a combustion environment that enhances the solubility of the scales on top of the metallic coating.

## 1.2 Thermal Barrier Coating Systems

### 1.2.1 Bond Coat and Oxide

The TBC provides thermochemical stability as well as thermal protection for the underlying metal substrate. The TBC consists of three main components: 1) the metallic coating that sits on top of the superalloy substrate, 2) the in-situ grown external oxide, and 3) the ceramic coating as shown schematically in Fig. 1.2. The metallic coating provides thermochemical stability to the superalloy substrate beneath it. This metallic coating can be used as a stand-alone coating if the propulsion application does not require temperatures in excess of ~1150°C. An example of this application would be marine propulsion where temperatures are lower than ~1000°C and the metallic coating would be referred to as an overlay coating. However, in aero-propulsion or power generation applications—where temperatures can be in excess of 1425°C—an actively cooled ceramic coating is needed and the metallic coating is referred to as a bond coat [6].

Regardless of is coupling with the ceramic coating, the metallic coating provides thermal stability by reacting with the oxygen in the combustion stream in a controlled way. This chemical reaction is termed oxidation and occurs when a metal is converted to a compound, e.g. an oxide, due to the presence of an oxidant (e.g. oxygen). The external oxide that is formed on the metallic coating is the hexagonal structure α-aluminum oxide, or α-alumina, with a thickness

of 10 μm or less [4]. This slow growing, dense oxide on the metallic coating is beneficial in that it prevents the diffusion of oxygen deeper into the metallic coating. However, an external alumina scale can only form on the metallic coating if it contains a large amount or "reservoir" of Al [7]. It wouldn't be possible for the superalloy substrate to maintain the required amount of aluminum to form an external alumina scale, since it would diminish the high-temperature strength needed to withstand the significant centrifugal forces produced by the high rotational speeds of the turbine [8]. Therefore, metallic coatings with an Al reservoir are placed on top of the hot-section superalloys in order to provide thermochemical stability in the form of oxidation resistance to the underlying Ni-based superalloys.

### 1.2.2 Ceramic layer

The outer-layer consists of a ceramic coating that is actively cooled by air that reaches the ceramic through passageways cast into the hot section component. For 30 plus years, the industry-standard material of choice for the ceramic coating was 8 wt% yttria-stabilized zirconia (8YSZ) [9]. 8YSZ has been the material of choice for multiple decades due to its combination of favorable mechanical and thermal properties. The favorable mechanical properties include a high toughness which is critical to prevent "foreign object damage" or FOD that enters the turbine and may impact the ceramic coating [10]. Also, 8YSZ provides good lateral strain compliance allowing it to contract and expand during the engines thermal cycle in a way that will not cause it to delaminate from the underlying metal substrate. These favorable mechanical properties of 8YSZ are in addition to its advantageous low thermal conductivity of the order of 1 W/m-K [6]. The low thermal conductivity when coupled with active cooling can drop the temperature of the underlying metal substrate by as much as 250°C. This ceramic top layer therefore allows gas turbine engines to reach higher temperatures and in turn higher efficiencies.

## 1.3 Metallic Coating Processing Methods and Properties

There are two broad types of alloy coatings that are used as standalones in marine turbines or as part of a hierarchal coating for aero-turbines or power generation: 1) diffusional and 2) overlay. The oldest alloy coatings are the aluminides which are diffusional coatings originally synthesized by pack cementation aluminizing. These coatings were first made by simply embedding the metal to be coated in a powder mixture of aluminum, sal ammoniac ($NH_4Cl$), and graphite and then heat treating the mixture for 2 hours [11]. More recent techniques of aluminizing processes involve chemical vapor deposition processes (CVD) where the internal cooling passages are coated by slurry, forced flow gas phase, or vacuum pulse aluminizing [12, 13].

MCrAlY coatings are a common example of the overlay coatings that are the second type of bond coat besides the diffusional Ni-aluminides. The first overlay composition introduced was a FeCrAlY applied to a Ni-superalloy by electron beam vapor deposition [14]. This coating was limited in practice due to the formation of a NiAl layer between the alloy and coating at high temperatures. The introduction of CoCrAlY coatings showed useful oxidation and corrosion resistance but within a narrow compositional range that was too brittle for airfoils in high-performance engines. Also, a major limitation of this coating in marine turbine applications was its high susceptibility to Type II hot corrosion. NiCrAlY was also not optimal due to limited hot corrosion resistance. Finally, the NiCoCrAlY and CoNiCrAlY were introduced with a nominal composition of Co/Ni-23%, Cr-15%, Al-12.5%, Y-0.5%, and Co/Ni making up the balance. These coatings showed to have a compromise of sufficient hot corrosion and oxidation resistance over a larger composition—NiCoCrAlY having better oxidation resistance and CoNiCrAlY having better corrosion resistance. In order to manufacture such complicated overlay coatings, synthesis methods have expanded from electron beam vapor deposition, to include low-pressure

plasma methods and the plasma shrouded torch [14]. A qualitative summary of the hot corrosion/oxidation resistance of the various alloy coatings is shown in Fig. 1.3.

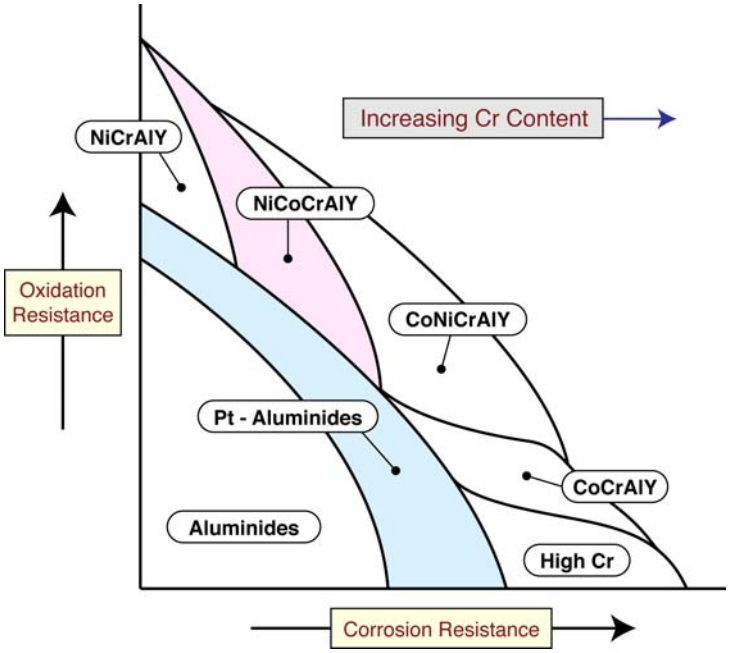


**Figure 1.3 A graphic comparing the oxidation and corrosion resistance of diffusional and overlay alloy coatings within the fields of their compositions.**

### 1.4 Oxidation of the Reservoir Element in the Bond Coat

Alloy coatings will either oxidize internally, have a mixed external scale, and/or form an exclusive, external alumina scale based on the original Al content in the coating as depicted in Fig. 1.4 [15]. Thus a critical part of coating design is the minimum amount of concentration in the alloy necessary to form an external alumina scale or $N_{Al}^{*}$. Inclusion of small concentrations of a third element—that which forms an oxide of intermediate thermodynamic stability between NiO and $Al_2O_3$—was found to decrease $N_{Al}^{*}$ [15]. Such is the case in M-Cr-Al alloys (where M stands for Ni, Co, or Fe) where the inclusion of Cr as a minor constituent reduced the $N_{Al}^{*}$ from 34 at.% in a Ni-Al alloy to just 10 at.% in a M-Cr-Al alloy. The common mechanism for this is known as "secondary gettering" [16]. Here an oxide of the third element is said to form

extensively in the transient scale and thereby reduces the oxygen potential at the scale/alloy interface. The reduced oxygen potential lowers the inward flux of oxygen into the alloy and allows Al to preferentially form an external alumina scale as opposed to being internally precipitated as on oxide.

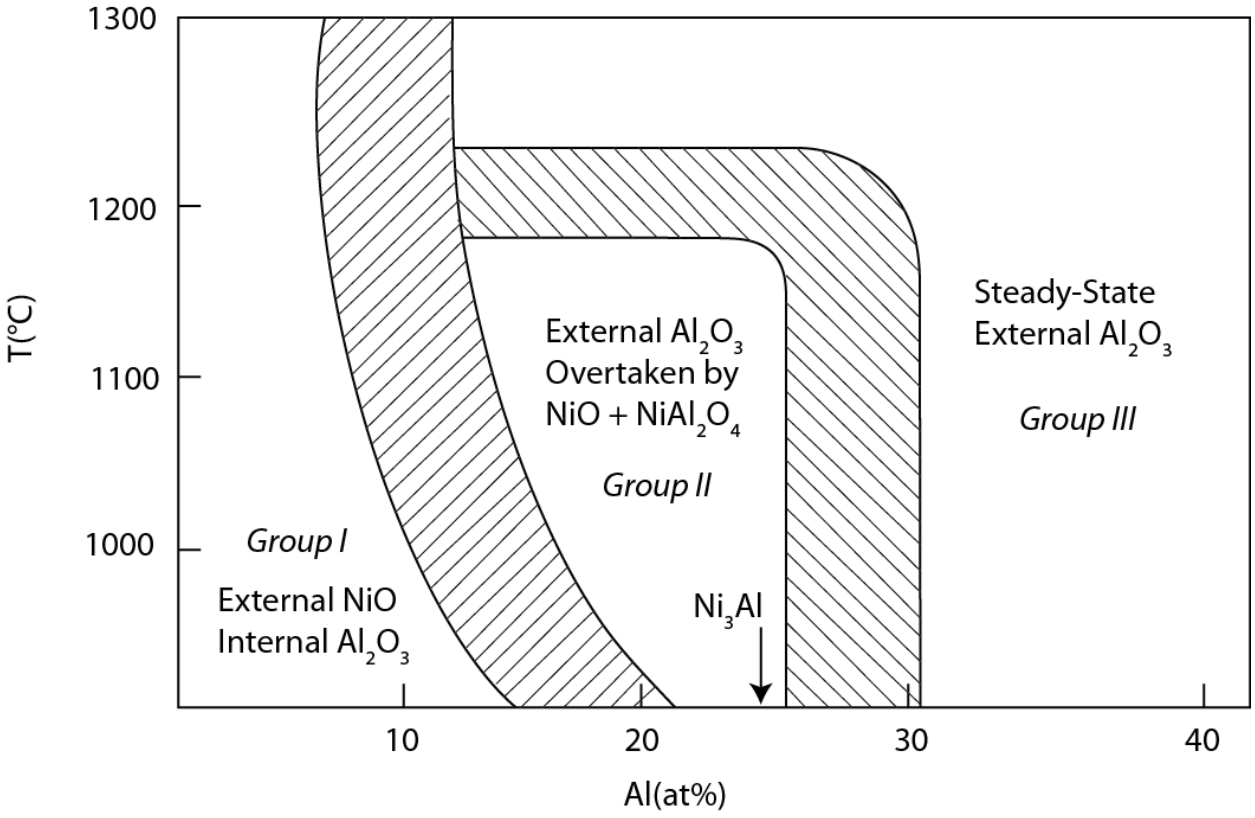


**Figure 1.4 Prediction of the type of oxide that will grow in/on an alumina former based on the operating temperature of the alloy and the original Al content [7].**

Ni-aluminide alloy-coatings are currently modified with Pt to increase the oxidation/corrosion resistance of the Ni-aluminide coatings. Pt modifies the $L1_2$ structure of the Ni-rich γ-Ni and more Ni-lean γ'-$Ni_3Al$ by preferentially substituting for Ni [17]. A Pt-modified Ni-aluminide was found to reduce the $N_{Al}^{*}$ compared to Ni-aluminide alone, as well as promote the formation and adherence of an external alumina scale on the alloy [7]. Besides effectively displacing Ni and enhancing the Al content available for oxidation, the main mechanism for

enhancement of oxidation/corrosion resistance by Pt is due to its ability to alter the Al activity. A Pt-modified alloy exposed to oxidizing conditions will have the Al activity of its depletion zone decrease relative to a Pt-free Ni-aluminide. The Pt-modified alloy would therefore have an increased gradient in Al activity through the coating in comparison to the Pt-free alloy. The end result is an increase in Al diffusion through the alloy and an increase in scaling according to Eq. 1.2 [7].

$$J_{Al}^{i} = -C_{Al}^{i} D_{Al} \frac{\partial \ln a_{Al}}{\partial x} \qquad \text{[Eq. 1.2]}$$

Here $C_{Al}^{i}$ is the interfacial Al content at the scale/alloy interface, $D_{Al}$ is the diffusion coefficient of Al, and $J_{Al}^{i}$ is the outward diffusive flux.

### 1.5 Reactive Elements in Alloy Coatings

While the benefit of the third element in M-Cr-Al alloys has been discussed, further discussion is needed to describe the benefits of Y or other minute constituents like it. It is known that adding reactive elements (REs) such as Y, Hf, and Zr to bond coats is an effective way to improve oxidation resistance by slowing down the growth of the scale and improving its adhesion to the coating [18]. However, the mechanism behind the improved oxidation resistance is widely disputed in the literature. The REs are thought to oxidize and form "oxide pegs" or intrusions [10], but the effect on the mechanical properties of the coating is in debate. While it would seem that the "oxide pegs" would improve the coatings properties such as toughness [18, 19], it has been suggested by some that the "oxide pegs" make the coatings more brittle [20]. Another benefit of REs, is acting as a "secondary getter" of S impurities in the alloy-coating [10, 18]. Sulfur impurities within the coating have been found to coalesce at the coating/scale interface and thus weakens the interfacial bond strength. Therefore, the ability of REs to prevent the sulfur segregation beneath the scale has increased the lifetime of the coating. More recently,

increased adhesion due to the REs has been attributed to the open, d-shell electronic structure of the transition metals like Ti, Zr, and Hf, which enhances the bonding between the alumina and metal substrate [21-23]. This electronic character was thought to provide strong bonding due to a mixture of ionic, covalent, and donor-acceptor bonding between the RE dopant and the oxygen in alumina.

### 1.6 Ceramic Layer Processing and Properties

The 8YSZ can be applied to the bond coat in one of two deposition methods depending on the application: 1) electron beam physical vapor deposition (EBPVD) or 2) air plasma sprayed (APS). The physical vapor deposition of EBPVD refers to the deposition of a material in a vacuum without chemically reacting it to the substrate [2]. The electron beam in EBPVD refers to the use of a focused electron beam to vaporize a desired chemistry from an initial button of YSZ chemistry or ingot. Due to the differences in vapor pressure between yttrium and zirconium, the composition of the initial ingot will be different than the composition deposited on the substrate. Therefore, the initial chemistry of the ingot needs to be tailored to account for the different volatilization rates of yttrium and zirconium. The hot-section substrate to be coated is preheated and manipulated in a cloud of volatile material so that the preferred chemistry will condense onto the substrate. The need to use the EBPVD method in a high vacuum makes this method of deposition more expensive than APS and limits its use to more high performance applications such as in the blades and vanes of aero-turbine applications.

The 8YSZ coatings deposited by EBPVD are typically 125 um thick and have characteristic microstructural features [24]. At the bottom of the coating, near the ceramic/metal interface there is a region of equiaxed grains of the order of 0.5 μm. Growing out of the equiaxed grains are featherlike columns with diameters of the order of 10 μm that contain nanometer-scale porosity as shown in Fig. 1.5 [25]. There are channels between the columns that provide the

coating with lateral strain tolerance to accommodate the thermal expansion mismatch with the underling metallic coating [9].

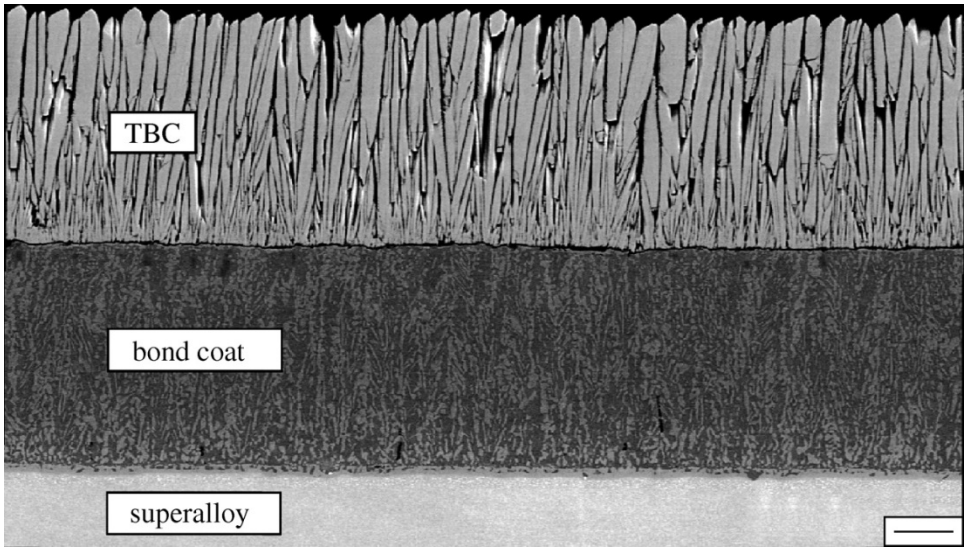


**Figure 1.5 A SEM image of an EBPVD YSZ coating deposited on to a bond coat with a scale bar of 50 µm [25].**

APS involves the injection of the coating material in the form of a powder or a pellet into a high-temperature plasma stream that has been created inside a plasma gun. While in the plasma gas stream, the injection material is melted and accelerated toward a substrate which will be preheated prior to application. The injection material ideally forms "splats" along the substrate so that it spreads out in a direction parallel to the substrate. A resulting coating is built up with successive splats stacked on top of one another to form the microstructure shown in Fig. 1.6. The heated substrate allows for the formation of a column structure through the splats in the direction perpendicular to the substrate. This process is advantageous from the standpoint that there is no concern of different vapor pressures for elements to be deposited [26]. There is therefore more flexibility in the composition of materials that can be deposited as compared with EBPVD. However, due to variations in the melting temperature of the starting powder, it is expected that a

certain number of particles will reach the substrate prior to melting and will appear embedded between splat layers.

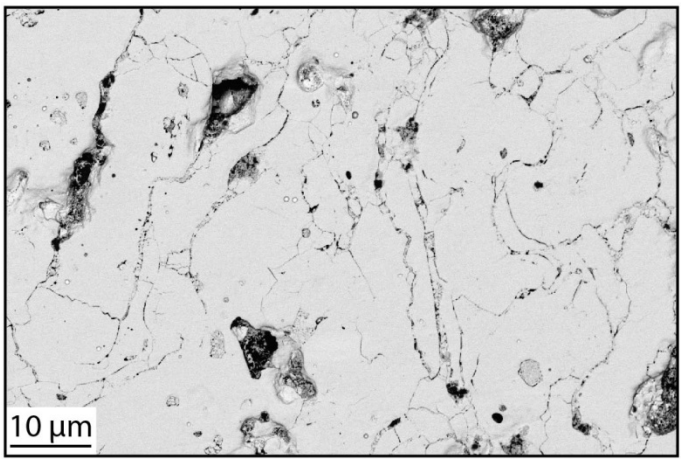


**Figure 1.6 A BSE SEM image of a cross-section of an as-received APS YSZ coating.**

The splat morphology of the APS coatings provides a distinct microstructure from the EBPVD coating and therefore different properties. The overall coating thickness is larger than that for an EBPVD coating being at least 300 µm thick. The individual splat sizes can vary significantly with a thickness between 1 to 5 µm in thickness and a diameter between 200 to 400 µm. The 15 to 25 vol% porosity in the APS coatings allow for a more compliant coating that provides some strain tolerance to accommodate the thermal expansion mismatch in a different way than the of the EBPVD microstructure. Both the porosity and the splat boundaries allow for a lower thermal conductivity than that which can be achieved in an EBPVD microstructure. However, to ensure adequate adhesion of the APS coating to the bond coat a rough bond coat surface is required. This produces out-of-plane stresses—tension at the crests and compression at the troughs—causing fracture along the oxide/ceramic coating interface and cracking in the ceramic coating near the crests [27]. This along with other mechanical failure modes limits the

APS coatings to industrial gas-turbine engines where there are fewer thermal cycles and reduced temperature gradients across the coating due to lower service temperatures.

## 1.7 Routes of Failure

### 1.7.1 Hot Corrosion

Accelerated oxidation of metals and alloys occurs in the presence of alkaline metal salts and sulfur at temperatures in the range of 650-950°C [28]. This accelerated form of degradation has been historically termed hot corrosion and is common in shipboard turbines. Sodium from the marine environment and sulfur from the fuel and/or marine environment react to form a molten sodium sulfate above 884 °C. These molten sulfates dissolve the protective oxide that is formed on alloy coatings at engine operating conditions. The current understanding of the hot corrosion mechanism is described by a fluxing mechanism where the formation of a basicity gradient at the alloy-molten salt interface causes self-sustaining hot corrosion [29, 30].

Hot corrosion can be characterized further into two regimes—Type I—high-temperature hot corrosion—and Type II—low temperature hot corrosion. Type I hot corrosion is most prevalent at temperatures ranging from 850-950 °C [28]. Characteristic of this type of hot corrosion is a uniform attack on the alloy with internal sulfides located immediately below the oxide scale as shown in Fig. 1.7. Selective diffusion of a reservoir element from the coating leaves a depletion zone of the reservoir element immediately below the oxide. The dissolution of the protective oxide scale by the metal sulfides is believed to occur due to a basic reaction where the metal oxide dissolves in the sulfate melt as a complex anion as shown in Eq. 1.3 [29].

$$MO + O^{2-} = MO_2^{2-} \qquad \text{[Eq. 1.3]}$$

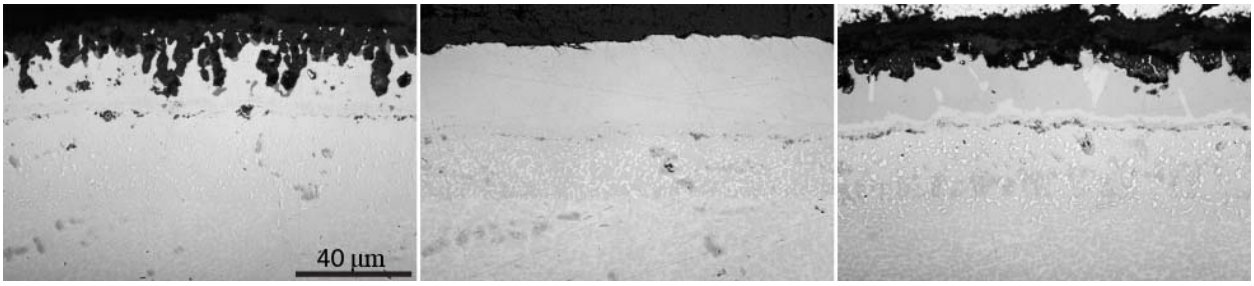


**Figure 1.7 The Type I hot corrosion morphology of a NiAlPt coating after exposure in the LVBR as compared to its as-received condition (center).**

Type II hot corrosion is the predominate degradation mechanism of turbine hot section materials in the temperature range of 600 – 750 °C [31]. The morphology of this type of attack is characterized by large, sulfide-containing pits that appear non-uniformly on the exposed alloy as shown in Fig. 1.8 [28, 31, 32]. The pitting is the result of a gaseous reaction of $SO_3$ and/or $SO_2$ with CoO and NiO that causes these oxides to become unstable and dissolve. Low melting eutectic mixtures consisting of $Na_2SO_4$–$CoSO_4$ or $Na_2SO_4$—$NiSO_4$ form as a result of the gaseous reaction between sodium sulfate and the Ni /Co superalloys containing Al and/or Cr. The morphology of the Type II attack does not contain the Type I characteristics of sulfides or a depletion zone beneath the scale. This is likely the result of the difficulty in forming a $Cr_2O_3$ or alumina external scale at Type II temperatures. Furthermore, the level of attack on the superalloy in Type II conditions has been shown to be a function of the partial pressure of $SO_3$ or $p_{SO_3}$ [32]. As a result of a higher relative $p_{SO_3}$, Type II has an acidic type of fluxing defined by the reaction shown in Eq. 1.4.

$$MO = M^{2+} + O^{2-} \qquad \text{[Eq. 1.4]}$$

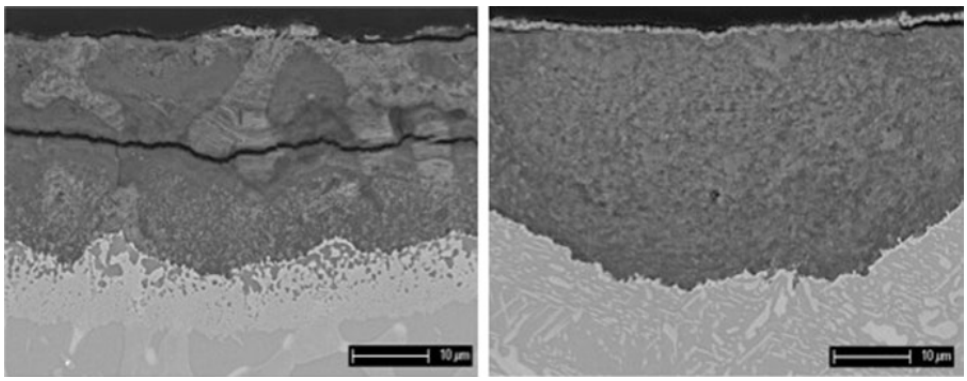

**Figure 1.8 Scanning electron micrographs showing the Type II hot corrosion attack on a NiCoCrAlY (left) and a CoCrAlY (right) [33].**

Of particular interest for marine turbines is the idealized case of molten sodium sulfate on Ni [33]. The melt will cause the formation of an external NiO scale by the removal of oxygen from the sodium sulfate melt. The removal of oxygen in the melt lowers the oxygen activity locally at the melt/metal interface allowing the increase of sulfur activity and subsequent formation of nickel sulfides to form. The nickel sulfides will dissolve or flux the oxide layer so that the sodium sulfate will come into direct contact with the Ni causing the sulfidation reaction shown in Eq. 1.5. The sulfidation reaction produces a large concentration of oxide ions within the melt. The dissolution of these oxides produces a negative basicity gradient within the fused salt film from the melt-oxide interface (high basicity) to the melt-gas interface (low basicity) as shown in Fig. 1.9. This negative basicity gradient provides the required flux of solute metal into the fused salt film to allow for a self-sustaining hot corrosion reaction.

$$4Ni + Na_2SO_4 = 3NiO + NiS + Na_2O \qquad \text{[Eq. 1.5]}$$

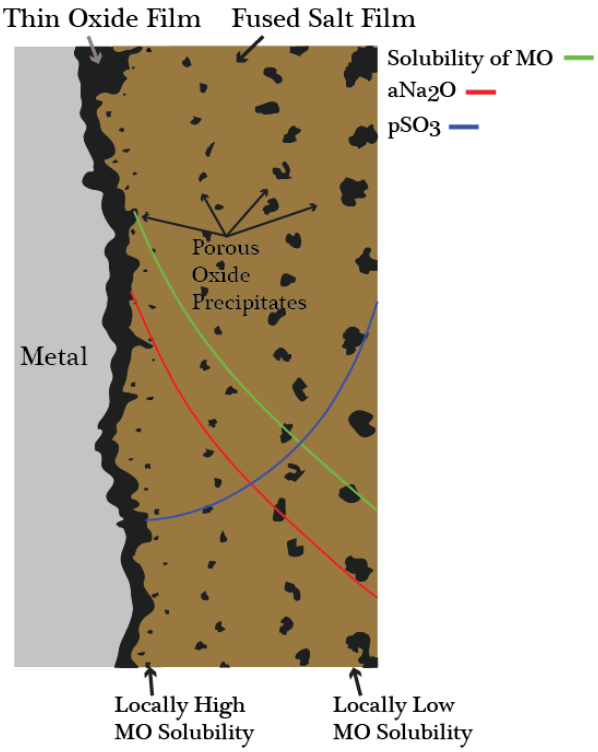


**Figure 1.9 Redrawn graphic of the proposed fluxing mechanism of hot corrosion for molten sodium sulfate on Ni [8].**

While the proposed fluxing mechanism provides a means to explain the necessary gradient for the hot corrosion reaction, it still has limitations that make its description of the mechanism incomplete [8]. The fluxing mechanism model assumes a steady state condition which is difficult to achieve in practice. The formation and growth of metal sulfides is not included in the model even though continued sulfide growth will remove sulfur from the melt and destabilize it unless there is a continuous supply of $p_{SO_3}$. Furthermore, unless conditions at the interface remain constant—like the $p_{SO_3}$—the chemistry of the melt will not be constant. Changes in the melt chemistry will not keep the hot corrosion reaction self-sustaining, as there will not be a consistent supply of fluxing ions to create the necessary activity gradient. Lastly, sustaining a continuous liquid diffusion path from the melt to the exposed metal is another unlikely condition. As the sulfidation reaction continues, the accumulation of the oxide precipitates will continue to constrict the diffusion path through the melt. Therefore, the steady-state assumptions implied in the fluxing mechanism make it unrealistic in a gas turbine engine

environment with rapid thermal cycling. Further research is needed to more accurately model the transient nature of hot corrosion in gas turbine engines.

### 1.7.2 8YSZ Aging

While both APS and EBPVD 8YSZ coatings fail primary due to mechanical means, the thermochemical conversion of these coatings can reduce the toughness of these coatings making them less resistant to FOD. With evidence that the inlet temperatures of gas turbine engines has risen to 1425 °C or higher [3], recent research has investigated the stability of the *t'* that is locked into the 8YSZ coating. The *t'* phase designates a metastable tetragonal phase that has favorable toughness properties due to phase transformation to the monoclinic phase [34] as well as ferroelastic domain switching [35]. The *t'* phase does not transform to the monoclinic phase upon cooling down to ambient temperature even though the phase diagram predicts that it should. This is believed to be due to coherently strained interfaces between neighboring, nanoscale tetragonal and cubic grains [36]. However, exposing either the APS or EBPVD 8YSZ coatings at high temperatures for prolonged time periods—or "aging" these coatings—has shown that the *t'* phase decomposes to its equilibrium phases—the tetragonal and cubic phases. The tetragonal phase is then susceptible to converting to the monoclinic phase upon cooling to ambient temperature which is undesirable as the monoclinic phase has no associated toughening mechanism. However, all of these studies have been done in "laboratory air" environments and little is known about how the aging process is influenced by alternative environments. In chapters 4 and 5, it well be demonstrated how an increased and controlled humidity accelerates the aging process of APS coatings due to an enhanced ability to overcome the coherency strains locking in the *t'* phase.

# 2 Chapter 2: Experimental Techniques

## 2.1 Thermal Aging Experiments

Dry and humid thermal aging was performed in an environmentally controlled tube-furnace. The environmental control refers to specifying and controlling the partial pressures of the gases used in the tube—namely oxygen, nitrogen, and water vapor. This is in contrast to a lot of experiments described in literature where the samples were heated in a furnace with "laboratory air." This can be problematic as ambient humidity can fluctuate with location, season, and temperature. So even if the same experimental set-up is used for each thermally exposed sample, the humidity can be an unknown variable in the experiment if "laboratory air" is used for the environment.

In order to greatly reduce the uncertainty of humidity in the thermal aging experiments, all experiments were performed in a controlled environment set-up. For the dry thermal aging, the controlled environment consisted of a gas mixture comprised of 80 % $N_2$ and 20% $O_2$ by volume. Both the nitrogen and oxygen were derived from separate cylinders consisting of 99.99 vol% of their respective gas. This composition was chosen to simulate air devoid of humidity with only a parts-per-million contribution of water content coming from the gas cylinders. This dry-air composition was controlled by a multi-channel mass flow controller (*MKS Instruments*, model 647B) that is capable of setting and holding the flow rates for each mass flow controller. The flow set-points of the multi-channel controller were calibrated using a *Bubble-O-Meter*. Here, a soap-solution allowed for measuring the time of a bubble to pass through a fixed volume in order to calculate the true flow rate of a set-point.

To ensure that the desired controlled environment was achieved before reaching the aging temperature, care was taken to purge the furnace of "laboratory air" while at ambient

temperature. The amount of time used for the purge was determined by the calculation of a residence time, $\tau$, as defined by Eq. 2.1.

$$\tau = \frac{V}{f} \qquad \text{[Eq. 2.1]}$$

In Eq. 2.1, $V$ is the volume of the sealed environment and $f$ is the volumetric flow rate. The "laboratory air" was considered to be purged when the desired gas composition was flown through the experimental set-up for an equivalent of six residence times. For a four foot long ceramic tube with a 2 in inner dimeter, the dry purge time would be approximately 133 min at a flow rate of 80 sccm.

Performing a thermal aging test with controlled humidity requires additional measures to be taken to obtain a specific partial pressure of water, or $p_{H_2O}$, all the way through the system while not allowing the water to condense anywhere near the ceramic tube and causing it to thermal shock. Therefore, an experimental set-up as shown in the graphic of Fig. 2.1 was employed. Instead of having the gas go directly into the inlet of the furnace, it is directed through a de-ionized water tank that is thermally controlled by heating tapes covered with insulation. The de-ionized water tank is heated and set to a temperature in order to provide a desired $p_{H_2O}$ or humidity level in the gas composition as dictated by saturated steam tables. For example, keeping the temperature of the de-ionized water tank to 79°C by the use of would allow for a 45% by volume water vapor content in the gas. To ensure that this amount of water vapor was flowing through the system for a given experiment, an Erlenmeyer flask was connected at the exhaust of the ceramic tube to allow measurement of the condensed water vapor. Comparison of the measured values of the condensed water to those calculated theoretically by steam tables showed an error value of less than 3%.

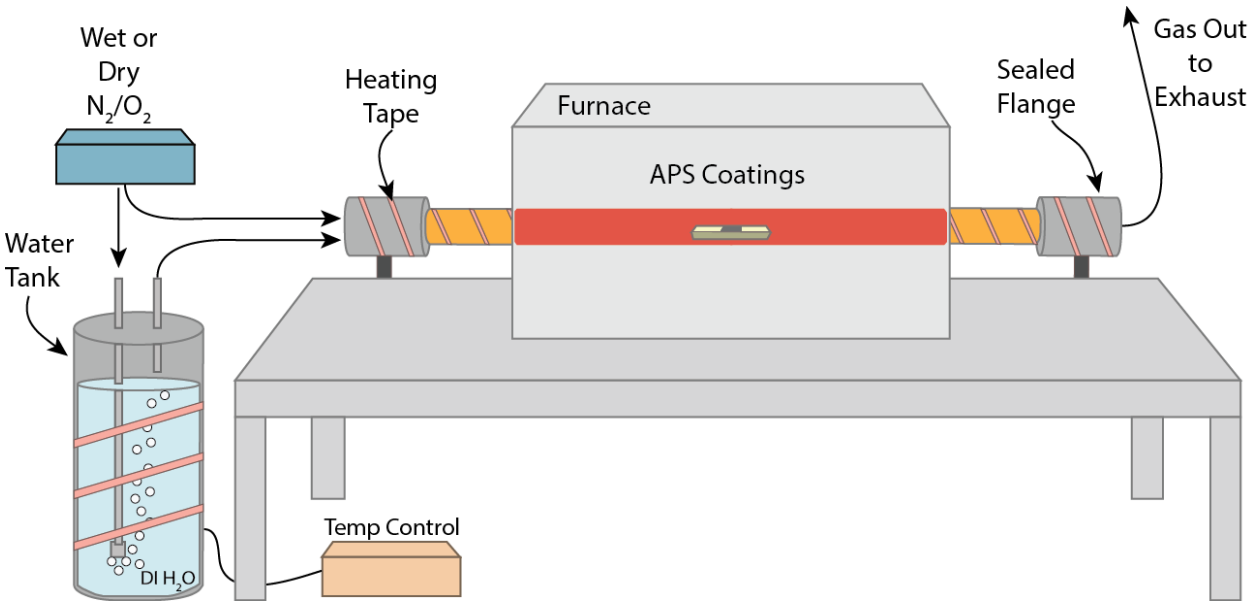


**Figure 2.1 Graphical representation of the experimental set-up used to perform the thermal aging tests in a controlled environment.**

Once the humidified gas composition leaves the water tank, it needs to be heated throughout the experimental set-up to ensure that it reaches the samples in a vapor form and not condense on any of the metallic fittings in contact with the ceramic tube. As shown in Fig. 2.1, the heating of the experimental set-up outside of the hot zone of the furnace is accomplished by heating tapes covered with insulation. The heating tapes were controlled by proportional controllers that were set to achieve a temperature of approximately 125 °C. The heating tapes covered both the inlet and outlet metal flanges as well as four inches of the mating ceramic tube on each end. To ensure that the humid environment was achieved by the time the aging temperature was reached a purge of six residence times within the desired humid environment was performed after the dry purge. During this humid purge, the gas composition was flowed through the water tank with all heating tapes on and the furnace set to 150 °C by manual control. At the conclusion of the aging test, the gas bypassed the water tank by the use of a gate valve once the furnace temperature got below 150 °C. This allowed the remaining water vapor to

volatilize away during the rest of the furnace cooling period and not condense on the sample prior to it being removed from the ceramic tube.

## 2.2 Raman Spectroscopy Analysis

Raman spectroscopy was employed as a means to supplement the XRD analysis of the thermally aged samples with a much smaller probing volume (~ 1 $\mu m^3$). In Raman spectroscopy, a sample is irradiated with a laser beam with a frequency $\nu_0$ and scattered light is observed in the direction perpendicular to the incident beam [37]. Two types of scattered light are present in the spectrum as shown in Fig. 2.2: 1) Raleigh scattering and 2) Raman scattering. The Raleigh scattering is considered strong and has the same frequency $\nu_0$ of the incident beam. However, Raman scattering is weak with an intensity of $\sim 1 \cdot 10^{-5}$ of the incident beam and has a frequency shift, $\nu_m$, from the incident beam that is the frequency of the molecule or atomic bond. The Raman lines that correspond to a shift of the $\nu_0 - \nu_m$ nature are known as the Stokes lines while a shift of the $\nu_0 + \nu_m$ nature is known as the anti-Stokes lines as shown in Fig. 2.2. Both the Stokes and Anti-Stokes lines provide the same information but the Stokes lines are typically stronger and therefore it is customary to measure the Stokes side of the spectrum. Thus, the "Raman shift" is the shift of the frequency from that of the incident beam caused by the frequency of the molecule or atomic bond.

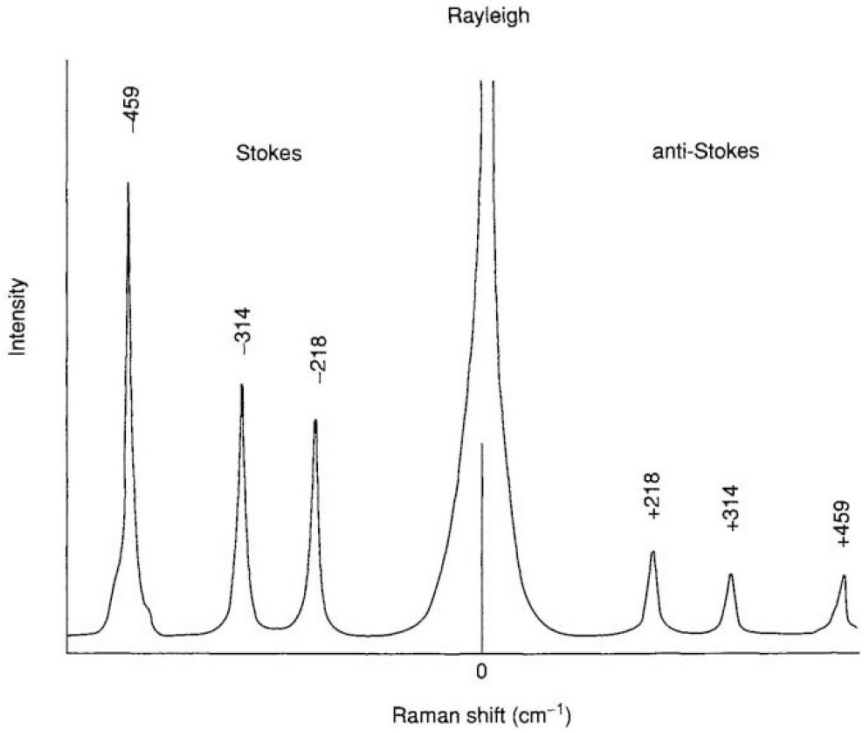


**Figure 2.2 Raman Spectrum of $CCl_4$ showing the two different types of scattered light present after laser excitation: 1) Raleigh scattering and 2) Raman scattering (Stokes and Anti-Stokes lines) [37].**

All Raman spectroscopy results obtained for this dissertation were performed at the Laser Spectroscopy Facility on UCI's campus. There are currently three lasers that are available to use on the Raman microscope. The red laser of 785 nm provides high resolution in terms of the amount of Raman shift but has a low signal-to-noise ratio, while the blue laser of 405 nm has a high efficiency of Raman scattering but lower Raman shift resolution. The green laser of 532 nm has Raman scattering efficiencies and resolution between the other two lasers and was thus chosen as optimal for probing the thermally aged samples. There are several other parameters that need to specified in order to obtain spectra with the given laser. Some of the important parameters are laser power, exposure time, and accumulations. The laser power was normally chosen to be 100% to optimize the signal-to-noise ratio while reducing the time spent to acquire

spectra. There is no real drawback to using full laser power as the interaction volume does not increase with higher power. It should also be noted that the surface of the samples probed was not polished and was also porous which are two factors that will limit the amount of signal that can be obtained. The other two laser parameters—exposure time and accumulations—were optimized in a similar way with preference given to increasing the number of accumulations over that of the exposure time. This was because each additional accumulation will be added to the previous one to give a larger cumulative signal, while increasing the exposure time will have a similar effect but can give rise to signal sources that are not sample dependent. Exposure times were typically less than five seconds and the amount of accumulations was three or less.

In order to determine the peak centers of the Raman modes and obtain quantitative results, it is necessary to calibrate the Raman system and due peak fitting. The calibration of the Raman system was performed by obtaining a Raman spectrum from a Si standard. The Si peak should be at 520.5 $cm^{-1}$ ± 0.5 $cm^{-1}$ with deviations in the value due to thermal fluctuations or instrument optics. The value obtained from the Raman spectrum of Si would then be used to offset the values of the subsequent spectrum taken of the thermally aged samples during the same session. For example, if the Si value obtained was 520.2 $cm^{-1}$, than an offset of +0.3 $cm^{-1}$ would be applied to all the values of each spectrum taken from the samples during the remainder of the session. This calibration was found to be extremely important to do during each session, as the same samples were found to have differences of ~1 $cm^{-1}$ in Raman shift values when the spectrum was taken on different days. However, the relative difference in Raman shift values between samples was always found to be the same as long as the spectrum was obtained during the same session. Therefore, any time peak fitting was performed on Raman spectra, all spectra that were going to be compared needed to be taken during the same session.

Raman peak fitting was performed in either the plotting software *Origin* or *Matlab*. In either case the raw Raman data was fit using an Asymmetric Double Sigmoidal peak function as shown in Eq. 2.2.

$$y = y_0 + A \cdot \frac{1}{1 + e^{-\frac{x - x_c + \frac{w_1}{2}}{w_2}}} \cdot \left( 1 - \frac{1}{1 + e^{-\frac{x - x_c - \frac{w_1}{2}}{w_3}}} \right) \qquad \text{Eq. 2.2}$$

In Eq. 2.2, $y_0$, $A$, $x_c$, $w_1$, $w_2$, and $w_3$ are all fitting parameters. The Asymmetric Double Sigmoidal peak function was used in order to accurately capture the asymmetric Raman lines of tetragonal zirconia [38]. Each Raman peak was fit using the data from above the full width at half maximum point in order to ensure consistency in peak fitting. Once the constant values were obtained from the fit, Raman shift values were inputted into Eq. 2.2 in order to obtain the corresponding intensity. The data set generated from the fit was then differentiated and the Raman shift value that gave a corresponding intensity value of zero was determined to be the center of the peak. For a given sample, this fitting routine would be performed for ten of the same Raman peaks from spectra taken more than 10 μm apart from one another. Two or three of these Raman peak values would usually be significantly different from the rest due to surface roughness or pore scattering and would not be included in the averaging of the Raman peak center values reported in this dissertation.

### 2.3 Quantitative X-ray Diffraction Analysis by Rietveld Refinement

Quantitative XRD was performed by the use of the General Structure Analysis System (GSAS) software with the EXPGUI graphical interface. This analysis was used to determine the phase fractions of the thermally aged samples at different aging times and the results are presented in chapter 4. In this section, the physical basis and influence of five parameters

commonly refined in GSAS will be explained via a short parametric study. These parameters are related to the profile (*GU*, *LX*, and *Asym*), the atomic displacement (*Uiso*), and the texture. Each parameter starts from a value of 0 and is increased by 10%, 20%, 50%, and 100%. The *GU* parameter is based on a term in the Gaussian variance of the peak which is defined by Eq. 2.3.

$$\sigma^2 = U\tan^2\theta + V\tan\theta + W + P/\cos^2\theta \qquad \text{Eq. 2.3}$$

The *U* coefficient is the same as the *GU* parameter in GSAS and is related to the microstrain within crystallites. The influence of the *GU* parameter on the XRD spectra of the *t'* phase is shown in Fig. 2.3.

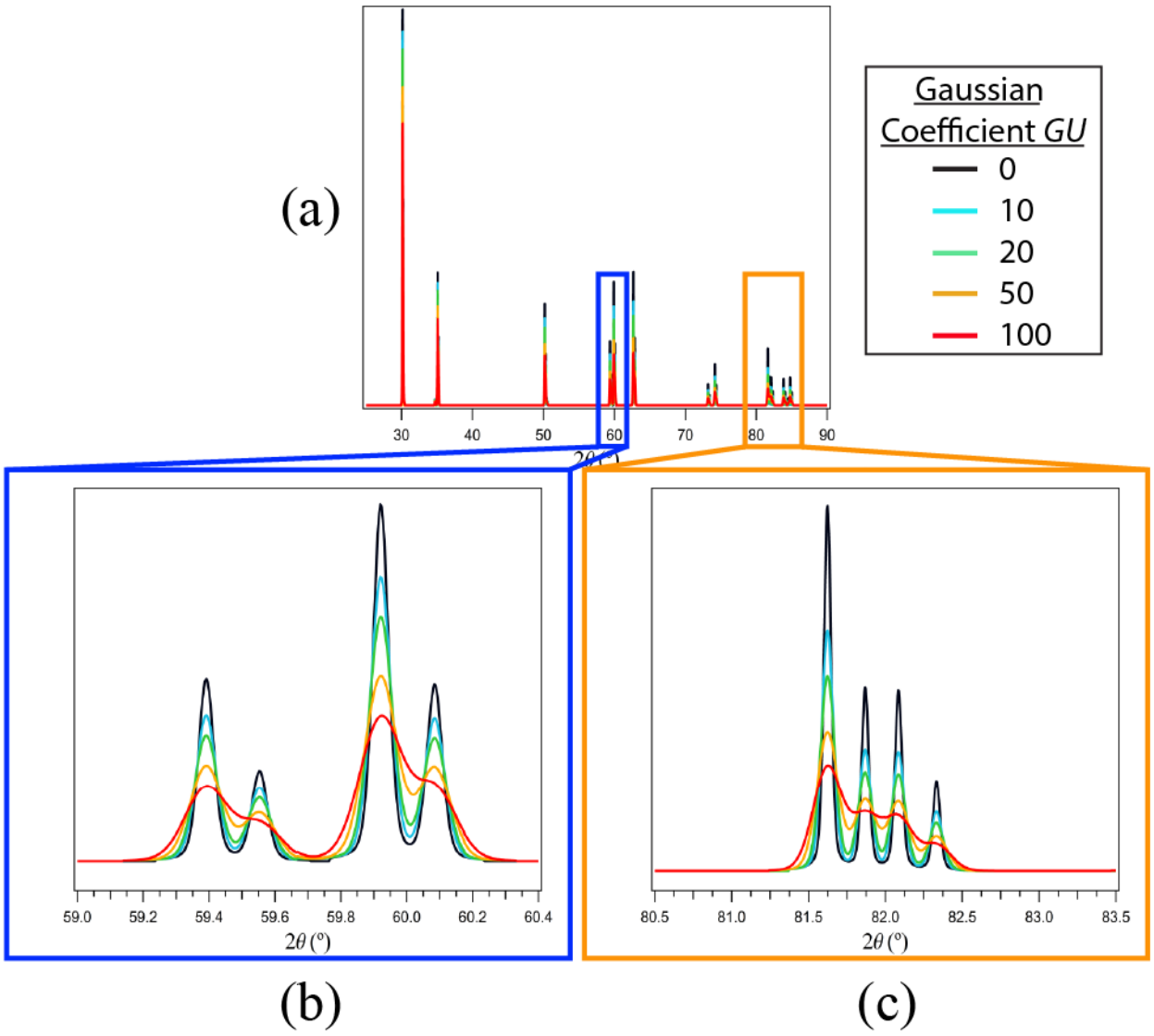

**Figure 2.3 The influence of the Gaussian coefficient *GU* on the XRD spectra of the *t'* phase.**

The *LX* parameter is based on one of the coefficients in the Lorentzian function which is described by Eq. 2.4.

$$\gamma = \frac{X}{\cos\theta} + Y\tan\theta \qquad \text{Eq. 2.4}$$

The *X* coefficient is the *LX* parameter in GSAS and is related to the crystallite dimensions in the sample. The influence of the *LX* parameter on the XRD spectra of the *t'* phase is shown in Fig. 2.4.

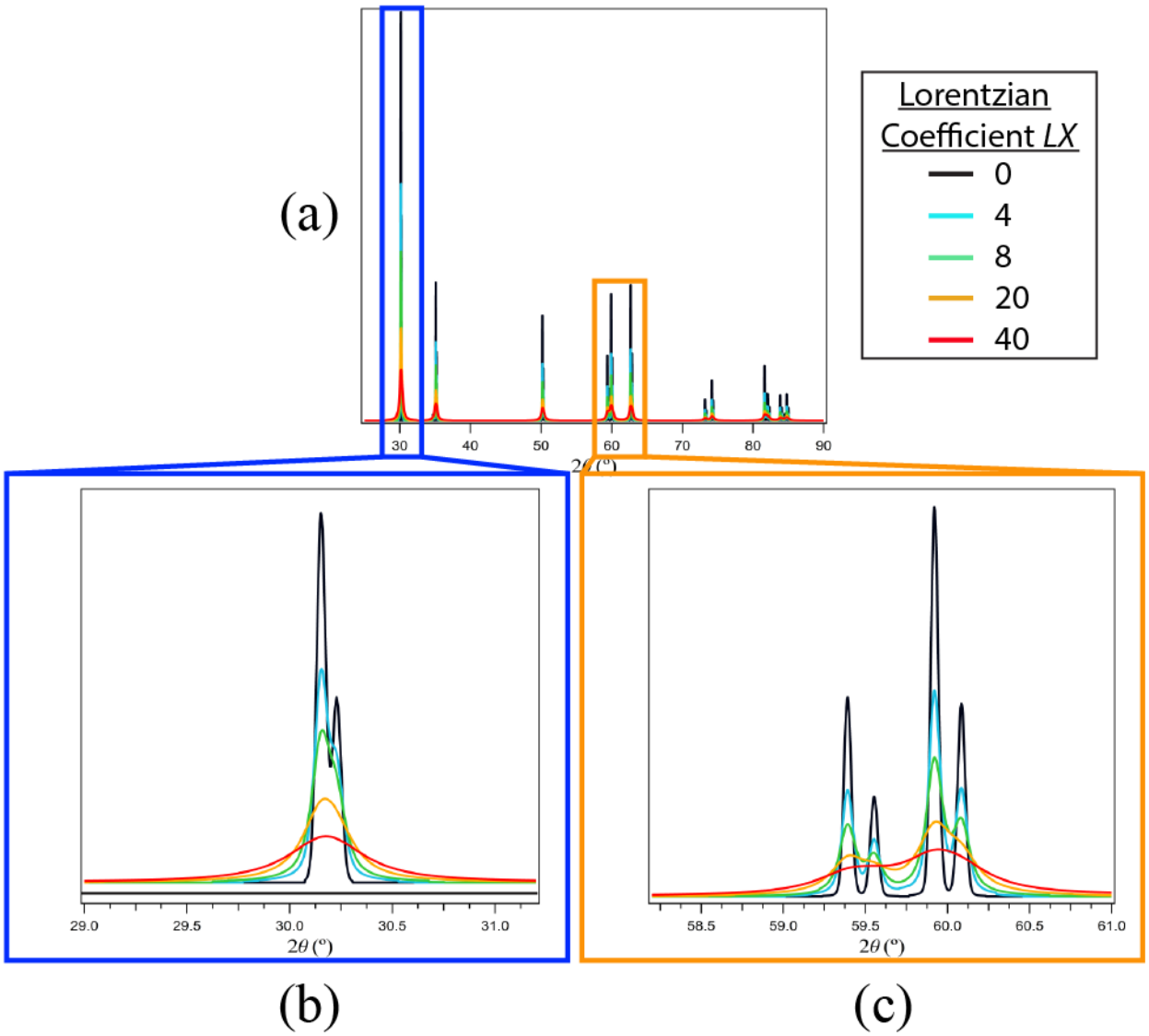


**Figure 2.4 The influence of the Lorentzian coefficient *LX* on the XRD spectra of the *t'* phase.**

The *Asym* parameter is found in the pseudo-Voigt function used to fit the experimental data as in Eq. 2.5.

$$\Delta T' = \Delta T + \frac{f_i A_s}{\tan 2\theta} + S_s \cos\theta + T_s \sin 2\theta \qquad \text{Eq. 2.5}$$

The $A_s$ coefficient is the *Asym* parameter in GSAS and it is related to the 2θ difference modified for asymmetry. The influence of the *Asym* parameter on the XRD spectra of the *t'* phase is shown in Fig. 2.5.

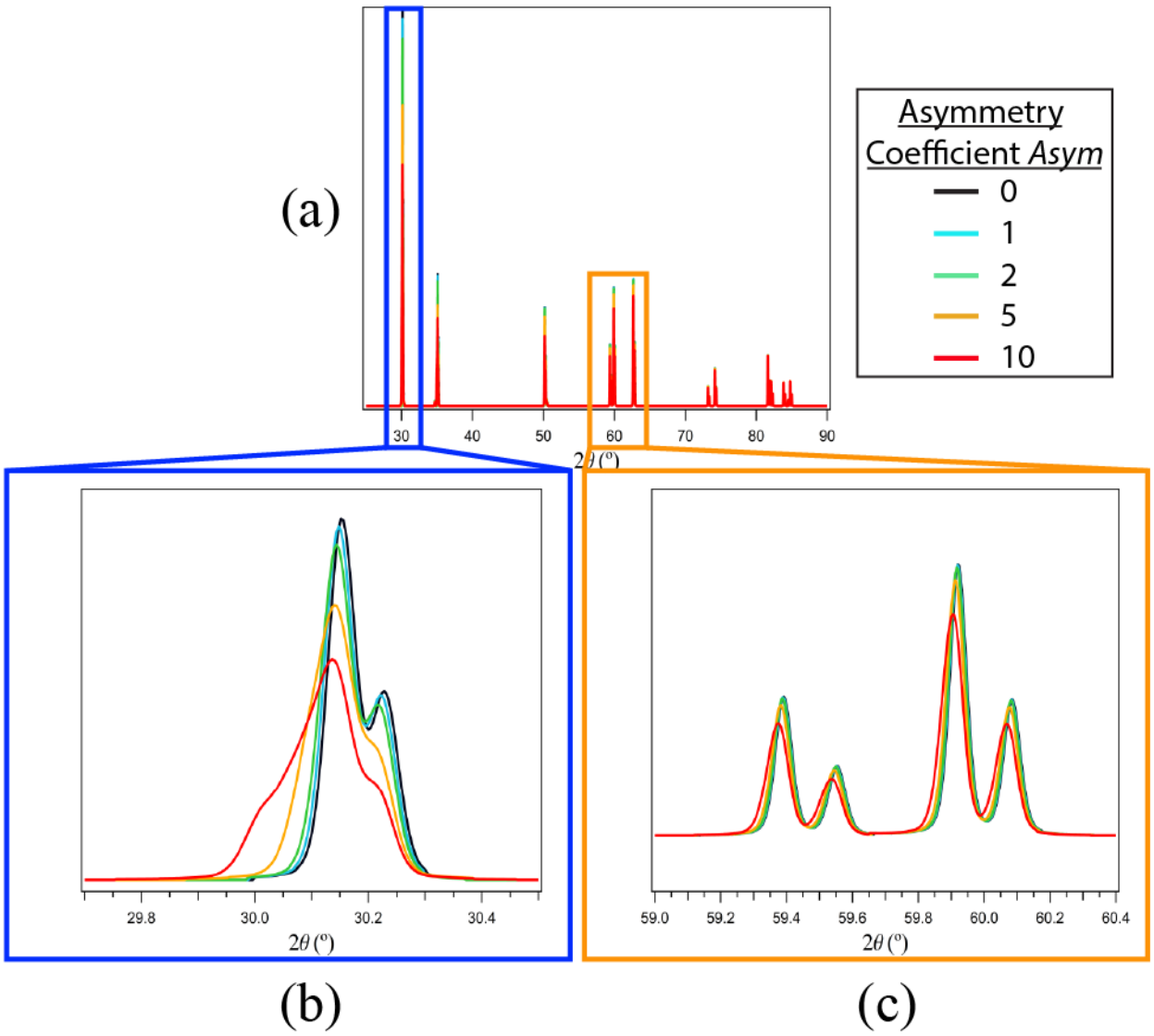


**Figure 2.5 The influence of the asymmetry parameter *Asym* on the XRD spectra of the *t'* phase.**

The atomic displacement parameter or thermal parameter is known as $U_{iso}$ in GSAS if the displacement is isotropic or $U_{ij}$ if it is anisotropic. The thermal motion tensor for an atom is defined by Eq. 2.6.

$$U_i = T + A_i S + S^T A_i^T + A_i L A_i^T \qquad \text{Eq. 2.6}$$

$T$, $S$, and $L$ are the translation, screw, and libration (not a typo) thermal motion matrices and $A_i$ is a Cartesian coordinate matrix. The influence of the oxygen $U_{iso}$ parameter on the XRD spectra of the *t'* phase is shown in Fig. 2.6.

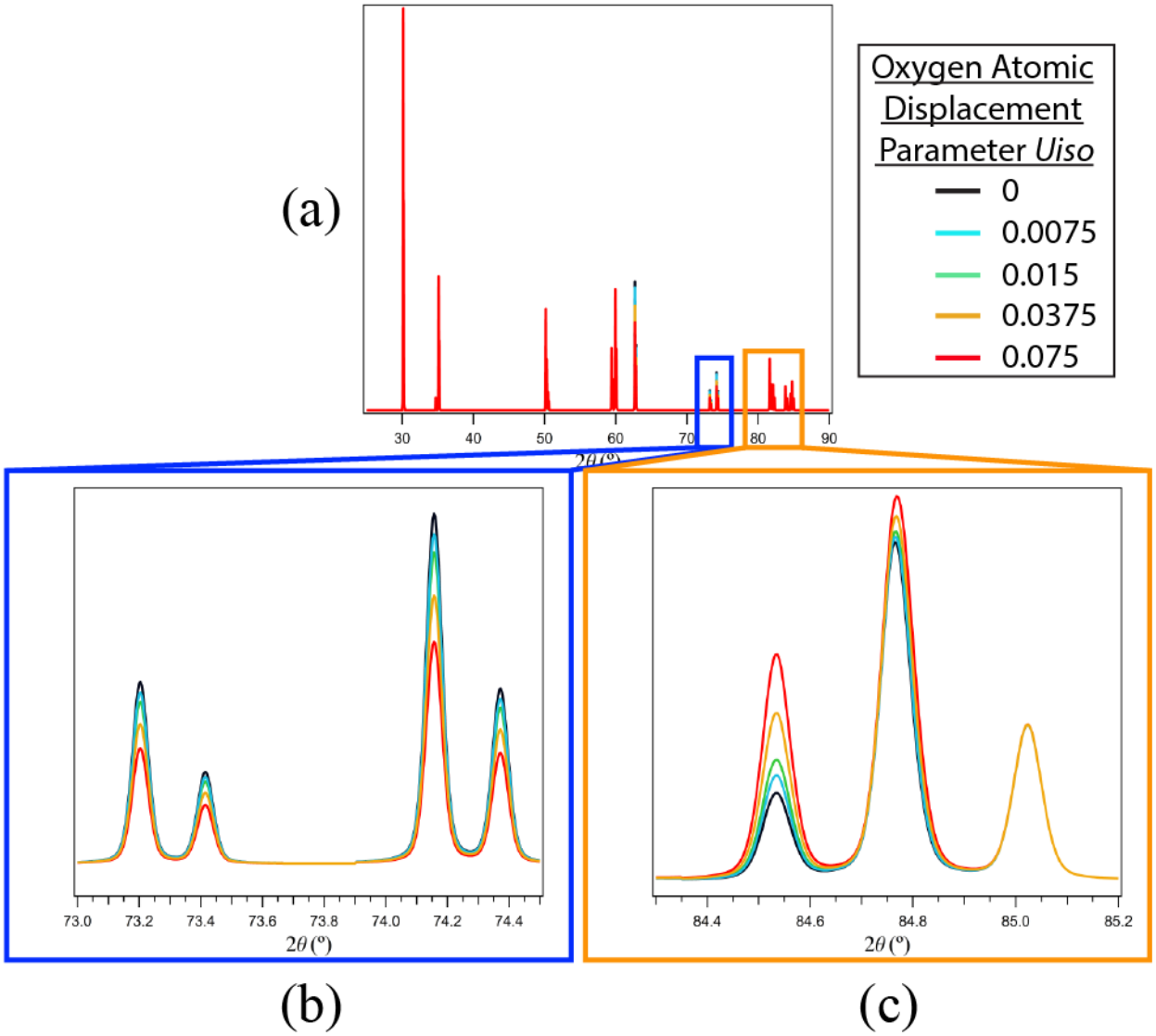


**Figure 2.6 The influence of the oxygen *Uiso* parameter on the XRD spectra of the *t'* phase.**

A way to correct for preferred orientation in GSAS is to use a formulation described by Bunge [39] known as the spherical harmonics function. The spherical preferred orientation correction is described by Eq. 2.7.

$$O_p(h,y) = 1 + \sum_{L=2}^{N_L} \frac{4\pi}{2L+1} \sum_{m=-L}^{L} \sum_{n=-L}^{L} C_L^{mn} k_L^m(h) k_L^n(y) \qquad \text{Eq. 2.7}$$

This formulation is a function of the reflection, *h,* and on the sample orientation, *y*. The two harmonic terms $k_L^m(h)$ and $k_L^n(y)$ take on non-zero values according to the crystal and sample symmetries, respectively. By increasing the "spherical harmonic order," the user is increasing the number of harmonic terms used in the summation. The influence of spherical harmonic order texture on the XRD spectra of the *t'* phase is shown in Fig. 2.7.

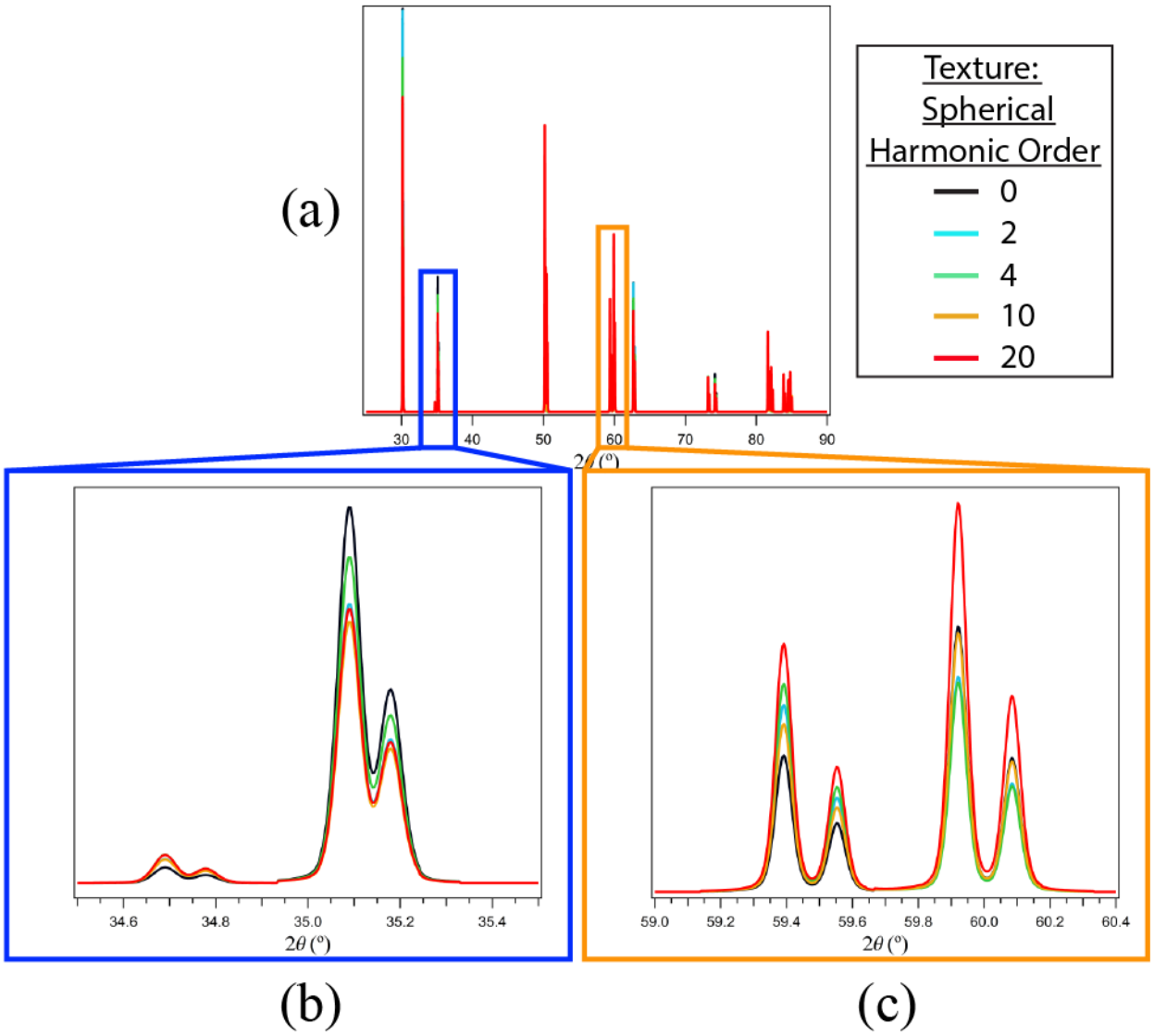


**Figure 2.7 The influence of the texture on the XRD spectra of the *t'* phase as defined by the spherical harmonic order. The (002) and (110) planes of the tetragonal phase are shown in (b) and the (103) and (211) planes of the tetragonal phase are shown in (c).**

## 2.4 Thin Foil Sample Preparation for Electron Microscopy Analysis

The thin foil specimens or lamella analyzed in this dissertation were prepared by the use of the *FEI Quanta 3D's* SEM/FIB/Omniprobe system available in the Laboratory for Electron and X-ray Instrumentation (LEXI) at UCI. A summary of this procedure as well as a typical finished lamella for a thermally aged APS sample is shown in Fig. 2.8. This procedure begins with depositing a protective layer of Pt onto the surface of the bulk sample where the lamella will be extracted. The deposition was carried out first using the electron beam and then subsequently with the ion beam. The electron beam deposit comes first as it will not mill away material but it is not a very efficient process, so a layer of Pt is deposited on top of the electron beam immediately after using the ion beam as shown in Fig. 2.8 (a). The final Pt thickness is more than 4 μm (only 300 nm of it from the electron beam) which is more than double what is prescribed in the LEXI standard-operating procedure. However, as removal of the Pt layer prevents continued milling of the lamella at the end of the procedure, it allowed for the thinning process to be extended.

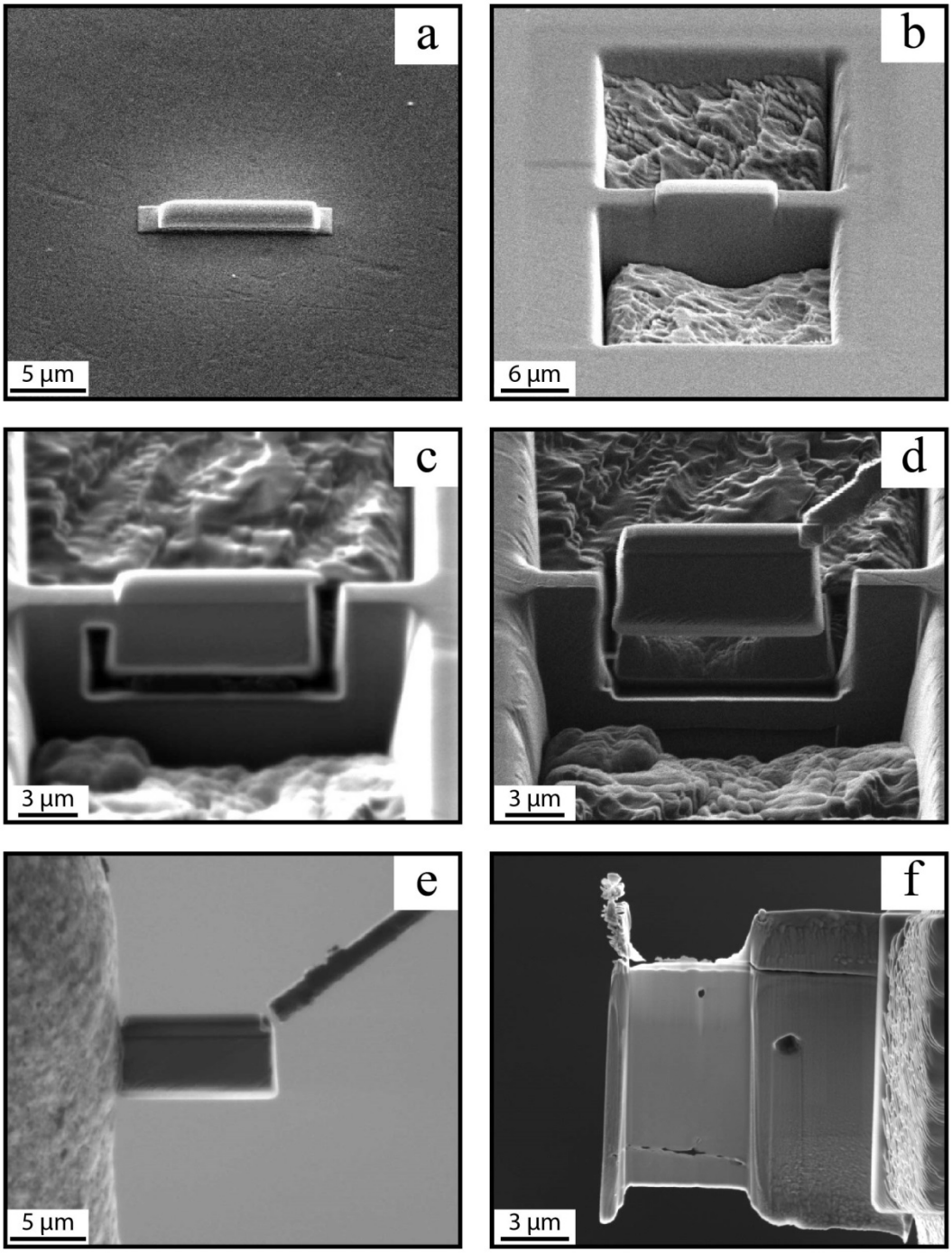


**Figure 2.8 Steps of the procedure used to prepare a lamella sample from the thermally aged samples. The micrographs shown in (a)-(e) were taken using an ion beam and are from the LEXI standard-operating-procedure for TEM sample preparation, while the micrograph shown in (f) was taken using an electron beam and is an example of a finished lamella from a thermally aged sample.**

Following the deposition of the Pt layer, bulk ion-beam milling was performed at large current values and the maximum accelerating voltage in order to remove large amounts of material that surround the resulting lamella. The sample is tilted to 52°, close to where the ion beam is supposed to be perpendicular to the sample. Large current values (greater than 7 nA) are used until the lamella is roughly 8 micron wide. At this point, the way in which the ion beam mills away material is changed from a stair-step method (*Regular cross-section*) to a less time efficient but more precise layer-by-layer removal method (*Cleaning cross-section*). The *Cleaning cross-section* milling is performed to reduce the taper in the lamella from the *Regular cross-section* and get the lamella thickness to be approximately 2 μm as shown in Fig. 2.8 (b). The lamella is then prepared for removal by tiling to a low angle (seven degrees) so that the ion beam will mill through the thickness of the lamella, leaving it attached to the bulk sample at only one end as shown in Fig. 2.8 (c).

Removal of the lamella is accomplished by the use of the *Omniprobe* ® AutoProbe ™ nano-manipulator. The *Omniprobe* is essentially a rod that can be controlled in the x-, y-, and z-axes on a sub-micron scale with motion rates as small as 0.1 μm/s. The *Omniprobe* is brought directly into contact with the lamella and then adhered to it by Pt deposition. After milling away the remaining end of the lamella that is attached to the bulk sample, the lamella is removed by moving the *Omniprobe* away from the sample in the z-direction as shown in Fig. 2.8 (d). The lamella is then moved to and attached to a standard TEM copper grid again using the Pt deposition method as shown in Fig. 2.8 (e). Once on the copper grid, the sample is milled to its final thickness of approximately 50 nm using successfully smaller accelerating voltage and current values. At this stage, the process becomes less of a regimented procedure and more of an

adaptive procedure that needs to be tailored for a given lamella—but a few points should be emphasized.

First, it is important to perform the final thinning with the smallest accelerating voltage possible. The energy given to the ions as set by the accelerating voltage is what determines the extent of the amorphous region that develops on the lamella as it is being milled. For Si, the general rule of thumb is 1 nm of an amorphous layer for each additional 1 kV. However, for harder materials like ceramics, it is anticipated that the amount of the amorphous region formed will be less than that of Si at a given accelerating voltage. The next point to emphasize is the importance of determining the tilt angle that is truly normal to both electron and ion beams. Experience has shown that the electron beam is not usually normal to the lamella/copper grid at zero degrees but is actually off by 2 or 3 degrees depending on the grid used. Therefore, the user needs to determine the actual point at which the lamella/grid is normal to the electron beam by tilting the stage and viewing the resulting image. Once this tilt angle is determined the same difference in tilt can be used to find the true normal point of the ion beam—e.g. if the electron beam normal is at a tilt angle of -2° than the ion beam normal will be at a tilt angle of 50° as opposed to 52°. Finally, it is important to emphasize that as the sample is milled to thinner dimensions, it will likely begin to bend or warp due to the loss of mechanical constraint from the surrounding material. This is especially true for the APS samples that have large residual stresses due to the rapid cooling that occurs as the material is deposited. Therefore, it is advantageous to keep the sides and ends of the lamella thicker (of the order of 1 μm) to keep it mechanically restrained better.

## 2.5 Scanning Transmission Electron Microscopy

STEM analysis was performed on the thermally aged samples for three main reasons: 1) to determine if the lamellae—i.e. the thin foil sample prepared by FIB milling—was thin enough for TEM analysis, 2) to perform high-angle annular dark field (HAADF) imaging of the lamellae, and 3) to perform Energy-Dispersive X-Ray Spectroscopy (EDS) analysis of the lamellae. STEM imaging was performed for point 1) because the process of obtaining an image by STEM is much easier than obtaining an image with the TEM. This is in part due to the fact that the STEM instrumentation is 20 years newer than that of the current TEM, but also due to the much simpler process of tuning the electron beam in the SEM than in the TEM. In regards to point 2), the STEM imaging was useful in providing contrast in images due to changes in mass by isolating electrons scattered through an angle larger than ~3° [40]. This helped image the domain microstructure of the lamellae because adjacent domains will have slightly different mass and therefore contrast as shown in Fig. 2.10. Finally, in regards to point 3), EDS was performed with STEM in order to quantify the chemistry of the domains in the lamellae samples. Although EDS could be performed with the TEM, it is limited because it can not identify regions of mass contrast due to the lack of a HAADF detector. Also, moving the sample exact dimensions was not possible in the available TEM, which would have made it difficult to do EDS line scans across nano-size domains.

The procedure for STEM imaging is straightforward as the only variable that can be adjusted is the beam current. The accelerating voltage needs to be fixed at the highest value possible (i.e. 30 kV) in order to allow for the highest possibility of electron transmittance through the sample. Also, the working distance is not a parameter that can be adjusted either because it is fixed by the height of the STEM stage that houses the sample. For the same reason,

tilting the sample is not an option with the STEM stage. Therefore, the only parameter that can be adjusted to modify the image is the beam current. The same balance between probe size and image contrast occurs when imaging with the STEM as it does for SEM. A current value of 100 pA—with an approximate probe size of 25 nm—was determined to be optimal to capture the contrast of the domain microstructure of the aged samples. Forming a bright-field, dark-field, or HAADF STEM image is a simple manner of either using the center, inner-annulus, or outer-annulus portions of the STEM detector, respectively. Performing EDS in the STEM is the same as performing it in the SEM, with the advantage of having a much smaller interaction volume when the EDS is performed in the STEM due to the nanoscale thickness of the lamellae.

### 2.6 Transmission Electron Microscopy Analysis

TEM analysis was performed on the thermally aged samples to supplement the STEM analysis with information on the orientation of the domain microstructure as well as local phase analysis. Information on the orientation of the domains was provided by dark-field imaging where scattered electrons are selected to form an image from an electron diffraction spot off the optical access. This is achieved by first inserting the selected-area aperture into the imaging plane with all other apertures removed in order to create a virtual aperture at the plane of the specimen [40]. The selected area diffraction (SAD) pattern for the grain being probed can now be observed while in diffraction mode—an example of which is shown in Fig. 2.9 (b). Keeping the selected-area aperture inserted, the objective aperture is then inserted and positioned to select an off-axis electron diffraction spot. The selected-area aperture is then removed to form a dark-field image from the selected electron diffraction spot. It should be noted that a dark-field image formed this way will introduce aberrations into the image due to being off the optical axis. The magnification of the TEM dark-field images used in this dissertation was not high enough to cause issues in affecting the resolution of the dark-field images taken. However, if the resolution

was affected, an alternative method called centered dark-field operation could be used to resolve the off-axis problem.

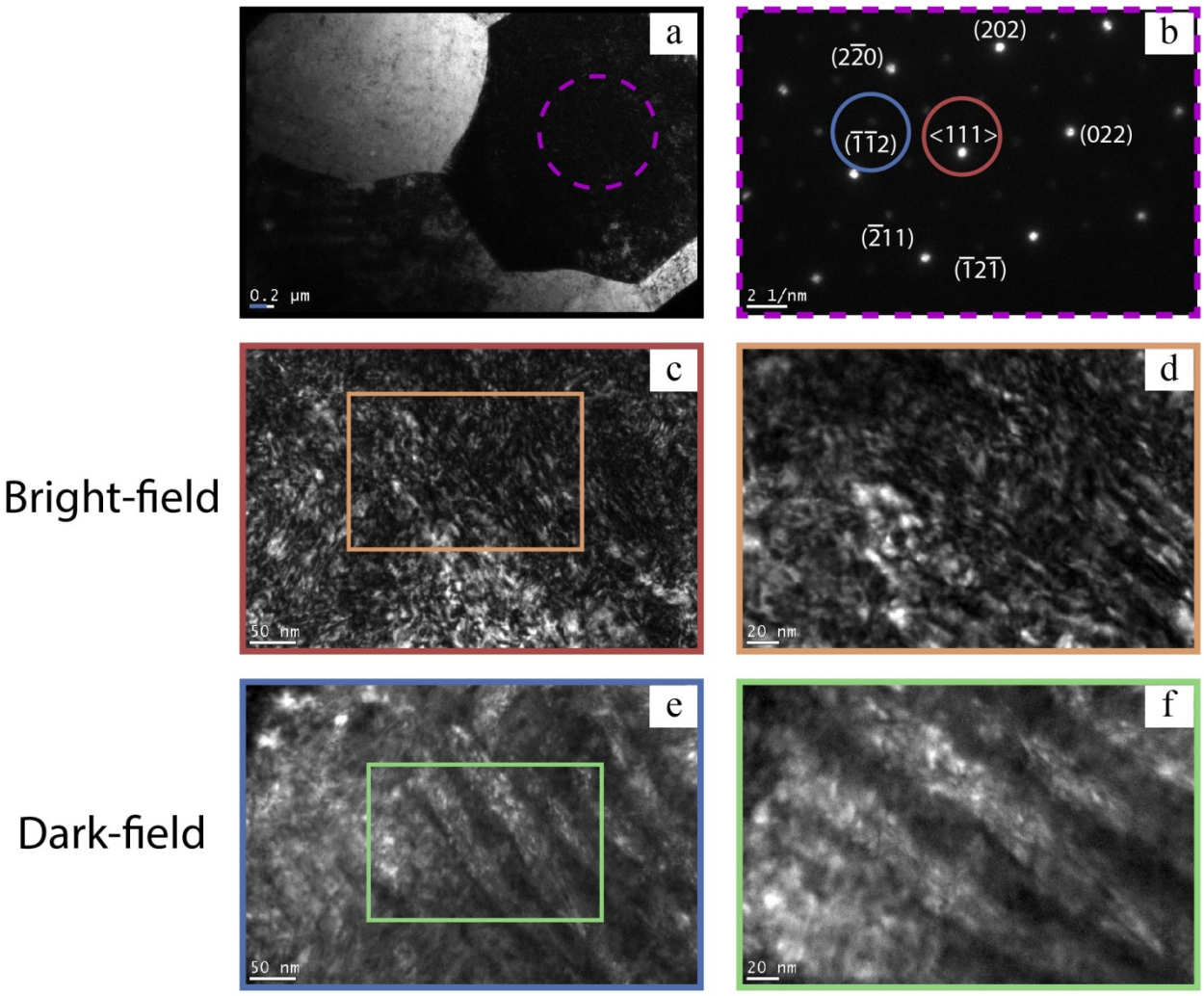


**Figure 2.9 TEM images and a diffraction pattern showing: (a) a bright-field image with a grain displaying "Bragg contrast", (b) a diffraction pattern from a grain showing "Bragg contrast", (c) and (d) bright-field images from the electron diffraction spot shown in (b), and (e) and (f) dark-field images from the electron diffraction spot shown in (b).**

The contrast in dark-field images can provide information on mass/thickness changes—although a darker contrast indicates a lower mass or thinner area which is the opposite of what it

means in a bright-field image—but it is now also convoluted with contrast from changes in orientation. Figure 2.10 shows a comparison of the TEM dark-field images and HAADF STEM images from the same regions of the dry- and humid-aged samples. The HAADF STEM images are only showing differences in contrast due to chemistry. There is a close correlation in the bands of contrast between the TEM dark-field images and the HAADF STEM images indicating that the differences in contrast of the TEM dark-field images are highlighting the different orientations of neighboring domains.

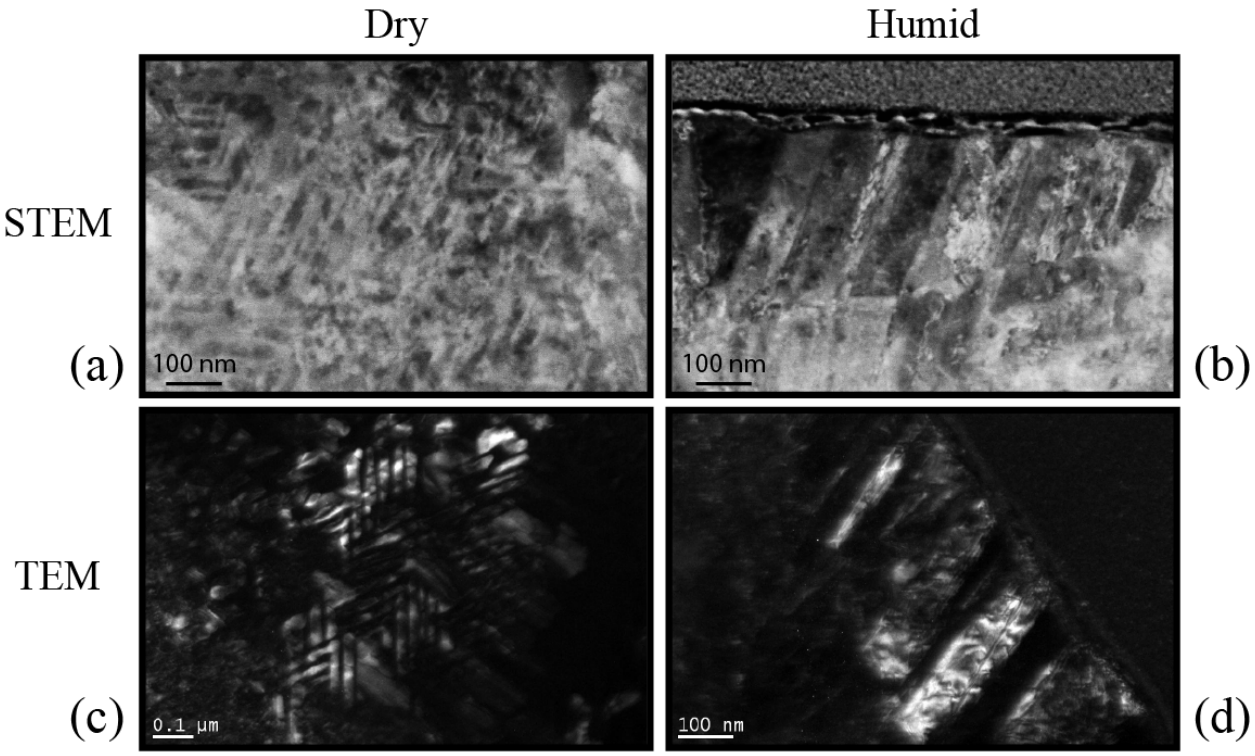


**Figure 2.10 HAADF STEM images (a) and (b) of the 16.7 K (224 h) dry- and humid-aged sample as well as dark-field TEM images (c) and (d) from similar regions of each sample.**

The TEM was also used to form diffraction patterns from grains within the aged samples in order to identify the phases present. This can be accomplished in two ways: 1) by convergent beam electron diffraction (CBED) or 2) by SAD. CBED can provide a wealth of crystallographic orientation and can generate diffraction patterns from grains smaller than 100 nm. However,

CBED is not the best method to use when the diffraction spots are close together or when the grains are large (greater than 1 μm) [40] as is the case in the thermally aged samples. SAD patterns were formed in a manner as described earlier by inserting the selected-area aperture and removing the objective aperture while in diffraction mode with a parallel beam. The resulting SAD pattern is usually not readily identifiable and it is therefore necessary to tilt the specimen until the Bragg diffraction criteria is satisfied. Experience has shown that locating the zone axis is useful when trying to identify major diffraction planes within the sample. This can be achieved by converging the beam and forming a CBED pattern from the area of interest. Kikuchi bands can now be observed and by tilting the specimen the bands can be traced to a zone axis where the bands intersect with one another. Even if this zone axis does not reveal the desired reflection, it can serve as a marker to locate the current crystallographic direction and act as a means to calculate the tilting necessary in order to find the desired reflection. An example of a SAD pattern from a thermally aged sample is shown in Fig. 2.9 (b).

# 3 Chapter 3: Burner Rig Evaluation of the Type I Hot Corrosion of Marine Gas Turbine Coatings in Traditional and Synthetic-Blend Fuel Combustion Environments


## Abstract

Type I hot corrosion exposure of metallic overlays was performed in a burner rig using two different types of fuels—NATO F76 diesel (F76 test) and a blend consisting of 50% hydroprocessed renewable diesel (HRD) derived from algae and 50% NATO F76 diesel (Blend test) by volume. The burner rig tests simulated a marine combustion environment by providing automated thermal cycling and the injection of 10 ppm of sea salt into the combustion flame. Post-testing measurements of the average surface loss and oxide/sulfide penetration into the sample show statistically larger values for the Blend test as compared with the F76 test for many of the metallic overlays. The microstructure of the samples look similar between tests for the majority of the coatings. However, for the NiAl and Pt-modified NiAl coatings there are sections of the coatings that look very different for the Blend test. Instead of a dense, compact scale these regions of the coating have porous scales that contain sulfides and residual coating. The depletion of Al in the coatings adjacent to these regions is much more significant as compared to the regions of the coatings that have a compact scale on top. The Blend test combustion conditions are proposed to cause a more basic fluxing condition at the scale/deposit interface, causing the scale to be dissolved at a faster rate than that compared with the F76 test. Once the scale is dissolved, the deposit comes into direct contact with Ni causing sulfides to form in the porous scale. During the thermal cycle the sulfides solidify and as the samples are heated up again a new scale needs to form on this region of the coating—thus causing enhanced depletion in these coating locations. Therefore, the Blend fuel enhances the Type I hot corrosion attack in NiAl and Pt-modified NiAl coatings by promoting a more basic fluxing condition at the scale/deposit interface.

## 3.1 Introduction

As the largest consumer of energy in America, the different branches of the US military have actively sought to reduce petroleum use [41]. Specifically the United States Navy has the goal of reducing petroleum use in its fleet by 50% by 2020 [5]. To reach this goal, the US Navy has implemented a blended-alternative fuel in its surface ships [41]. While this Blend fuel is currently being used in service, the mechanisms behind the corrosive attack on hot-section gas turbine components of this combusted Blend fuel are unknown. This corrosive attack at elevated temperatures is termed hot corrosion and occurs in gas turbines used in marine environments. Marine gas turbines have traditionally made use of metallic overlays to protect gas turbine blades and other components from hot corrosion and oxidation. It is therefore critical to understand how the combustion of alternative fuel-blends may affect the hot corrosion mechanism so that next generation marine-metallic overlays can be designed to withstand this attack.

In marine turbines, the combination of sea salt and the presence of sulfur from the fuel and/or air cause a hot corrosion attack on the first-stage turbine components that can lead to engine failure within hundreds of hours if not properly designed against [42]. The hot corrosion attack is a deposit-induced corrosion that occurs at temperatures in excess of 650 °C and is categorized into two types—Type I—high-temperature hot corrosion—and Type II—low temperature hot corrosion [28]. The subject matter of this chapter concerns Type I and the influence of the fuel on this type of hot corrosion will be the focus of this chapter.

Type I hot corrosion is most prevalent at high temperatures ranging from 850-950 °C and low partial pressures of $p_{SO_3}$ (less than $1 \cdot 10^{-4}$ atm) [28]. The Type I attack occurs in two stages, an initial incubation stage and a subsequent propagation stage. During the initiation stage, there is little evidence of attack of the metallic overlay but this stage does involve an evolving

composition of the deposit, scale, and alloy [43-45]. The propagation stage begins when the deposit comes into direct contact with the metallic overlay, resulting in a rapid and usually catastrophic degradation. A common proposed mechanism for the transition from the initiation to the propagation stage is the fluxing or dissolution of the protective oxide that forms on top of the metallic overlay in-service [46-48]. Given the high temperatures and low $p_{SO_3}$ of Type I conditions, a basic—as opposed to acidic—type of fluxing of the protective scale occurs provided that the deposit is $Na_2SO_4$ and there are no refractory elements present in the coating [30, 43, 49].

The role of biomass-derived fuels on the Type I hot corrosion attack of metallic overlays is currently unknown but compositional differences of these fuels from conventional fuels suggest that there may be a difference. Biomass fuels derived from grass and wood were found to have higher levels of K and Na than coal [50]. Higher alkali metal contents could influence Type I conditions by changing the basicity of the deposit and therefore the solubility of the alloys scale [47]. A more recent analysis of fuel content for biomass-derived fuels, found differences of minor and trace elements from commonly used coals [51]. The biomass-derived fuels had a chlorine content twice that of the coal fuels and less than a tenth of the sulfur content by wt%. The different ratios of such contaminants may lead to a different type of hot corrosion attack in biomass-derived fuels even though the sulfur content is lower. For example, tube-furnace exposure tests on Pt-aluminide coatings at 700 ºC were performed by coating the samples with sodium/potassium sulfates and lead chlorides in order to simulate the deposits of fuel gases produced by the gasification of coal/biomass fuels [52]. A hot corrosion Type II attack was observed and the extent of the attack varied depending on the ratios of Na/K/Pb.

Besides differences in trace elements, HRD blended fuels have been shown to have differences in the atomization and combustion characteristics from pure diesel fuels. The time-scale for the physical processes of combustion is much larger than that of the reaction kinetics and are therefore more important in terms of understanding the combustion of spray flames [53]. These physical characteristics are dependent upon the physical properties of the biodiesels—e.g. kinematic viscosity, density, surface tension, and cetane number. These properties were shown to increase with increasing amount of blended fuel for some blended biodiesels [53]. These changes in the physical properties of the fuel altered the combustion characteristics of the blended fuel by decreasing the injection velocity, peak injection rate, and injection delay as well as increasing the peak combustion pressure compared to that of the pure diesel fuel [53]. However, recent work on the Blend fuel confirms the higher cetane number for a HRD blended fuel but shows the opposite trend for the dynamic viscosity and density [41, 54]. As the amount of the Blend fuel increased in the diesel, the dynamic viscosity and density decreased. The high cetane number of the blended fuel indicates a higher compression ignition quality relative to the diesel fuel [53, 55]. Also, an improved atomization for the Blend fuel—as indicated by its lower dynamic viscosity —can cause shorter fuel-evaporation times and increase the time allowed for the corresponding reaction kinetics. While full scale engine tests have shown satisfactory combustion performance of the Blend fuel [56], an analysis is needed to determine how the combustion of this fuel affects the degradation of gas turbine coatings by Type I hot corrosion.

In order to determine whether or not the Blend fuel will have a different hot corrosion mechanism it is vital to conduct testing conditions in combustion environments that simulate gas-turbine conditions. While many hot corrosion studies employ a “deposit-recoat” method of applying the hot-corrosion deposit—e.g. $Na_2SO_4$—to the sample because of its ease of

application, they do not capture the combustion environment of a gas turbine [43, 49]. Experimental test cells known as burner rigs have been employed for more than 40 years as a way to simulate gas-turbine combustion conditions without the expense of a full-scale engine test [57]. Burner rigs allow for fuel combustion to occur during experimental testing, causing experimental samples to be exposed to the combustion stream. Therefore, in order to understand how the combustion of the Blend fuel affects the Type I hot corrosion mechanism, it is necessary to perform experimental testing in a burner rig. Here we examine the Type I hot corrosion behavior of four industry coatings using a burner rig with the sole variable being fuel type. Two burner rig tests with automated thermal cycling were performed to evaluate mechanistic differences in the degradation of metallic overlays due to differences in fuel alone.

## 3.2 Experimental Procedures

### 3.2.1 Samples and Pre-Testing Procedures

Industry-standard metallic overlays and substrate material systems used in current marine propulsion gas turbines were utilized in testing conditions. These coatings encompass the two major types of coatings employed in marine propulsion gas turbines—MCrAlX (M = Ni and/or Co; X = Y or Hf) and Pt-modified Ni-aluminides. These coating systems make up the core of hot section gas turbine materials used in marine propulsion and any proposed fuel to be implemented in the US Navy fleet must be tested with them. Therefore, these coatings were used in burner rig testing in order to determine if the proposed Blend fuel would affect the hot corrosion mechanism of the state-of-the-art coating systems.

The samples were provided by the manufacturers in the form of 6.4 cm long pins with a substrate diameter of 3.2 mm and coating thicknesses ranging from 30 to 120 µm depending on the manufacturer and type of coating. The diameters of the as-received pins were measured at three locations along the length of the pin (6.4 mm, 20.2 mm, and 40.4 mm from the top of the

pin) using optical micrometers so that these diameters can be compared to post-testing measurements at the same locations. Samples were embedded in a moldable alumina-based ceramic that was housed in a cylindrical, carousel cup made of a Hastealloy®X alloy. The samples were thermally and electrically isolated from one another by being nominally spaced 3.2 mm from one another and 6.4 mm from the carousel edge. During testing, the samples were oriented in the carousel so that they were perpendicular to the combustion stream and rotating at a constant speed of 29 rpm.

### 3.2.2 Burner Rig Testing

Samples were exposed to Type I hot corrosion conditions in an enclosed burner rig to allow for a necessary p$SO_3$ to develop in the environment to ensure a similar hot corrosion environment as that of a gas turbine used for marine propulsion. Two 700 h burner rig tests were performed by ramping resistive molybdenum di-silicide heating elements at 5 °C/min to 900°C. Samples were held at this temperature for 23 hours and then thermally cycled to ambient temperature for 1 hr. The sole difference between the two tests was the fuel used—Test 1 used the Blend fuel while Test 2 used the F-76 fuel. To simulate a marine propulsion environment, ASTM-specified sea salt was introduced into the combustion flame at a concentration of 10 ppm. This sea salt concentration was an order of magnitude greater than that would occur in a marine turbine environment. The increased salt concentration was necessary in order to accelerate hot corrosion conditions in the time-span of a 700 h test. To ensure that there was no difference between the tests except for the fuel, the Blend fuel was intentionally doped with 0.5 wt% of sulfur to match that of the F-76 fuel.

### 3.2.3 Sample Preparation

Post-testing, pins were agitated in DI water to store the water-soluble pin deposits. The pins were then sputter coated with gold and electroplated with copper to help protect the corrosion products from pull-out during the grinding process. This copper layer resulted in a harder layer between the embedding epoxy and metallic overlay minimizing the exposure of the corrosion products during metallographic grinding/polishing. The pins were then dipped in epoxy twice to prevent loss of the oxidation/sulfidation products during the cutting process. Finally, the epoxy-dipped pins were sectioned using a diamond blade and polished to 1 μm using standard metallurgical techniques.

### 3.2.4 Sample Analysis

Measurements were made on three different cross-sections for each sample to record the average surface loss, average penetration, and maximum penetration as shown in Fig. 3.1. These measurements were made using an optical microscope with a modified stage. The stage position could be adjusted with a precision of 1 μm using digital micrometers. The average surface loss and penetration measurements were made at 20º increments for a total of 18 locations around the pin. The maximum penetration measurement was made by recording the deepest oxide/sulfide penetration into each cross-section. These measurements were made on three cross-sections per pin and there were five pins for each material group per test. Therefore, the surface loss, penetration, and maximum penetration results for one material group from one test are the result of averaging more than 270 measurements.

The microstructure and chemistry of the exposed samples were analyzed using scanning electron microscopy (SEM) and electron dispersive spectroscopy (EDX), respectively. The SEM images were taken using a backscatter electron detector to visual the phase contrast of the

polished cross-sections. Qualitative EDX maps were used to determine the locations of sulfide and oxide reaction products within the exposed coatings. Quantitative EDX was used to determine the evolution of the chemistry in the coating after exposure as well as to construct line scans across the coatings to identify the extent of elemental depletion within the coating. These analyses were performed at the Laboratory for Electron and X-ray Instrumentation at UC, Irvine.

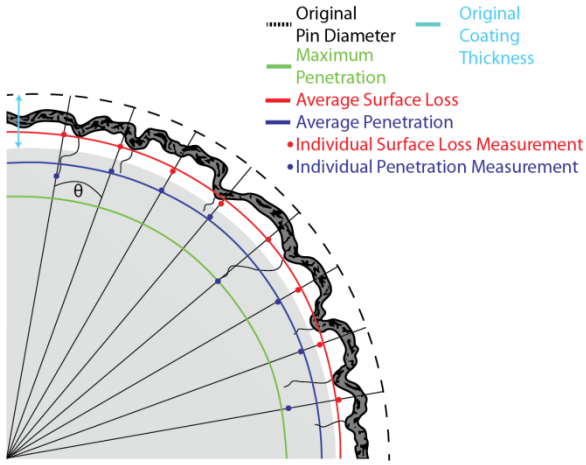


**Figure 3.1 A schematic of the statistical measurements performed on samples exposed in the burner rig at three cross-sections along the length of the pin.**

## 3.3 Results

### 3.3.1 Statistical Measurements

The average surface loss, average penetration, and max penetration values for the burner rig exposed coatings are shown in Fig. 3.2. The measurement values from the top, middle, and bottom cross-sections have been averaged together for the coatings because no consistent trend was observed along the length of the pin for any of the material groups.

The Pt-modified NiAl Mar-M-247 material group has very similar values between the tests. While the standard deviation is always less than 30% of the average surface loss or penetration value, the measurements do not indicate differences between the tests outside the

standard deviation. The maximum penetration values also do not vary outside the standard deviation for the tests.

The Pt-modified NiAl CMSX material group does show statistical differences between the tests. The Blend test has a larger average surface loss, average penetration, and max penetration when compared with the F76 test. The most notable differences between the tests are the penetration results. There is a significant difference between the average penetration and surface loss measurements for the Blend test, while nearly no differences for that of the F76 test. The average penetration of the Blend test is more than three times as large as that of F76 test. The maximum penetration values show a similar trend between the tests as the average penetration results.

For the NiAlCoCr/In-738 material group, the average surface loss, average penetration, and maximum penetration are larger for the Blend test than for that of the F-76 test. The maximum penetration values are completely outside the standard deviation while the average penetration values have average values outside of the standard deviation—but the standard deviations do overlap for these latter measurements. The NiAlCoCr/In-738 material group had less attack than the Pt-modified NiAl coatings for the Blend test, but had an attack similar to the Pt-Modified NiAl/CSMX material group for the F76 test. In terms of showing differences in attack between the fuel tests, the NiAlCoCr/In-738 material group shows a larger difference than the Pt-Modified NiAl/Mar-M-247 but a smaller difference than the Pt-Modified NiAl/CSMX material group. For these three material groups, the amount of attack has either been larger for the Blend test or the same amount as the F76 test—as in the case of Pt-Modified NiAl/CMSX-4 material group.

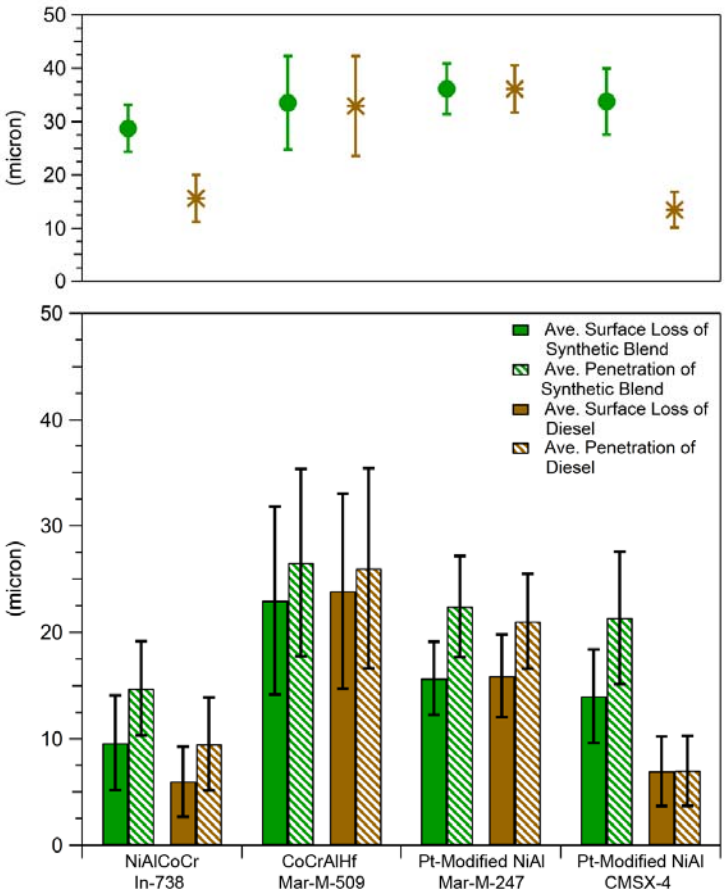


**Figure 3.2 Average surface loss, average penetration, and maximum penetration measurements for the exposed burner rig samples of both tests. Each data bar is the averaged result of 270 measurements on three different cross-sections from five different pins.**

### 3.3.2 NiAlCoCr Coatings on an In-738 Substrate

The coatings and scales of the exposed samples are shown in the backscatter electron images of Figs. 3.3 and 3.4, respectively. Most of the cross-sections show tightly adhering alumina scales suggesting that the samples are in an incubation stage. However, on the Blend exposed samples there are locations on the cross-sections showing large penetration into the coatings and sulfide formation at the leading edge of the attack suggesting these locations are in the propagation stage of hot corrosion.

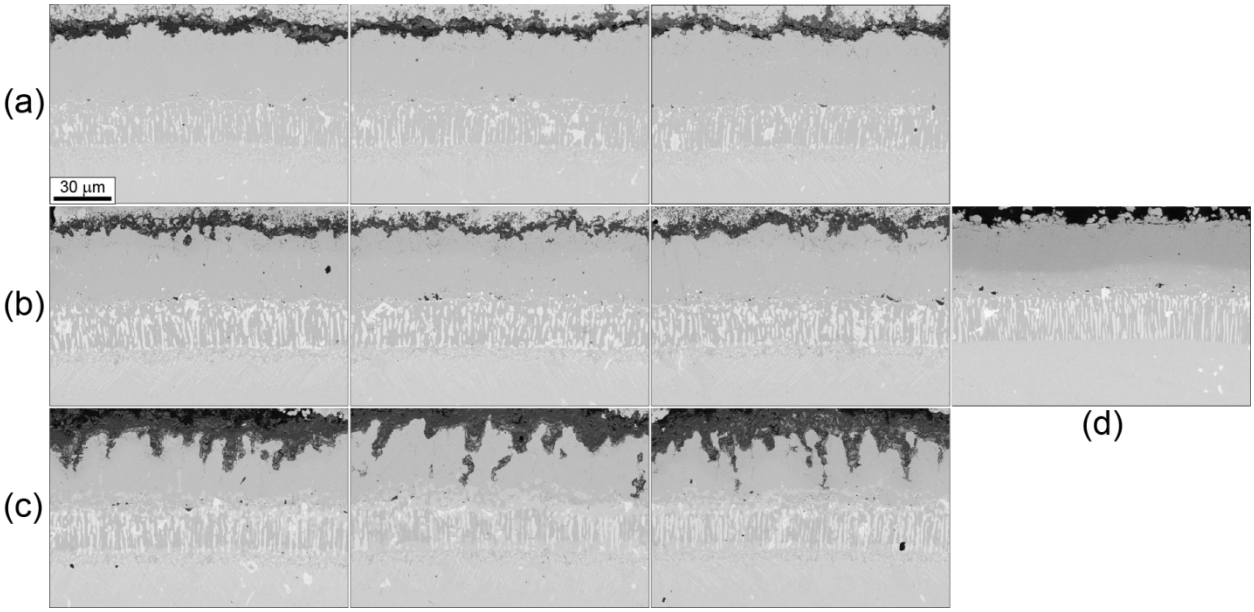


**Figure 3.3 Cross-sectional BSE images of the NiAlCoCr coatings showing the (a) F76 samples, (b) Blend samples, (c) Blend samples with deep penetration, and (d) As-received sample.**

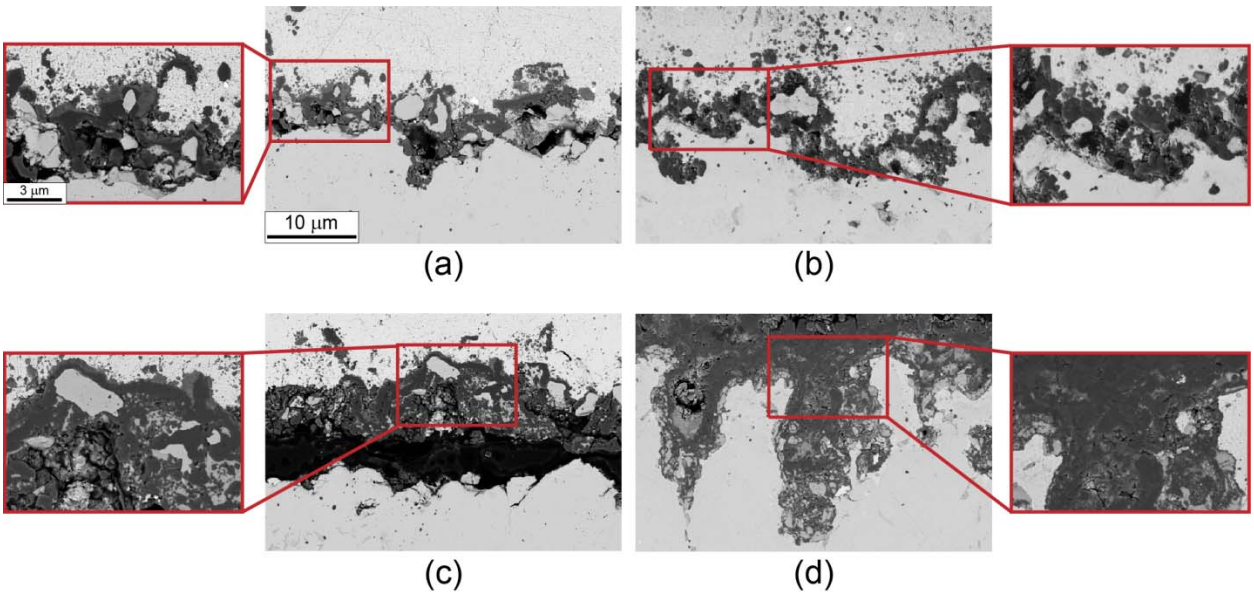


**Figure 3.4 Cross-sectional BSE images of the NiAlCoCr coating scales showing the (a) typical F76 scale, (b) the worst F76 scale, (c) typical Blend scale, and (d) the worst Blend scale.**

The coating chemistry does not change between the two tests as shown in the pie graphs of Fig. 3.5. The exposed coatings have been depleted of aluminum and chromium relative to the

as-received coating as expected. From the phase diagram of Fig. 3.6, the as-received coating chemistry corresponds to the β phase and it remains in this phase field after it is depleted due to the burner rig exposure.

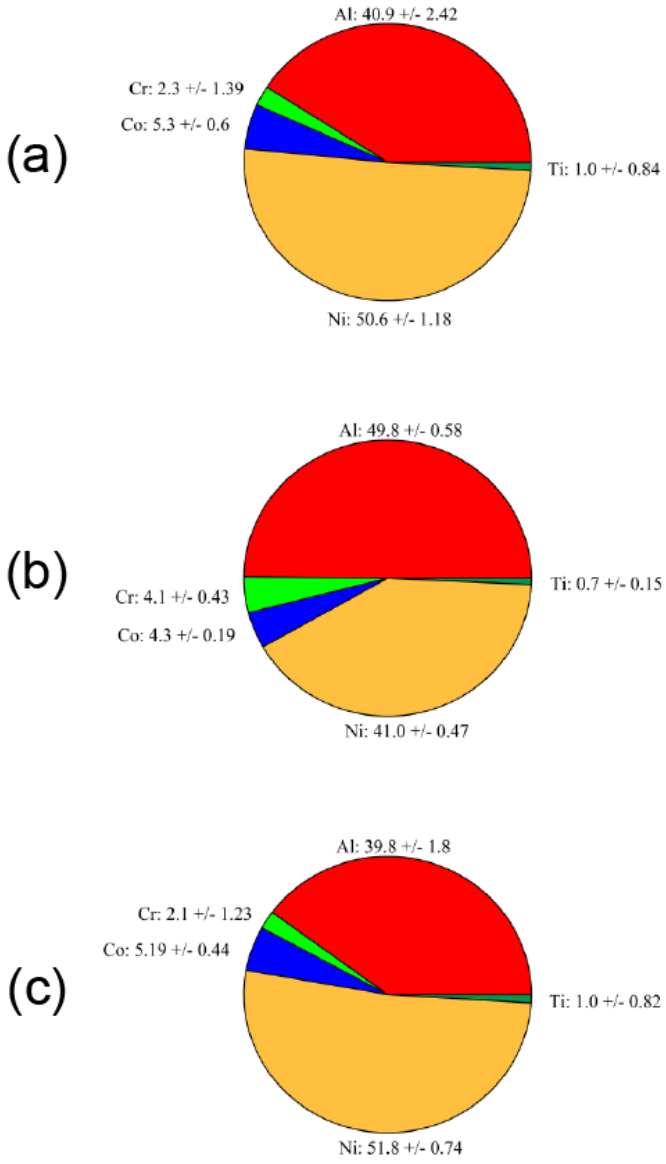


**Figure 3.5 EDX composition of the entire NiAlCoCr coating for the (a) F76 sample, (b) As-received sample, and (c) Blend Sample.**

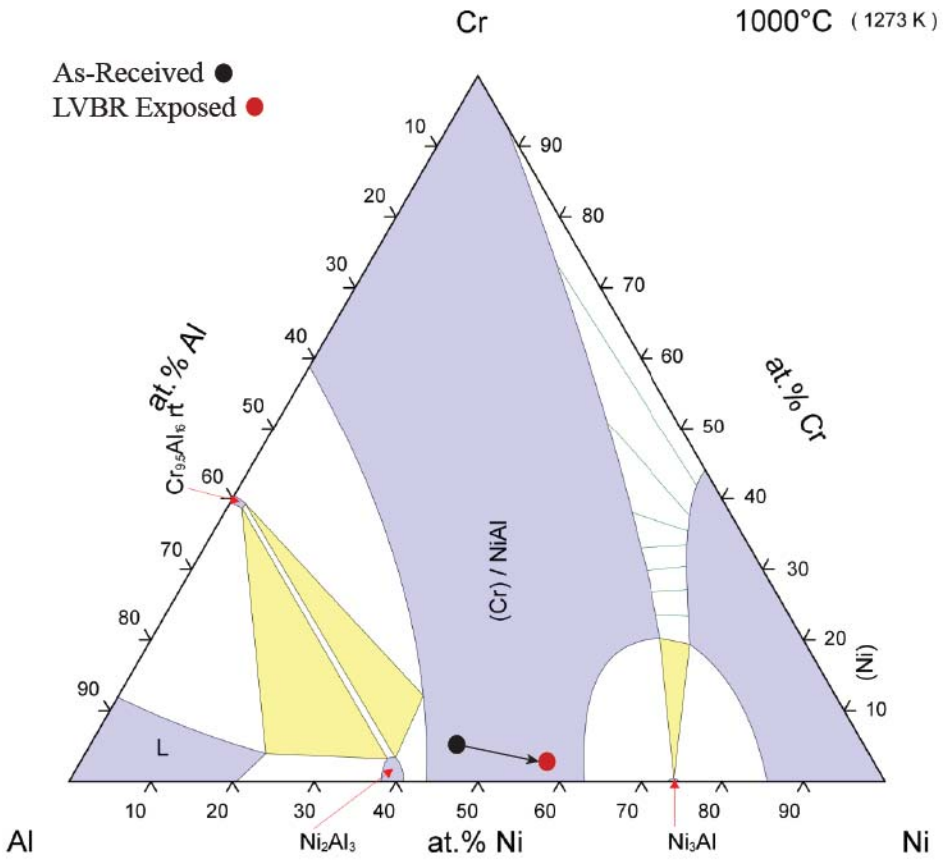


**Figure 3.6 Isothermal Ni-Al-Cr phase diagram with the compositions of the as-received coating and exposed coatings superimposed on the diagram at 1000 ºC.**

The EDX linescans of Figs. 3.7 and 3.8 show the evolution of the NiAlCoCr coating chemistry before and after Burner Rig exposure with the F76 fuel, respectively. Figure 3.7 shows significant compositional gradients for all elements detected. The coating is rich in Al at the top of the coating which decreases rapidly towards the diffusion zone as Ni increases. Also in the as-received coating, Co increases inconsistently towards the diffusion zone while the Cr concentration resembles a parabola across the coating. Ti is not detected within the coating until 10 microns from the diffusion zone. Figure 3.8 shows the compositional profile for the F76 exposed coating which had a similar profile as the Blend exposed coating. Ni has been enriched at the expense of Al depletion in the exposed coating and the compositional gradients for these

elements are significantly less across the coating than it was for the as-received state. The minor components of the coating have much more linear gradients across the coating but have similar concentrations close to the diffusion zone as they did for the as-received state.

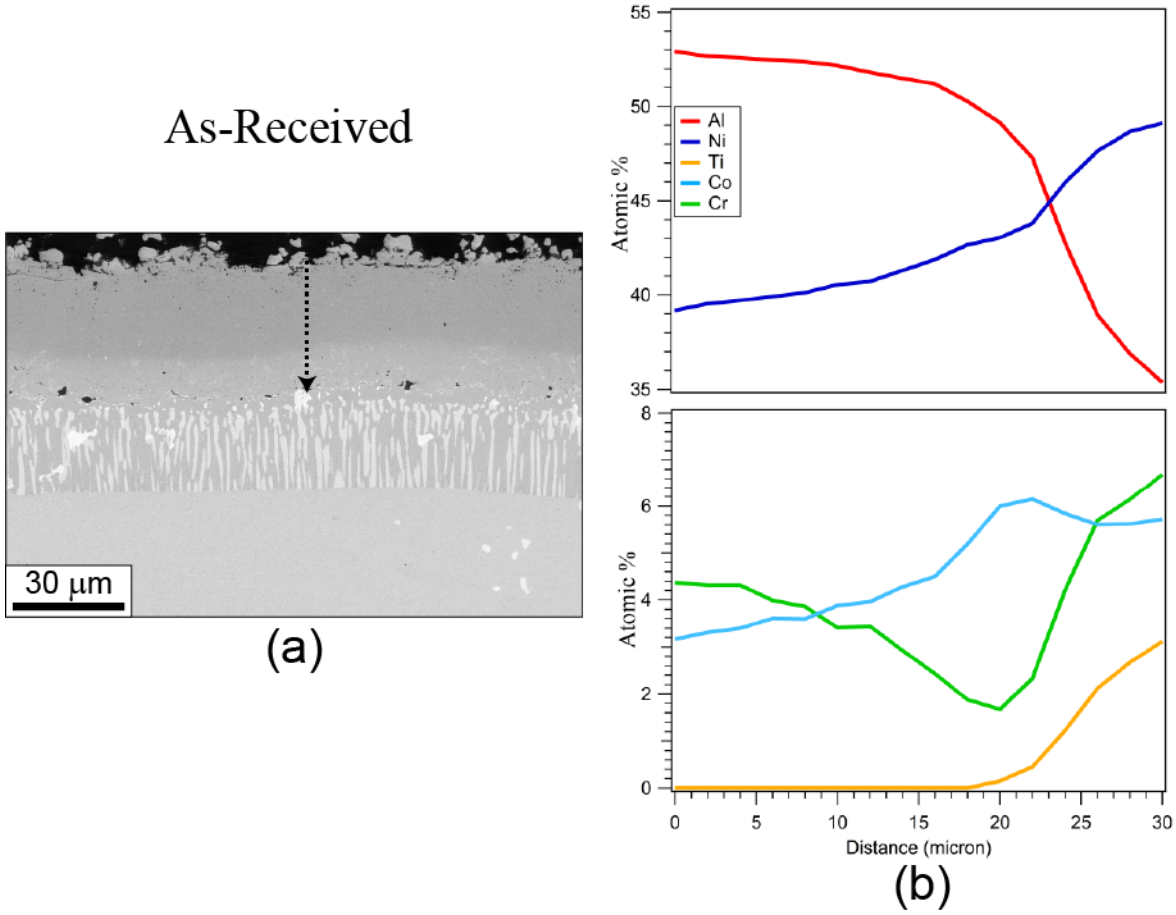


**Figure 3.7 EDX line scan of the as-received NiAlCoCr coating showing the (a) corresponding BSE image and (b) elemental profiles for the coating.**

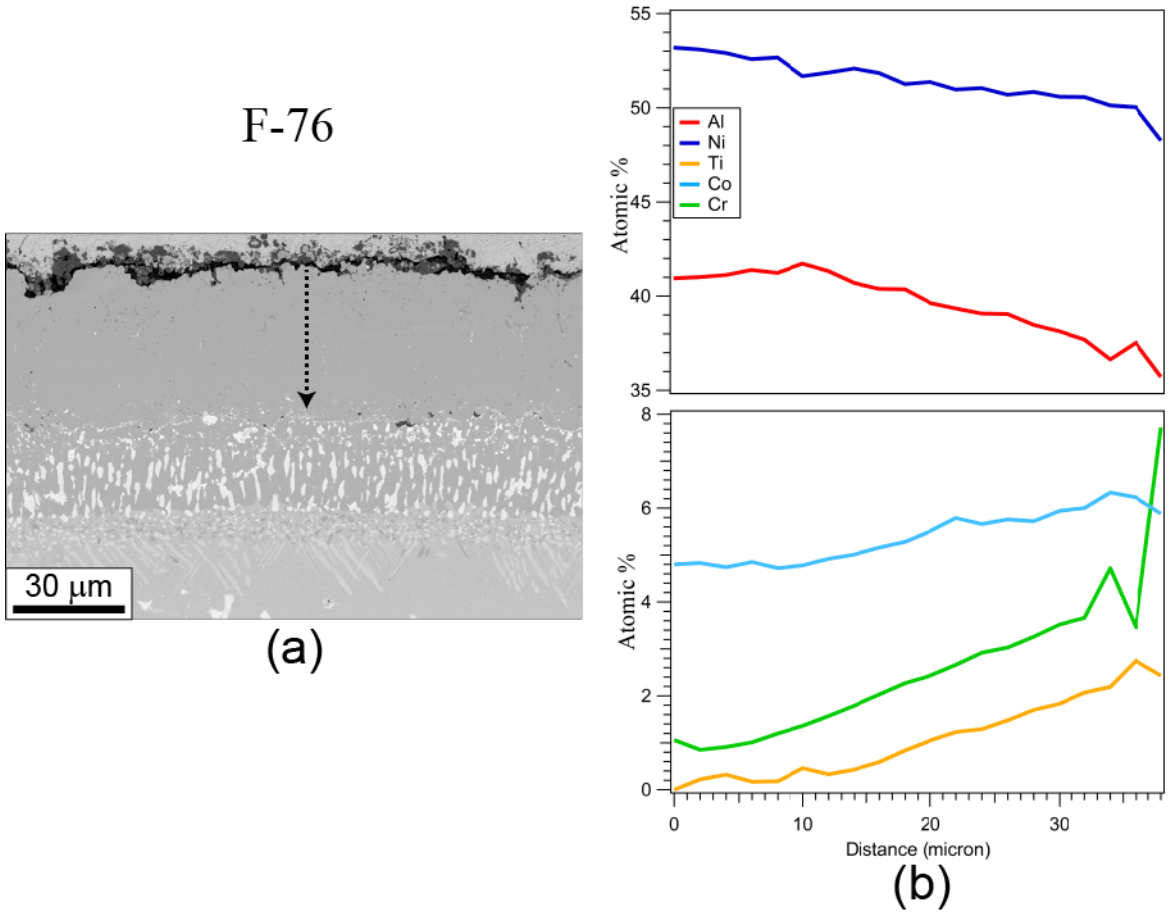


**Figure 3.8 EDX line scan of the F-76 NiAlCoCr coating showing the (a) corresponding BSE image and (b) elemental profiles for the coating.**

### 3.3.3 Pt-modified NiAl Coatings on a CMSX-4 Substrate

BSE images of the as-received and exposed Pt-modified NiAl coatings on a CMSX-4 substrate (CMSX-4 NiAlPt) are shown in Fig. 3.9. There is noticeably more z-contrast at the top of the as-received coating than for any of the exposed coatings. When there is a compact oxide on the exposed coatings, the microstructures look similar for the different tests at this field of view. However, a portion of the cross-sectional pin from the Blend test does not have a compact oxide. Instead, there are portions of the coating that have deep oxide penetrations with sulfides present at the leading edge and perimeter of the oxides.

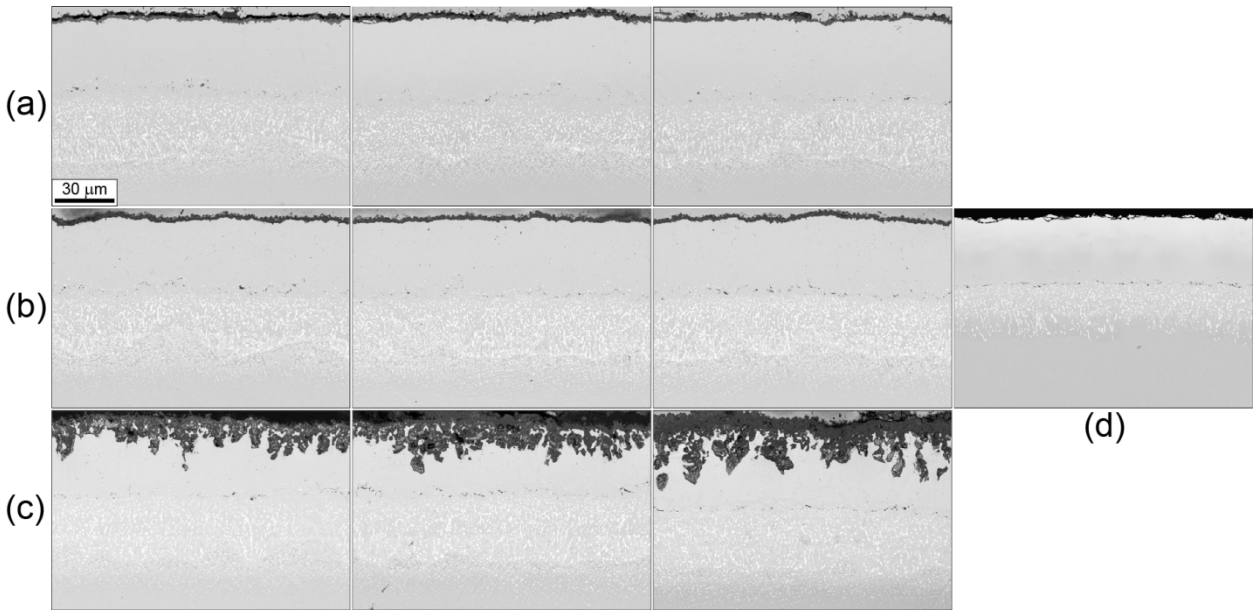


**Figure 3.9 Cross-sectional BSE images of the CMSX-4 NiAlPt coatings showing the (a) F76 samples, (b) Blend samples, (c) Blend samples with deep penetration, and (d) As-received sample.**

An SEM montage of a CMSX-4 NiAlPt coating cross-section exposed in the Blend test confirmed a non-uniform penetration around the coating circumference as shown in Fig. 3.10. Approximately one-third of the circumference had "finger-like," oxide penetrations into the coating, while the rest showed only a thin scale on top of the coating. This non-uniform penetration is not observed in the bottom cross-sections of the F76 coatings in SEM images or in the statistical measurements for this test.

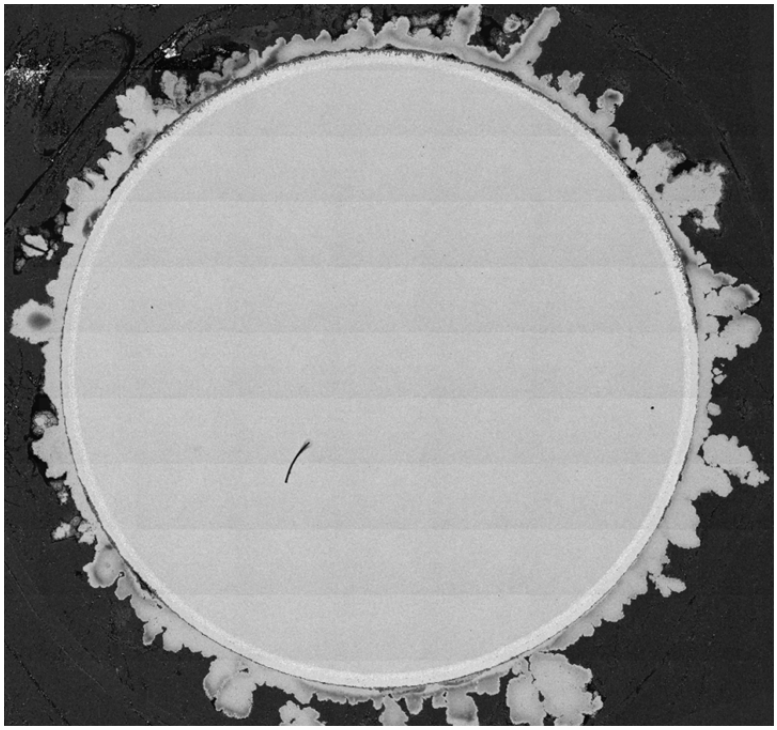

**Figure 3.10 Variation of the penetration along a CMSX-4 NiAlPt coating cross-section exposed in a Blend test.**

The alumina scales formed on top of the Pt-modified NiAl coatings after exposure are shown in Figs. 3.11 and 3.12. Three images are shown in each figure—the F76 scale, a compact Blend scale, and a deep penetration Blend scale. The compact Blend scale has elongated alumina grains on the gas-side of the scale that are not found in the F76 scale. The depth of the oxide scale for the deep penetration Blend scale is more than three times greater than that of the compact Blend scale or the F76 scale. The contrast of the deep penetration Blend scale also shows the presence of sulfides that are absent in the compact Blend scale as well as the F76 scale.

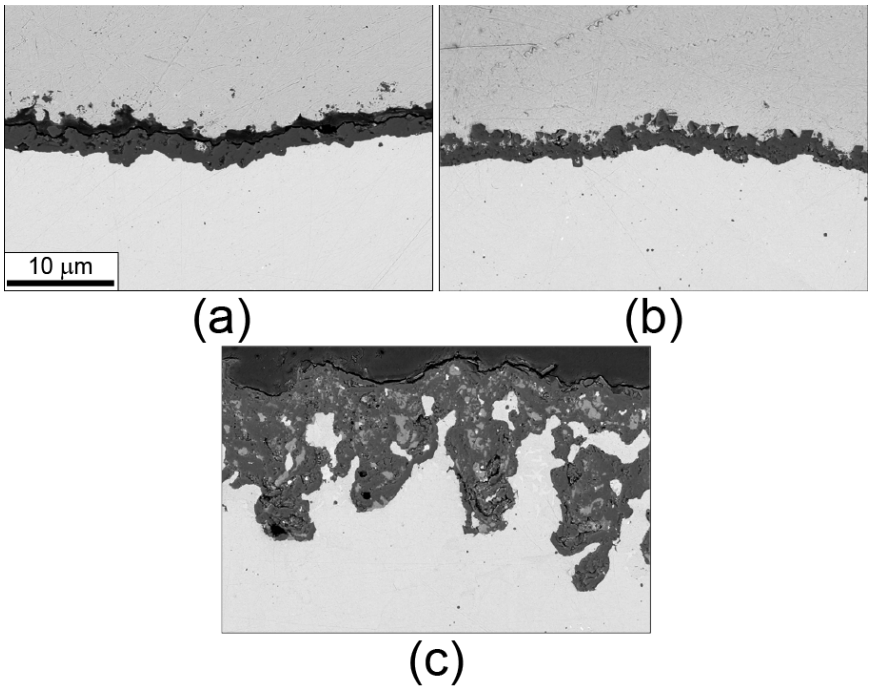


**Figure 3.11 Cross-sectional BSE images of the CMSX-4 NiAlPt coating scales showing the (a) typical F76 scale, (b) typical Blend scale, and (c) worst Blend scale.**

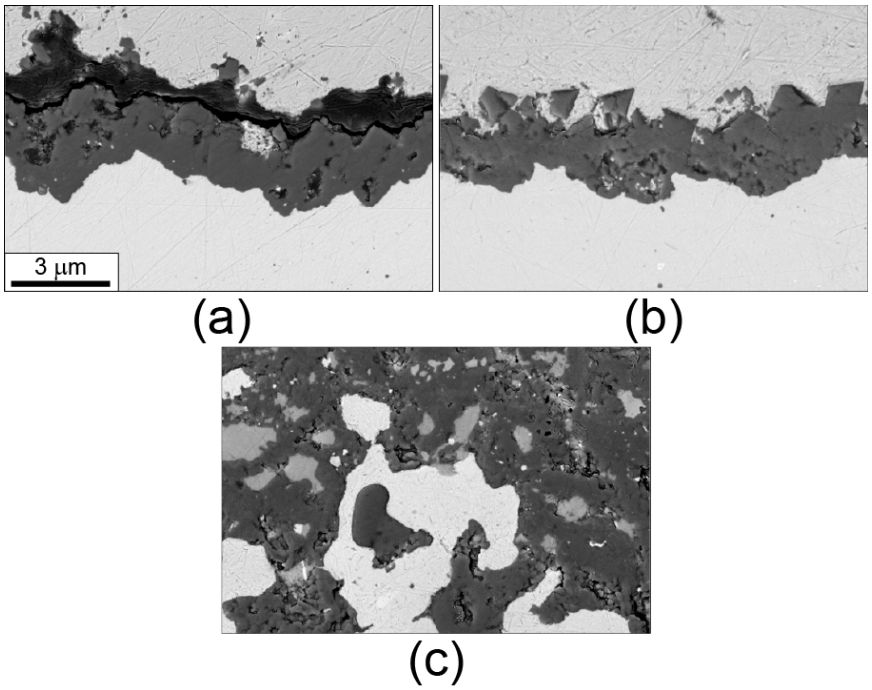


**Figure 3.12 Cross-sectional BSE images of the CMSX-4 NiAlPt coating scales showing the (a) typical F76 scale, (b) typical Blend scale, and (c) worst Blend scale.**

Figure 3.13 shows the EDX elemental maps and chemical composition of the scales formed for both tests of the Pt-modified NiAl coatings. The location of the Mg and Al overlap on the top of the scale indicating that a Mg, Al spinel has grown on top of the α-alumina below it for both tests. The quantitative EDX shows a composition with a similar stoichiometry to that of a spinel $AB_2O_4$, where $A$ is Mg and B is Al. The composition of the scale for the Blend test matches the spinel stoichiometry better than that of the F76 test. This is likely a result of the spinel grains being larger in the Blend test than in the F76 test and therefore having less overlap with the alumina in the EDX interaction volume. In areas of large attack on the Blend test, the Mg, Al spinel is also found on top of the porous alumina scale.

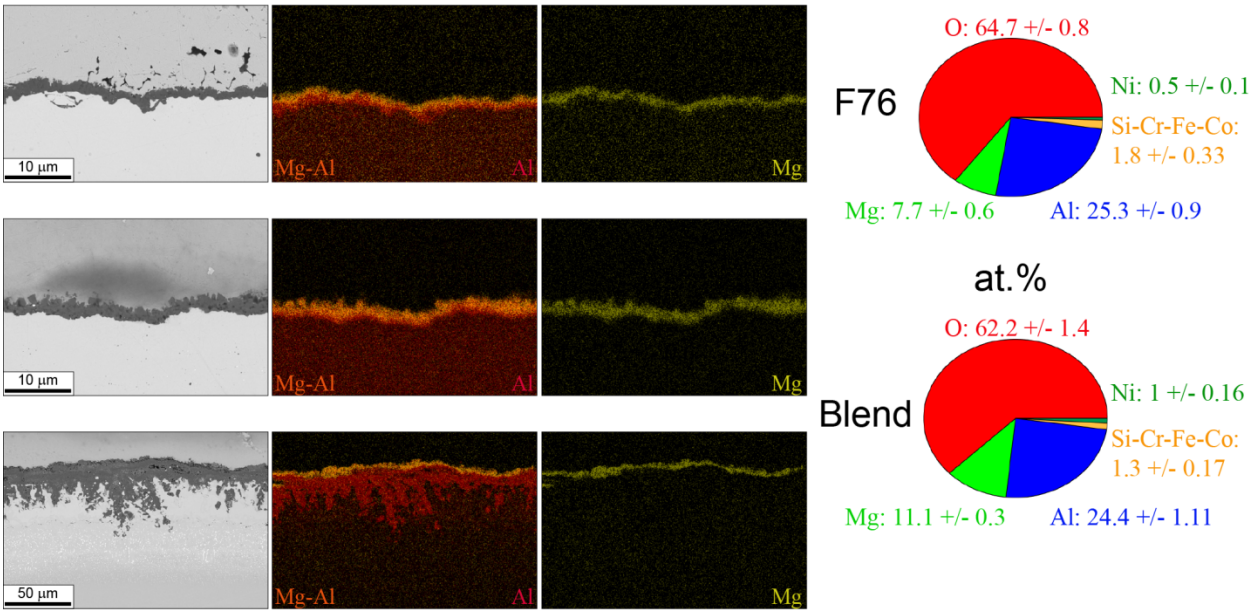


**Figure 3.13 BSE images, EDX maps, and quantitative EDX of the scales for the CMSX-4 NiAlPt coating material group.**

EDX line scans of the Pt-modified NiAl coating are shown in Figs. 3.14-17: Fig. 3.14 is the AR, Fig. 3.15 is the F76 exposed sample, Figs. 3.16 and 3.17 are the Blend exposed samples—the least and greatest attack cross-sections in this test, respectively. The compositions of the major components—Al, Ni, and Pt—are always shown on top of the minor components—

Co, Cr, Si, Ti, and W. The line scans start at the top of the coating, continue through the diffusion zone, and end 16 microns into the substrate—each region is color-coded in the Figs. In Fig. 3.14, there are large gradients for the major and minor components within the coating of the AR sample. Al and Pt have their greatest composition at the top of the coating and then decrease towards the diffusion zone while Ni follows the opposite trend. The minor components all increase in composition going towards the diffusion zone with the exception of W which is not detected until the substrate. Within the diffusion zone, there is much less change in composition for all the elements in comparison to the coating. The substrate is rich in Ni and devoid of Pt but Al is still present consistently at ~15 at.%. The minor components all increase in composition relevant to the coating and diffusion zone with the exception of Si and Ti.

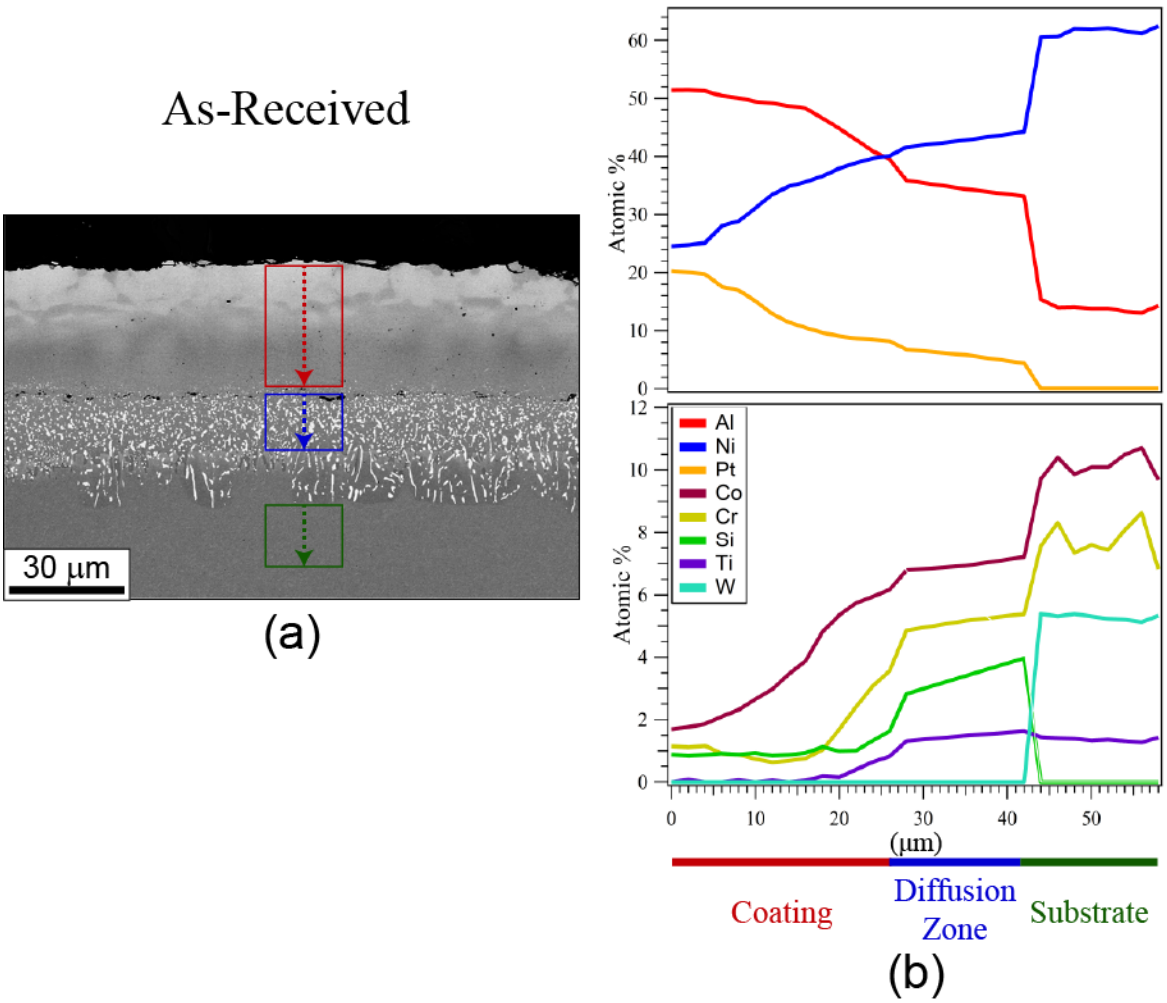


**Figure 3.14 EDX line scan of the as-received CMSX-4 NiAlPt coatings showing the (a) corresponding BSE image and (b) elemental profiles for the coating, diffusion zone, and substrate.**

The EDX line scan for the F76 exposed sample is shown in Fig. 3.15. There are significantly less compositional gradients for all elements of the F76 exposed coating as compared with the AR sample. The minor components have diffused further up the coating while Ni has been enriched in the coating at the expensed of Al and Pt depletion. As in the AR sample, there is marginal compositional change in the diffusion zone of the F76 exposed sample for all components. The compositions of all elements within the substrate are the same as they were in the AR sample.

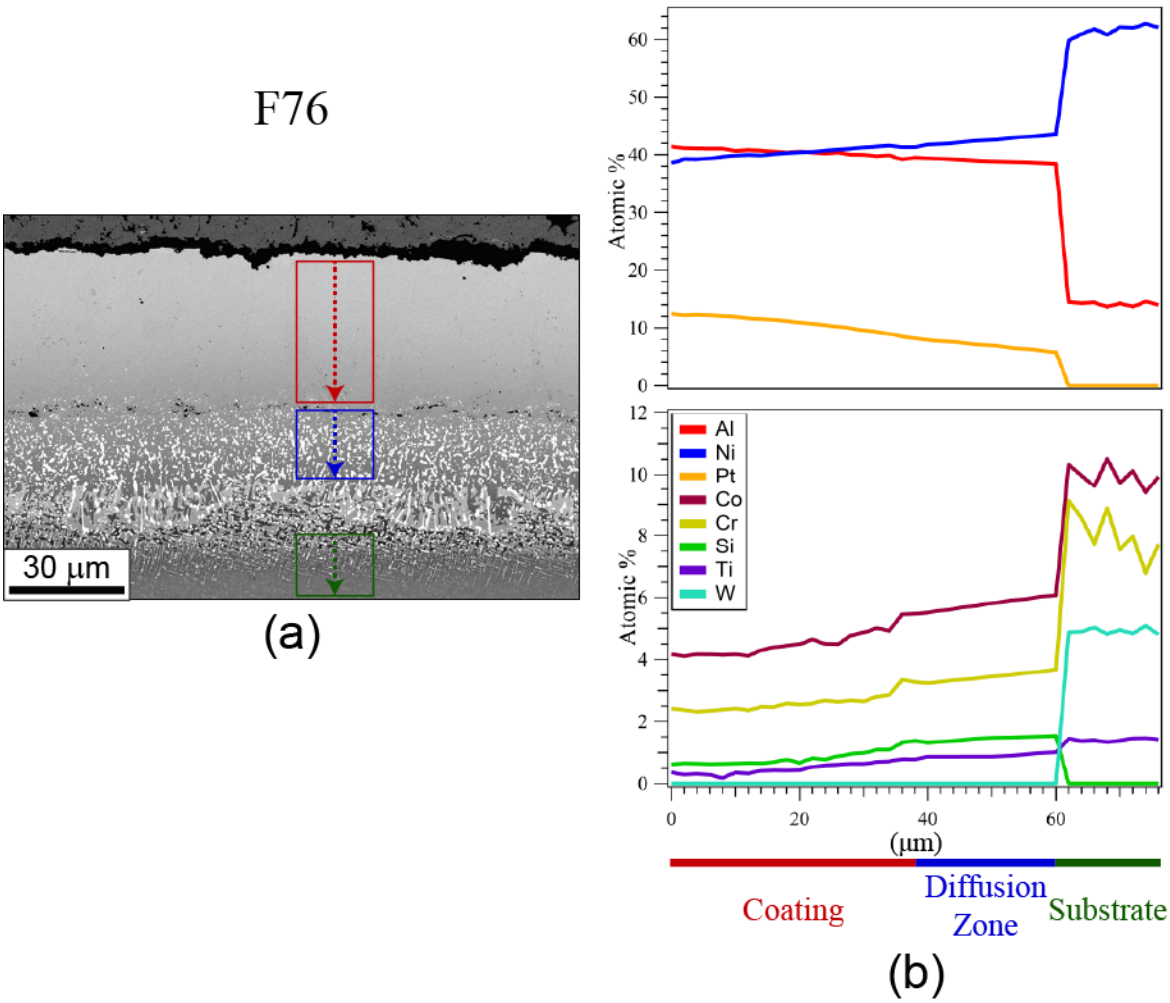


**Figure 3.15 EDX line scan of the F76 exposed CMSX-4 NiAlPt coatings showing the (a) corresponding BSE image and (b) elemental profiles for the coating, diffusion zone, and substrate.**

The EDX line scan for the Blend exposed sample with the least attack is shown in Fig. 3.16. There is even less of a compositional gradient for all elements in the coatings of the Blend: Least Attack sample as there was for the F76 exposed coating. There is slightly less Al and Pt in the Blend: Least Attack coating as there was for the F76 coating which is compensated with slightly more Ni. There is little change in composition between the coating and diffusion zone for all elements. The composition of the substrate is the same as it was for the AR and F76 exposed sample.

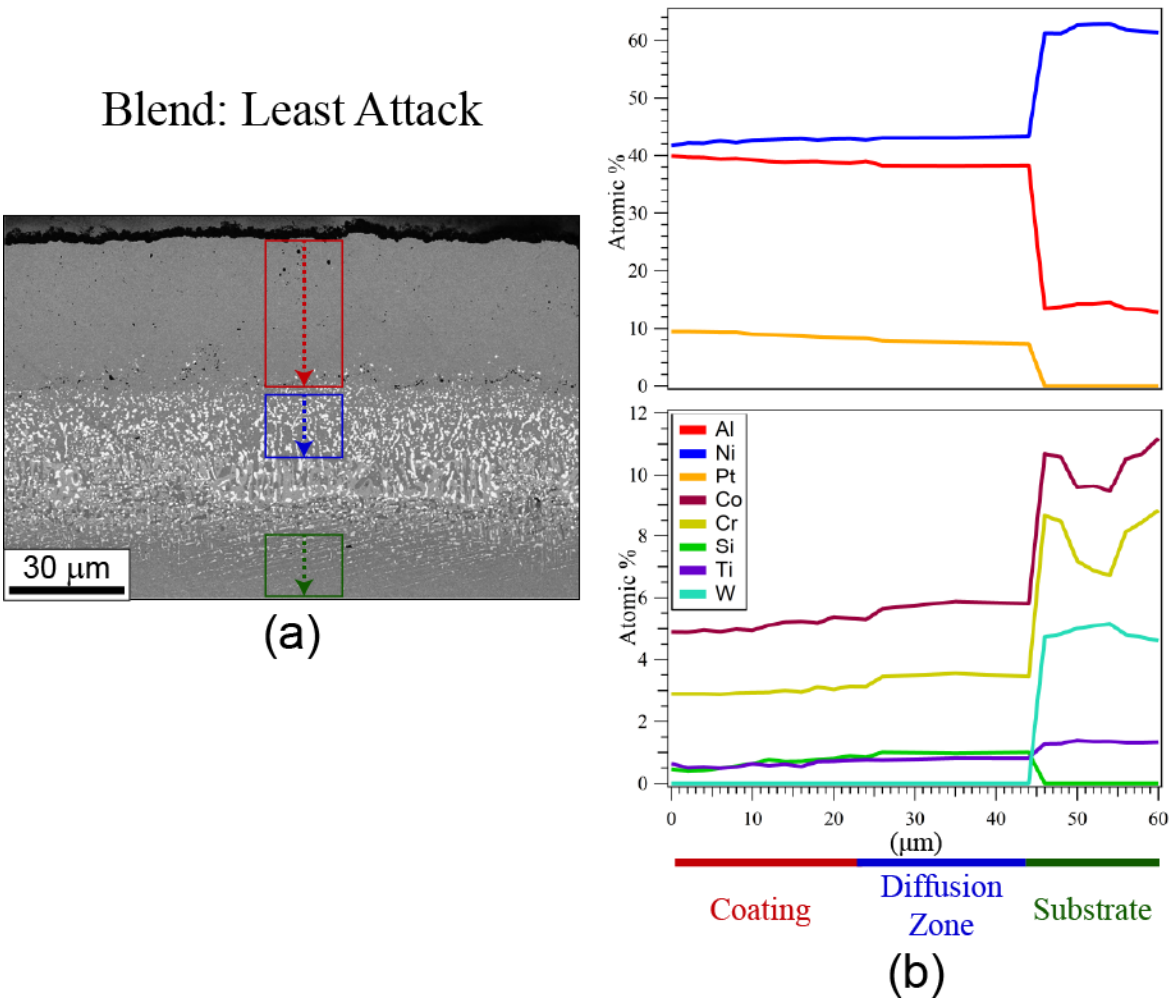


**Figure 3.16 EDX line scan of the Blend: Least Attack exposed CMSX-4 NiAlPt sample showing the (a) corresponding BSE image and (b) elemental profiles for the coating, diffusion zone, and substrate.**

The EDX line scan for the Blend exposed sample with the greatest attack is shown in Fig. 3.17. The composition profiles within the coating of the Blend: Greatest Attack vary significantly more than the other exposed samples. After four microns into the residual coating, there is a sharp gradient in the Al and Ni compositions with Al decreasing and Ni increasing. After these abrupt changes, there are only slight differences in the composition of the major components through the diffusion zone. The minor components show abrupt changes in composition as well after four microns. The most significant change in the composition of the

minor components from the other exposed samples is the increase of Si present in the coating and diffusion zone that continues to increase as it approaches the substrate. The compositions of the other minor components do not change significantly in the diffusion zone and there are only slight increases of Ni in the diffusion zone at the expense of Al and Pt as the profile approaches the substrate. As with the other exposed samples there is little change in the composition of the substrate from the AR sample.

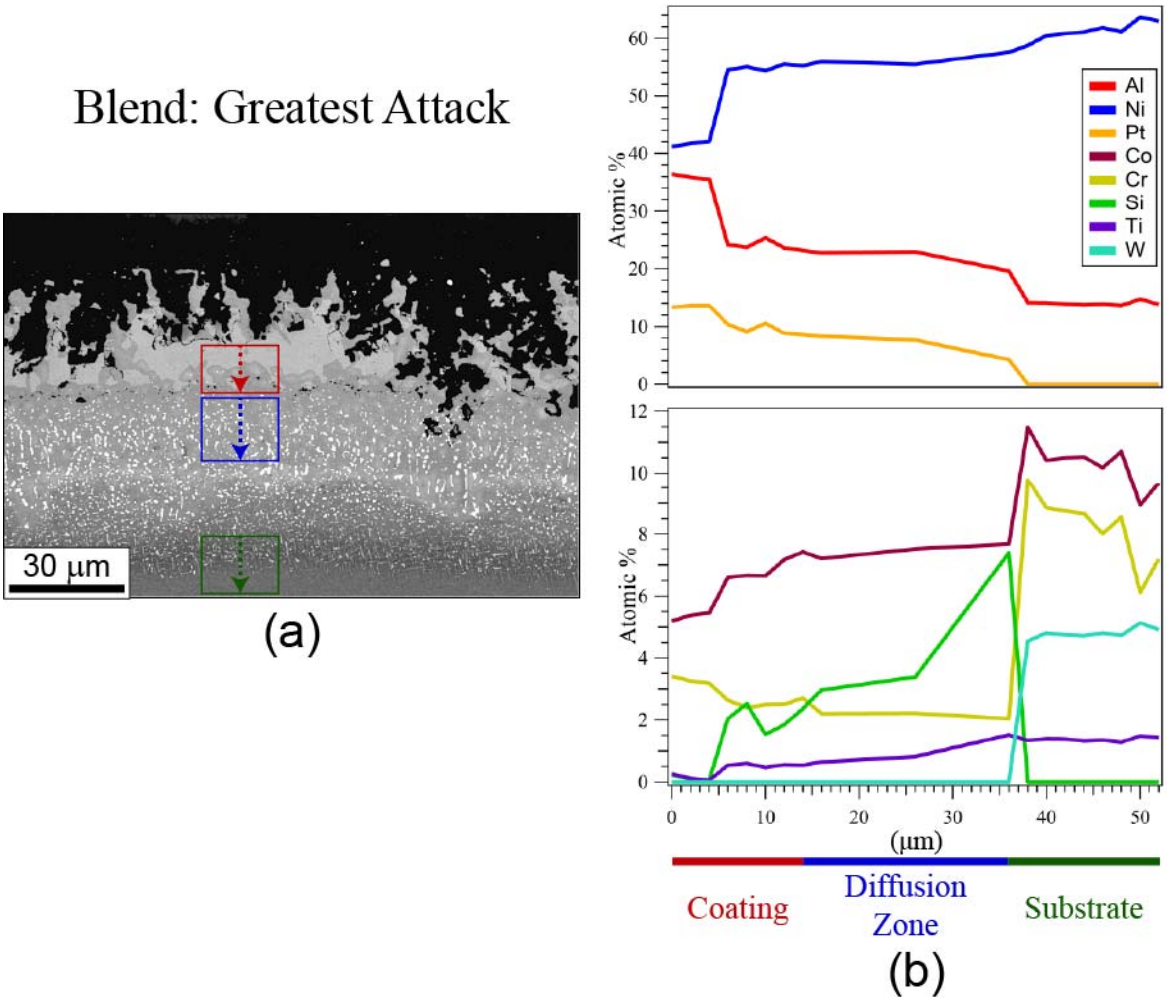


**Figure 3.17 EDX line scan of the Blend: Greatest Attack exposed CMSX-4 NiAlPt sample showing the (a) corresponding BSE image and (b) elemental profiles for the coating, diffusion zone, and substrate.**

### 3.3.4 CoCrAlHf Coatings on a Mar-M-509 Substrate

The morphology of the CoCrAlHf coatings of the AR, Blend, and F76 exposed samples are shown in Fig. 3.18. At a HFW of 250μm, the morphology of the coatings from either test does not appear that different from the AR condition. The surface roughness for the exposed samples does not change from that of the AR condition. Thin, compact oxides form on the exposed samples of both tests with no indication of destructive "breakaway oxidation." This is consistent with a previous investigation in a modified dean's rig where it was found that CoCrAlHf coatings with more than 20 wt. % Cr (the AR coating has excess of 27 wt% Cr) were not attacked after 20 days of cyclic exposure to Type I hot corrosion conditions.

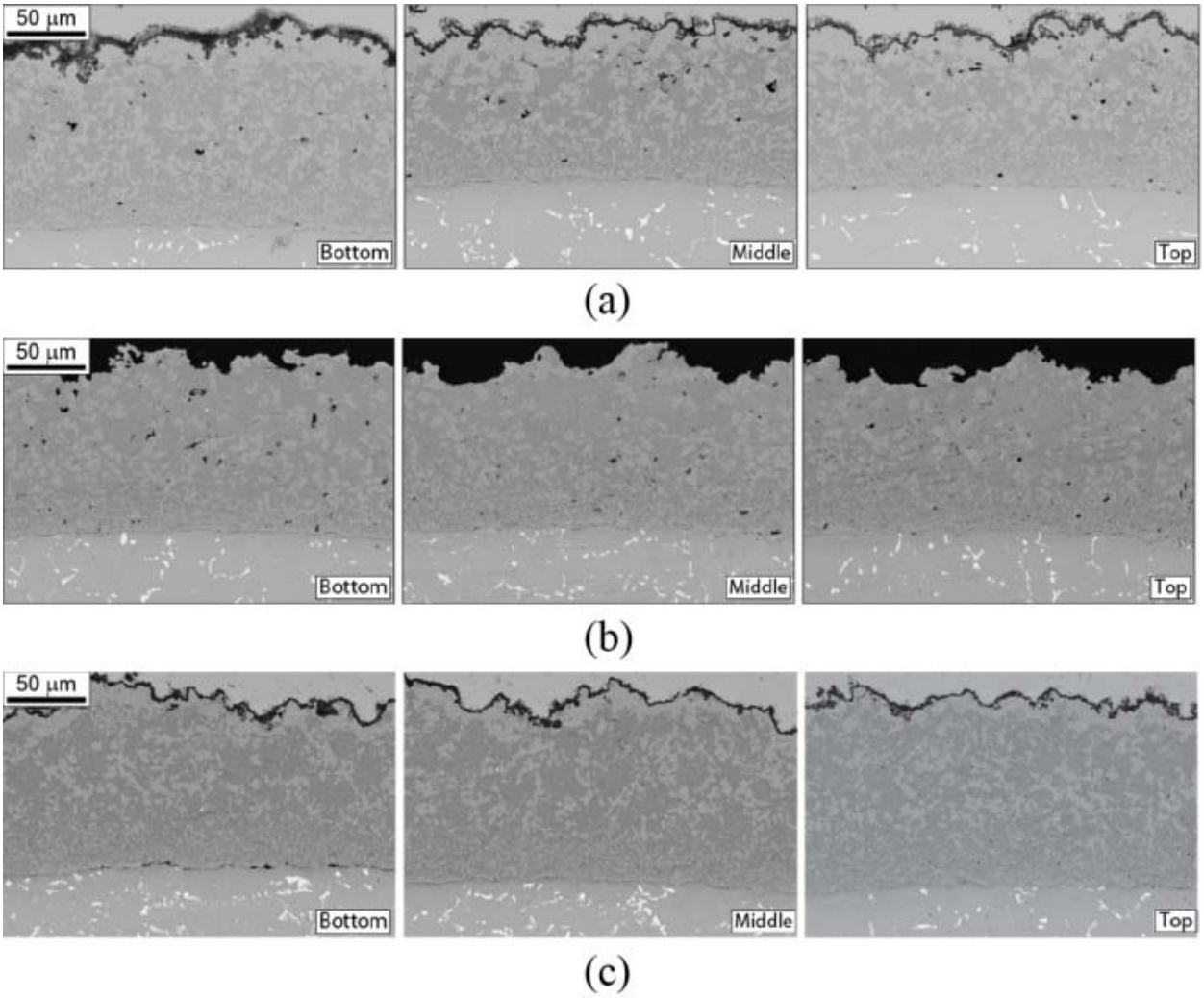


**Figure 3.18 BSE imaging comparison of the CoCrAlHf coatings for different cross-sections along the pin length showing: (a) the Blend test, (b) the AR, and (c) the F76 test.**

One difference between the exposed CoCrAlHf samples and the AR is the coalescence of γ-Co at the top of the coating. This phase is preferentially located immediately below the scale but does not appear preferentially at this location in the AR coating. The γ-Co layers at the top of the exposed coatings form due to depletion of Al from the β phase. Figure 3.19 shows higher magnification images of the tops of the CoCrAlHf coatings. The contrast is increased in these images to better image the atomic number contrast in the coating but the scale is not observed as a result. The preferential location of the γ-Co phase is more apparent in the exposed samples,

although the concentration of this phase at the top of the coating does not seem consistent between the two tests. The Blend test has a more developed layer of the γ-Co phase than the F76 test, which appears less uniform.

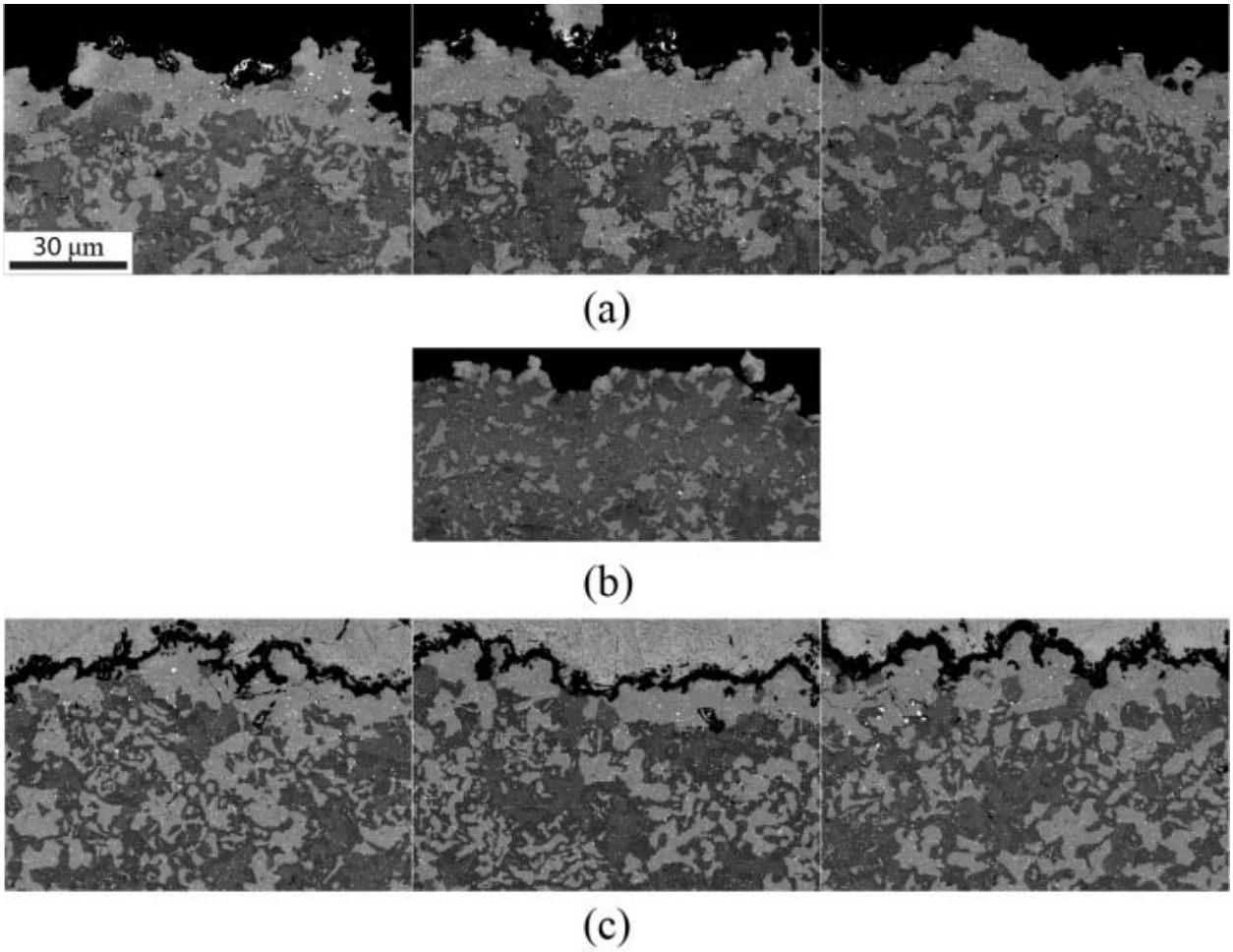


**Figure 3.19 BSE imaging comparison of the CoCrAlHf coatings showing the top of the coatings for the: (a) the Blend test, (b) the AR, and (c) the F76 test.**

### 3.3.5 Pt-modified NiAl Coatings on a Mar-M-247 Substrate

BSE images of the Mar-M-247 NiAlPt coatings are shown in Fig. 3.20 at a 250 µm HFW. The morphology of these coatings for both fuel tests shows much more corrosive attack as compared to the CoCrAlHf as expected. Alumina scales are still the predominant external scale formed on these coatings with dilute amounts of Cr in solid solution. However, in contrast to the

CoCrAlHf coatings, the characteristic Type I hot corrosion sulfides are now present beneath the alumina scale. There is not a substantial difference in the chemistry of the CrS formed beneath the scale for the two different fuel types.

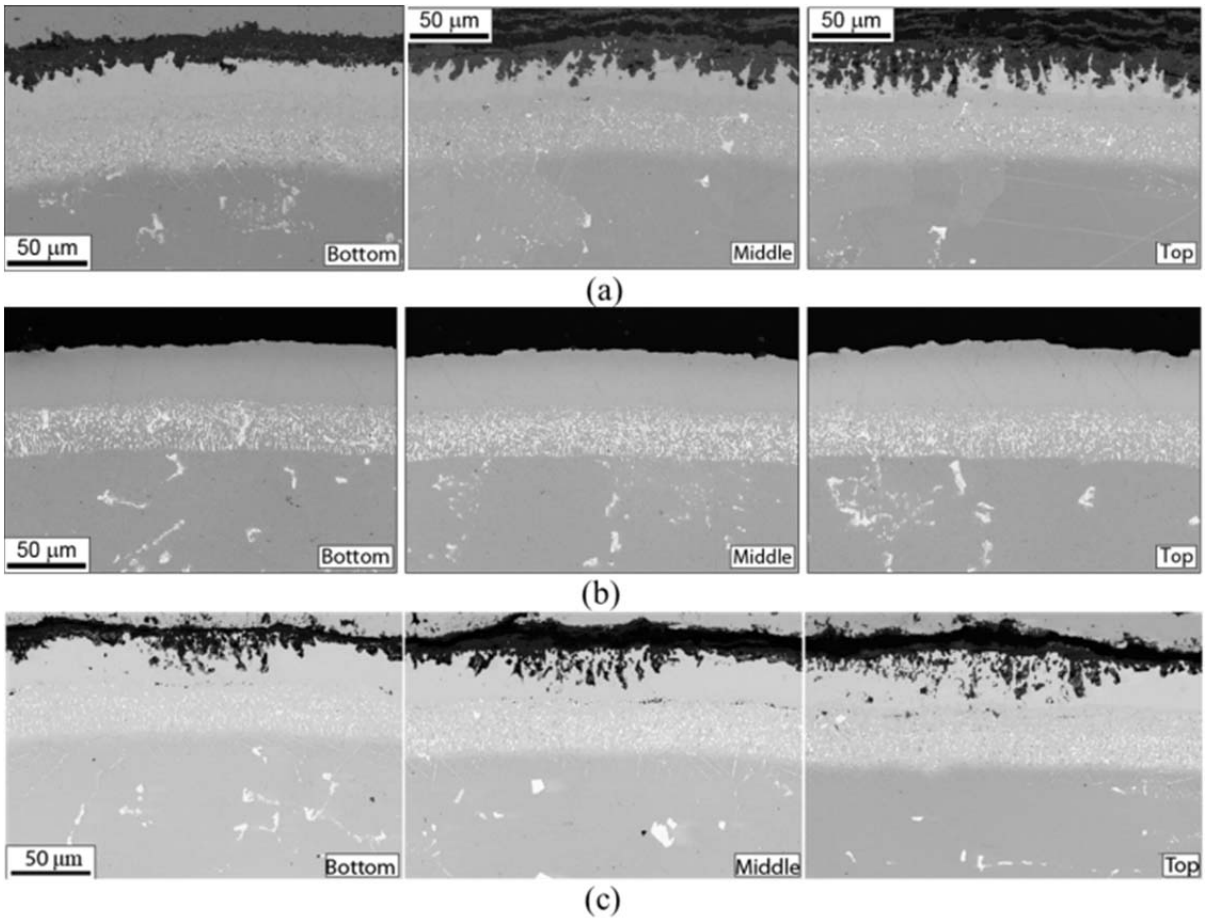


**Figure 3.20 BSE images of the Mar-M-247 NiAlPt coatings for the: (a) the Blend fuel, (b) the as-received condition, and (c) the F-76 fuel.**

Differences are seen between the Blend and F76 coatings in terms of the amount of the β and γ' phases that are now present in the Mar-M-247 NiAlPt coatings after exposure. Figure 3.21 compares a series of BSE micrographs from the Blend and F76 exposed samples as well as the AR sample. The β phase makes up a much larger fraction of the Blend coatings than that of the F76 coatings.

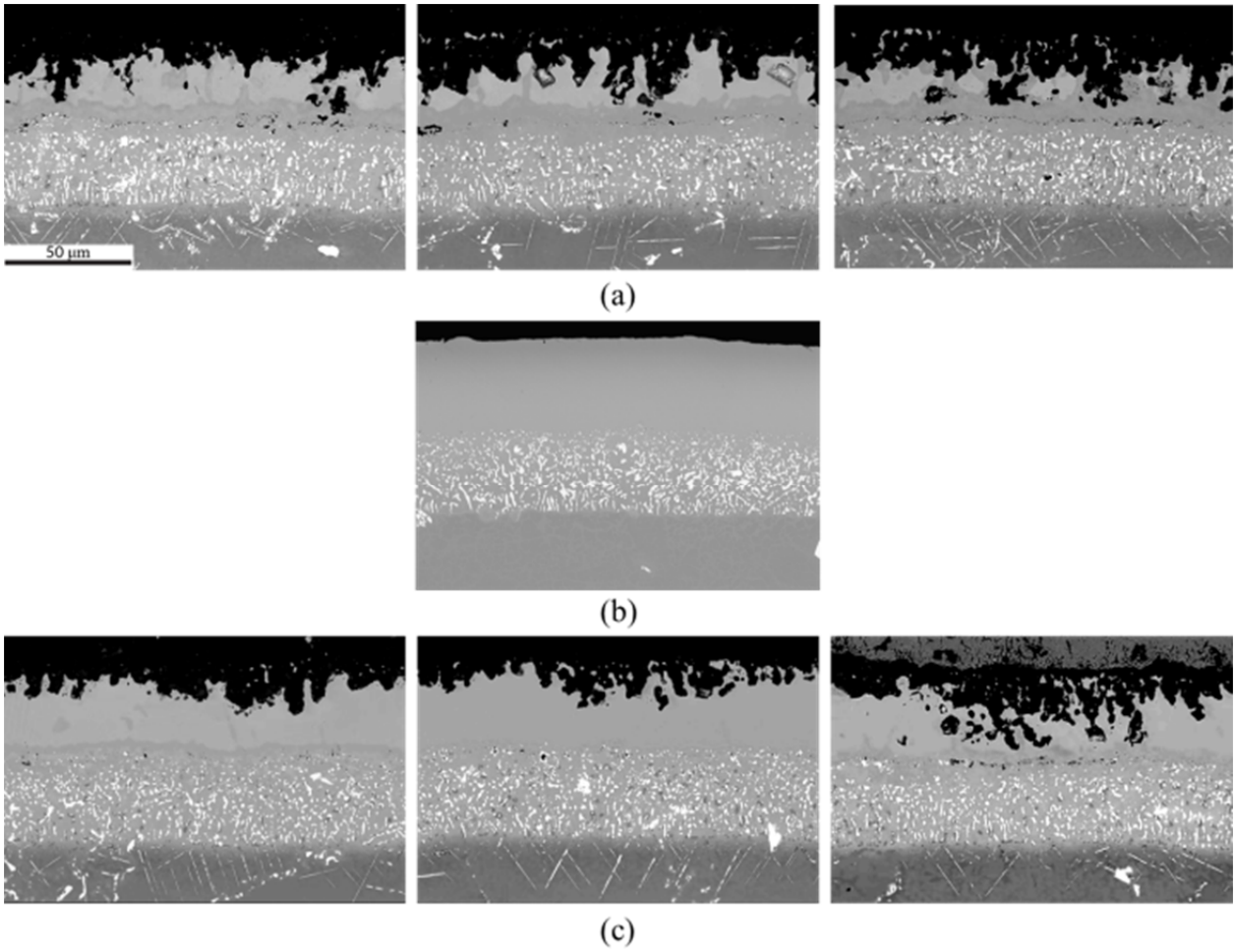


**Figure 3.21 BSE images comparing the phase distribution of the Mar-M-247 NiAlPt coatings for the: (a) Blend fuel, (b) as-received condition, and (c) F76 test.**

### 3.4 Discussion

The enhanced depletion observed in the NiAl and Pt-modified NiAl coatings can be explained by the Blend test creating a more basic environment at the scale/deposit interface. The $Na_2SO_4$ deposit on top of the α-alumina oxide will change its composition as a result of the environment and the underlying scale/coating. This is occurring during the initiation stage of hot corrosion where there is a transfer of electrons from the metallic atoms in the alloy to the reducible species in the deposit—the reducible species being oxygen [58]. The oxygen comes from both the gas stream and the $Na_2SO_4$ deposit in contact with the alloy. During this stage,

oxygen also reacts with the reservoir element in the alloy—aluminum in the coatings tested—to form the corresponding equilibrium scale α-alumina. The change in the deposit composition plays an important role in the destruction of the protective scale and therefore the hot corrosion attack. Goebel and Pettit described the influence of the composition of the $Na_2SO_4$ deposit by Eq. 3.1 [30].

$$Na_2SO_4 = SO_3 + Na_2O \qquad \text{[Eq. 3.1]}$$

The composition of the $Na_2SO_4$ deposit at a fixed temperature is then given by both (a) the oxygen partial pressure and (b) either the activity of the $Na_2O$ in the melt or the partial pressure of $SO_3$ ($p_{SO_3}$). If the law of mass action is applied to Eq. 3.1 and if the condensed phase, $Na_2SO_4$, is taken to be unity, the equilibrium constant for Eq. 3.1 can then be calculated by Eq. 3.2.

$$K_{eq} = a_{Na_2O} \cdot p_{SO_3} \qquad \text{[Eq. 3.2]}$$

Therefore according to Eq. 3.2, if either the $a_{Na_2O}$ or the $p_{SO_3}$ is increased the equilibrium constant for the Eq. 3.1 reaction will be larger. A larger equilibrium constant will decompose the $Na_2SO_4$ deposit faster. The Blend test conditions are proposed to cause a higher $a_{Na_2O}$ at the scale/deposit interface than the F76 test such that the alumina scale is dissolved faster and therefore requires Al to de depleted faster from the alloy which is shown by EDS line profiles.

The $a_{Na_2O}$ will play a more dominate role in the dissolution of the scale as opposed to the $p_{SO_3}$ in the LVBR testing performed here because the conditions favor basic fluxing. This can be understood in terms of how the protective scale is destroyed and how the hot corrosion attack moves toward the propagation stage [58]. Sulfidation and/or fluxing of the alloy scale are

possible routes for the propagation stage. As the temperature is above 850 °C and the $p_{SO_3}$ is below $10^{-4}$ atm, scale fluxing is proposed to be the initial dominant means of hot corrosion propagation. Moreover, basic fluxing is expected to be the means of scale fluxing given the minimal amount of the acidic component— $SO_3$ —or its sulfide reaction products in the alloy. Jose et al. formulated acidic and basic reactions to describe the dissolution of α-alumina [47]. The *basic* dissolution of alumina can be described by Eq. 3.3.

$$Al_2O_3 + O^{2-} = 2AlO_2^- \qquad \text{[Eq. 3.3]}$$

At equilibrium and in basic conditions, $Al_2O_3$ will be dissolved by $Na_2O$ according to Eq. 3.4.

$$Na_2O + Al_2O_3 = 2NaAlO_2 \qquad \text{[Eq. 3.4]}$$

To understand better how an increase in basicity can affect the stability of the scale, it is informative to analyze a phase stability diagram of the system. Jose et al. constructed a Na-Al-S-O phase stability diagram at 927° C as shown in Fig. 3.22 [47]. The dashed lines indicate where $Na_2SO_4$, $Na_2O$, and $Na_2S$ are stable in the phase stability diagram. $Na_2SO_4$ is clearly stable over a wide range of basicity and $p_{SO_3}$. All LVBR samples form α-alumina scales during both the Blend and F76 tests. If basic fluxing is occurring, the exposed samples should be moving from the α-alumina phase field *toward* the $NaAlO_2$ phase field as shown schematically in Fig. 3.22. However, as there is no evidence for the formation of $NaAlO_2$ in the exposed alloy coating, this indicates that the LVBR test conditions are within the α-alumina phase field and therefor have –log $a_{Na_2O}$ values between 9 and 19.

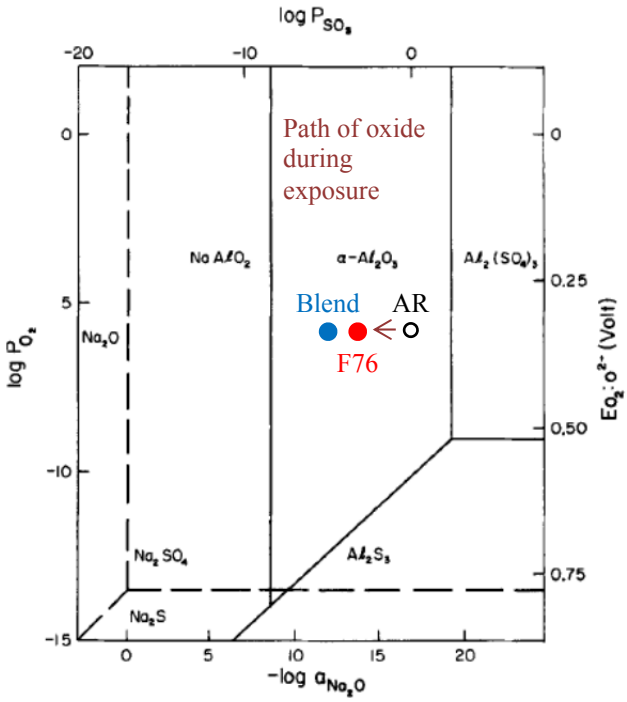


**Figure 3.22 A Na-Al-S-O phase stability diagram at 927° C with the positions of the as-received and exposed samples superimposed [44].**

In order to explain why an increase in the basicity will dissolve an α-alumina scale faster, it is illustrative to examine the solubility curve in an idealized system. The solubility curve of an α-alumina scale in a $Na_2SO_4$ bath at 927° C and $p_{O_2}$ = 1 atm is shown in Fig. 3.23 as a function of basicity. Superimposed on Fig. 3.23 are the proposed locations of the Blend and F76 tests. As the Blend test causes a higher basicity at the scale/deposit interface than the F76, it falls higher up on the solubility curve and results in a higher solubility of α-alumina in the $Na_2SO_4$ melt. Conversely, the F76 test falls lower on the solubility curve due to a lower basicity and results in a lower solubility of α-alumina in the $Na_2SO_4$ melt. An increased basicity at the scale/deposit interface for the Blend test and therefore an enhanced scale fluxing rate would explain why there is an enhanced depletion of Al in the Blend test exposed samples.

Although the solubility curve in Fig. 3.23 is for a fixed partial pressure, the authors stated that it should not depend upon the $p_{O_2}$ as the acidic or basic dissolution of alumina does not involve a change in aluminum valence [47]. If this is true, then the basic fluxing of an alumina scale in Type I hot corrosion conditions should not be dependent upon the $p_{O_2}$. However, it should be noted that the experiment used in the study was not performed in a $SO_3/O_2$ gas mixture. Therefore, the $SO_3$ in the experiment is being supplied by the $Na_2SO_4$ deposit. This would not be the case for the LVBR experiments performed here, as there is a $p_{SO_3}$ present within the combustion stream. Therefore, the $p_{O_2}$ will likely have an impact on the basicity at the oxide/deposit interface as well.

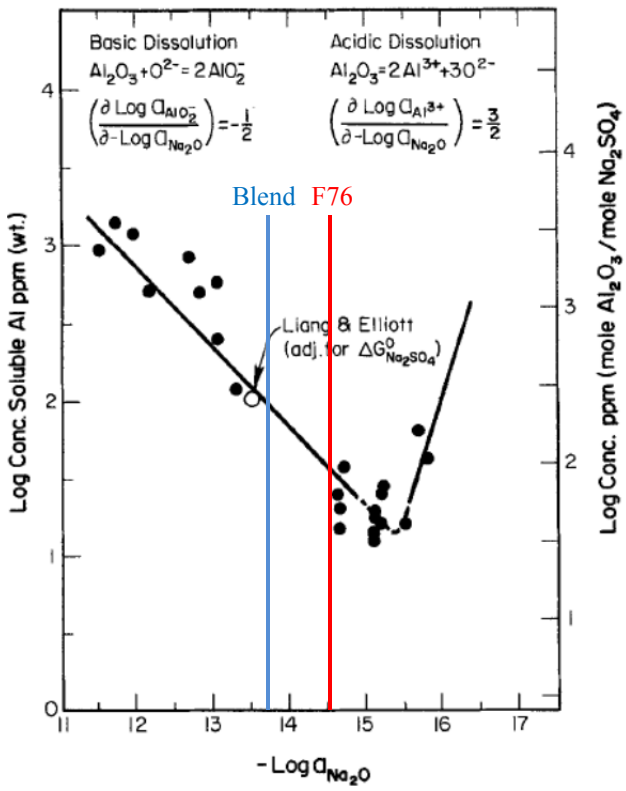


**Figure 3.23 Solubility curve of α-alumina in a fused $Na_2SO_4$ bath at 927° C and $PO_2$ = 1 atm [44].**

While it is beyond the scope of this work to explain why the combustion characteristics of the Blend test would promote a more basic environment, a connection can be made in regards to how the fuel properties can alter the reaction kinetics of the combustion process. A recent investigation into the physical properties of the Blend fuel has shown that the density and dynamic viscosity of the blend fuel are lower than that of the F76 fuel [5]. These physical property differences can affect the atomization characteristics of the fuel—or its ability to form droplets and vaporize. Generally speaking, increasing the density will enhance the atomization, while increasing the viscosity will reduce the atomization for a given fuel [59]. These opposite trends would seem to offset one another, but there is a 30% decrease in the viscosity and a 5% decrease in the density. Therefore, the decrease in the viscosity of the fuel would be expected to be more influential and cause the Blend fuel to have better atomization characteristics than that of the F76. This would imply a smaller droplet size of the Blend fuel, which would allow the fuel to evaporate more quickly than the F76 test. The faster evaporation rate of the Blend test would have implications related to the kinetics of the reaction species during combustion. For example, the conversion of CO to $CO_2$ is a kinetically limited process, but if given more time with better atomization this would allow for more conversion of CO to $CO_2$ and a lower corresponding concentration of oxygen. This could then alter the $p_{O_2}$ or $p_{SO_3}$ and in turn, according to Eq. 3.2, alter the basicity of the deposit. However, a more detailed analysis of the atomization characteristics of the fuels would be needed to better connect the increased basicity to the fuel properties.

### 3.5 Conclusion

Burner rig testing was performed on metallic overlays in Type I hot corrosion conditions to determine the effect of the fuel combustion environment on the hot corrosion material

response of the coatings. Larger average surface loss and oxide/sulfide penetration into the samples were observed for the Blend test as compared to that of the F76 test. While the microstructure for the majority of the coatings looks similar between tests, the NiAl and Pt-modified NiAl coatings have regions with thick porous oxides and deep sulfide/oxide penetrations for the Blend test. Furthermore, EDS analysis reveals that these regions of high attack have significant depletion of the reservoir element as compared to those of low attack. To explain this, it is proposed that the Blend fuel promotes a more basic fluxing condition at the scale/deposit interface in Type I conditions than that of the F76 fuel. If the basicity at the scale is greater in the Blend test environment, the protective scale will dissolve faster than that of the F76 test environment requiring more of the reservoir element to heal the dissolved scale. These results indicate that the NiAl and Pt-modified NiAl coatings will not have the same predicted lifetime when used in a Blend fuel environment and either should not be used in these environments or need to be further modified to accommodate the more basic conditions.

# 4 Chapter 4: Accelerated Aging of Yttria-Stabilized Zirconia Thermal Barrier Coatings in High Water Vapor Content, Elevated Temperature Environments: X-Ray Diffraction and Raman Spectroscopy Measurements


## ABSTRACT

High temperature aging was performed on free-standing, air-plasma spray (APS), 8 wt% yttria-stabilized zirconia (8YSZ) coatings in both dry and high water-vapor content environments. Aging was carried out isothermally at 1330°C at time intervals determined by a normalizing, non-dimensional Larson–Miller parameter (LMP). The phase evolution of the metastable, tetragonal phase of 8YSZ—designated as *t'*—to the thermodynamically stable tetragonal, cubic, and monoclinic phases in the different exposure environments is characterized by X-ray diffraction (XRD) and Raman spectroscopy. Identification of the phases post-aging by both characterization techniques showed little difference between exposure environments up to aging times of 88 h (LMP = 15.2K). However, at 140 h (LMP = 15.9K) and afterwards there is a distinct increase in the amount of the monoclinic phase formed in the humid environment relative to that of the dry environment as measured by both characterization techniques. The trend of increased monoclinic phase formation for the humid-aging exposure continues for two subsequent aging times. A proton incorporation mechanism is invoked to explain the increased destabilization of 8YSZ in high-temperature, humid-aging environments. The result of enhanced degradation of APS 8YSZ in high temperature, humid environments may have implications for power generation turbines that use high-hydrogen content fuels.


## 4.1 Introduction

The advent of Integrated Gasification Combined Cycle (IGCC) power plants promises to improve the efficiency and fuel diversity of gas turbine engines. The IGCC plants can take a variety of fuel sources—coal, biomass, and renewable fuels—and convert them into a synthetic gas (syngas) that can be used to generate electric power at an efficiency of 45% with full carbon

capture. However, the use of syngas may bring additional material challenges on the thermal barrier coating (TBC) system used to protect the hot section blades [10]. These challenges arise from the associated higher water vapor content in the combustion zone as a result of burning a high-hydrogen content fuel such as syngas. According to a report by the National Energy Technology Laboratory (U.S. Department of Energy), the use of steam injection to suppress $NO_x$ emissions from gas turbines may increase the water content in the turbine exhaust to 25-30% – a fourfold increase over the conventional combustion of natural gas [3]. Therefore, it is important to understand the role of high water vapor content in the material degradation of TBC systems in the combustion environment of gas turbines.

The degradation of the ceramic coating commonly used as TBCs – 8wt% yttria stabilized zirconia (8YSZ) – has recetly received increased attention as IGCC turbine inlet temperatures continue to rise, e.g. 1425 °C or higher [3]. One major degradation mechanism is the tetragonal phase of 8YSZ – referred to as *t'* – decomposing to its equilibrium mixture of yttrium-rich cubic phase and yttrium-lean tetragonal phase given a sufficient thermodynamic driving force, as shown schematically in Fig. 4.1. The metastable *t'* phase has been shown to transform to these more stable phases – as well as the continued transformation of the tetragonal phase to the monoclinic phase below the martensitic temperature – upon aging in laboratory-air environments at temperatures in excess of 982ºC [60-63]. The resulting stable phases form a coherent array of Y-rich (cubic + *t''*) and Y-lean (t + m) phases at the expense of the *t'* phase. In a recent study by Krogstad, *et al.* [36], the inferred gradient in the degree of tetragonality across these coherent interfaces was used as evidence for a spinodal decomposition as opposed to a nucleation-and-growth mechanism. This destabilization of the *t'* phase has been found to occur in 8YSZ for both electron beam physical vapor deposition (EBPVD) coatings used in aero-propulsion

turbines and APS coatings predominately used in power generation systems [60, 61]. While both EBPVD and APS coatings have been shown to follow the same trend in destabilization of the *t'*-phase with aging, a direct comparison of these two coatings showed distinct differences in the phase evolution of the stable Y-rich and Y-lean phases after the initial destabilization of the *t'* phase [60].

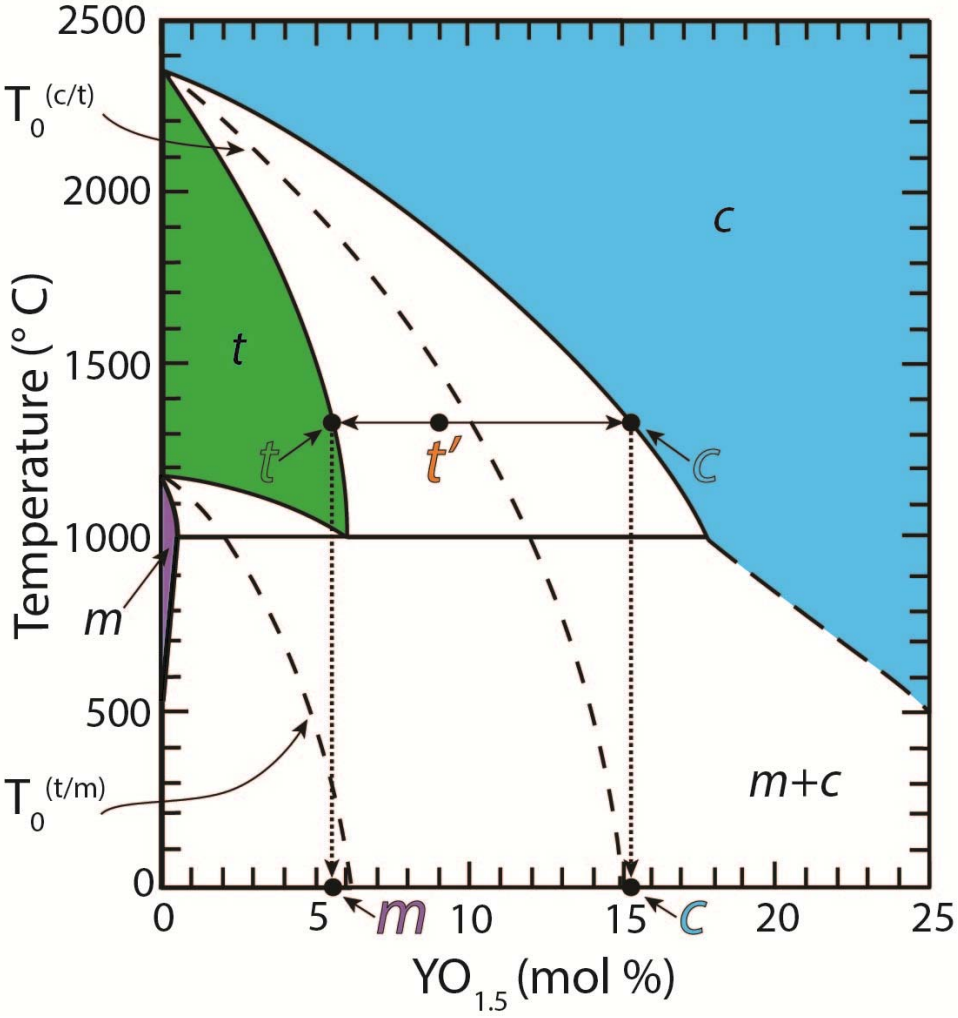


**Figure 4.1 The $YO_{1.5}$–$ZrO_2$ phase diagram redrawn from Lipkin et al. [37], showing the decomposition of the *t'* phase during isothermal aging at 1330°C. The metastable *t'* phase will decompose to the equilibrium tetragonal and cubic phases with increased aging times.**

While previous studies of the destabilization of the *t'* phase at elevated temperatures have generally focused on dry or laboratory-air environments, the low-temperature degradation (LTD) of YSZ has focused on the destabilization of the tetragonal phase in humid environments. In

LTD, the tetragonal phase of the YSZ (t-YSZ) transforms to the monoclinic phase at temperatures less than 300ºC in moist air. LTD in humid environments was first identified by Kobayashi *et al.*[64] who reported on the presence of micro-cracking and the loss in strength after the tetragonal to monoclinic transformation in YSZ. Since this early finding, additional papers have identified some general characteristics of LTD which include: (a) the phase transformation originating from the surface, and (b) resistance to the phase transformation increasing with higher stabilizer content or smaller grain sizes [65-67]. Many mechanisms have been proposed for trying to understand the monoclinic to tetragonal phase transformation that occurs during LTD in humid environments. Yoshimura *et al.* [68] proposed that water cleaves Zr-O-Zr bonds at the surface of t-YSZ causing the formation of Zr-OH or Y-OH. The formation of these hydroxyl groups was said to cause a stress field that induced the monoclinic phase transformation. Along the same lines, Sato and Shimada [66] proposed that the chemisorption of water on the surface of t-YSZ formed Zr-OH, which in turn caused the surface energy difference to be reduced between the tetragonal and monoclinic grains. However, this model is limited in that it does not explain the dependence of the tetragonal-to-monoclinic transformation on the grain size and stabilizer content [69].

In a different proposed LTD model, Lange *et al.* [67] suggested that α-$Y(OH)_3$ formation created yttria-poor regions at the surface, which then serve as nucleation sites for the monoclinic phase. This explanation was largely debunked by Kim *et al.* [69], in a study where 3 mol% YSZ samples were aged by LTD, annealed for two hours, and then aged by LTD again. The authors found that the YSZ transformed to the monoclinic phase after the initial aging, reversed to the tetragonal phase by the annealing treatment, and then transformed back to the monoclinic phase again after aging – but with significantly less transformation than after the first aging treatment. If $Y_2O_3$ was being depleted from the sample by hydroxide formation during the initial aging treatment, then subsequent aging should have caused further LTD due to less stabilizer content – However, this did not occur. These authors also doped t-YSZ with $Nb_2O_5$ and showed the activation enthalpy for LTD was constant regardless of the dopant amount and grain size. The authors suggested that LTD was a cause of thermally-activated oxygen vacancy diffusion where the pentavalent dopant annihilated oxygen vacancies, and thus decreased the oxygen diffusion

rate – and therefore the rate of LTD. This explanation is consistent with the annealing anion vacancy model of LTD [70, 71]. According to this model, water dissociates at the surface of t-YSZ to produce interstitial hydrogen ions and oxygen anions which anneal anion vacancies. Although this annealing anion vacancy model is appealing, it has not yet been proven that oxygen anions or some other water derived species is entering the 8YSZ and altering the thermodyamics and/or kinetics of the tetragonal phase transformation.

Even if oxygen anions are entering 8YSZ, this still leaves protons unaccounted for in their role in influencing the phase evolution of the *t'* phase. As protons derived from water would be more numerous, more mobile, and can occupy more locations in the lattice than the oxygen anions, they would seem to have a much more influential role than oxygen anions in destabilization pathways. While protons are not considered the dominant ion conductor in YSZ, computational studies have shown that the energy associated with proton migration in YSZ is comparable to other proton conductors like $BaZrO_3$ [72, 73]. At temperatures relevant to LTD, protons were found to diffuse into single crystal tetragonal as determined by a SIMS analysis [74]. A different study measured the electrical conductivity of 3 mol% YSZ thin films in dry and humid environments across a range of temperatures [75]. The porous films showed a dramatic increase in overall conductivity in the temperature rang of 120 to 400 °C for the humid environment which the authors attributed to proton conduction. While it was only speculated that this was due to the formation of hydroxyl groups at the surface of YSZ, a separate study verified the presence of hydroxyl groups in YSZ thin films by exposing them to a deuterium oxide ($D_2O$) gas environment [76]. XPS on the exposed samples confirmed that hydroxyl ions were present on the sample even after etching the sample with Ar in the XPS chamber. The study also confirmed proton migration by measuring an open circuit voltage in a hydrogen/air fuel cell that disallowed oxygen migration due to the presence of a palladium interlayer. Therefore, there is evidence for protons to be incorporated into YSZ and migrate through the material in humid environments.

Both LTD in humid environments and high temperature aging in dry environments of 8YSZ have been shown to de-stabilize the *t'* or tetragonal phase to the monoclinic and other stable phases. However, what has not been shown is whether the de-stabilization of the *t'* phase

is accelerated at high temperatures – relevant to gas turbines – for long exposures in high water vapor content environments. This study demonstrates that aging 8YSZ in a high-temperature, humid environment does indeed accelerate the de-stabilization of the *t'* phase in comparison to that of a dry environment exposure. Furthermore, the mechanism of proton incorporation by hydroxyl group formation will be invoked to explain how water vapor species emanating from exposure to high water vapor content environments enhances the destabilization of the *t'* phase. Clarifying the role of water vapor in the high temperature degradation of 8YSZ will allow for more detailed investigations into the role of water species in the phase evolution of the *t'* phase at temperatures relevant to gas turbine power generation.

## 4.2 Experimental Procedures

### 4.2.1 Processing of APS TBC Coatings

A free-standing plate of APS 8YSZ, with thickness ~ 3mm, was fabricated at the Forschungszentrum Jülich research center in Jülich, Germany. The resulting material had approximately ~17% porosity, representative of commercial applications of APS YSZ in power generation combustion systems. The APS 8YSZ was sectioned with a slow-speed diamond blade saw prior to aging experiments.

### 4.2.2 Aging Exposures

Isothermal aging was carried out at 1330º C in a sealed, environmentally controlled furnace. For all aging experiments, samples were placed on top of loose 3 mol% YSZ powder to prevent diffusion between the samples and the crucible. All aging experiments were conducted at a fixed ramp-rate of 4°C/min, and the aging times varied between 6-570 h as determined by approximate LMP intervals. As the temperature was fixed at 1330º C for all aging experiments, a change in the LMP corresponds to a change in the aging time. Each sample was aged for only one aging time and not re-used for additional aging (e.g. the 140 h aged sample was not reused to achieve an aging time of 224 h as illustrated in Fig. 4.2). The exposure environment consisted of

a gas mixture of ultra-high purity $N_2$ and $O_2$ that was flowed through the furnace tube at a rate of 80 mL/min. The flow rates for both gases were chosen so that the $P_{O_2}$ was fixed at 0.2 atm for both the dry and humid environments. Prior to ramping the furnace to the aging temperature of either the dry or humid environment, the tube furnace was purged of laboratory air for six residence times of gas flow. For the humid-aging environment, a second purge was carried out to replace the dry environment with the humid one for another six residence times of gas flow while the furnace was held at 150ºC. All humid-aging tests were performed at a water vapor content of 45 vol% by bubbling the $N_2/O_2$ gas mixture through a water bath at a controlled bath temperature. In one case, a humid exposure with the same water vapor content was performed in a reducing environment (10% Hydrogen-90% Argon) in order to better determine the influence of oxygen anions/hydroxyl groups on the destabilization of the *t'* phase. After each humid-aging test, the condensed water vapor from the tube furnace exhaust was weighed to ensure that the controlled environment had a water vapor content of 45 vol%.

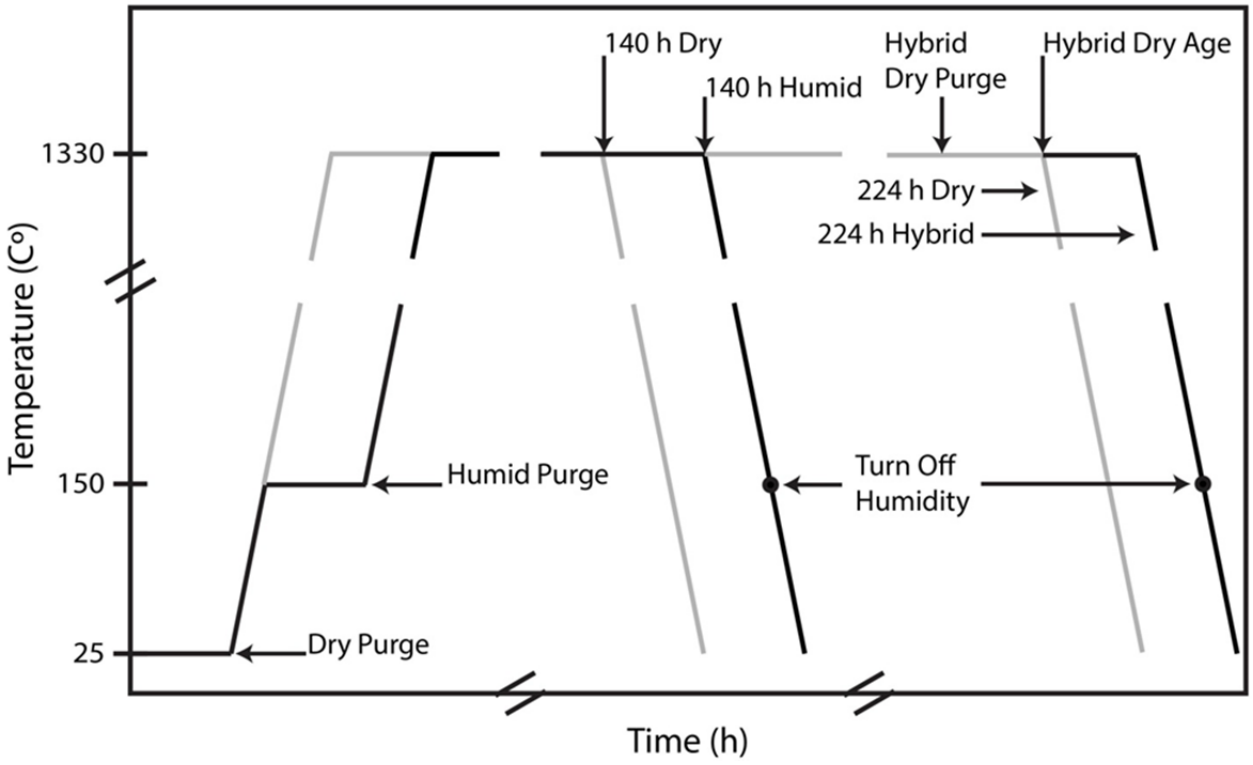


**Figure 4.2 Examples of the heating protocols for the sample aging showing the 140 h dry and humid tests, the 224 h dry test, and the hybrid 224 h test.**

### 4.2.3 Characterization of Phase Evolution – Experimental

Post-aging phase identification in the aged samples was achieved by XRD and Raman spectroscopy to determine if the *t'* phase of the 8YSZ was destabilized faster in a humid environment. XRD was performed using a step size of 0.004 deg with a scan speed of 1 deg/min on a 1D silicon-strip detector. In order to achieve a more-localized phase identification than XRD, Raman spectroscopy was performed. Prior to collecting spectra from aged samples, the instrument was calibrated using the 520.5 $cm^{-1}$ Raman band of a silicon wafer. Spectra were excited using a laser operating at a wavelength of 532 nm.

### 4.2.4 Characterization of Phase Evolution – Analysis

A Rietveld refinement analysis was performed on the XRD spectra using the *General Structure Analysis System* (GSAS) software with the EXPGUI graphical user interface [77] in

order to quantify the phase fractions of the YSZ after exposure to the different environments. The refinement employed a four phase model that consisted of a *t'* and tetragonal phase with a space group of $P4_2/nmc$ [78], a cubic phase with a space group of $Fm\bar{3}m$ [79], and a monoclinic phase with a space group of $P2_1/c$ [79]. The *t''* phase discussed elsewhere [79] was not included in the fitting because it is not expected to form upon cooling from an aging temperature of 1330°C. A pseudo-Voigt function that incorporates asymmetry and strain broadening was used to fit the peak profiles as described by Thompson, *et al.* [80]. The displacement parameters used in the model were obtained from Howard and Hill [81] and were fixed throughout the refinement.

### 4.3 Results

The XRD peaks for the dry and humid aged condition up to a LMP of 15.2 K (88 h) are shown in Fig. 4.3 with the *t'*, tetragonal, and cubic peaks superimposed. All aging conditions look indistinguishable up to 15.2 K (88 h), for both the dry and humid aging conditions. It is notable though, that as the aging time increases for both environmental conditions the peak positions gradually shift away from the *t'* phase and towards the tetragonal and cubic phases.

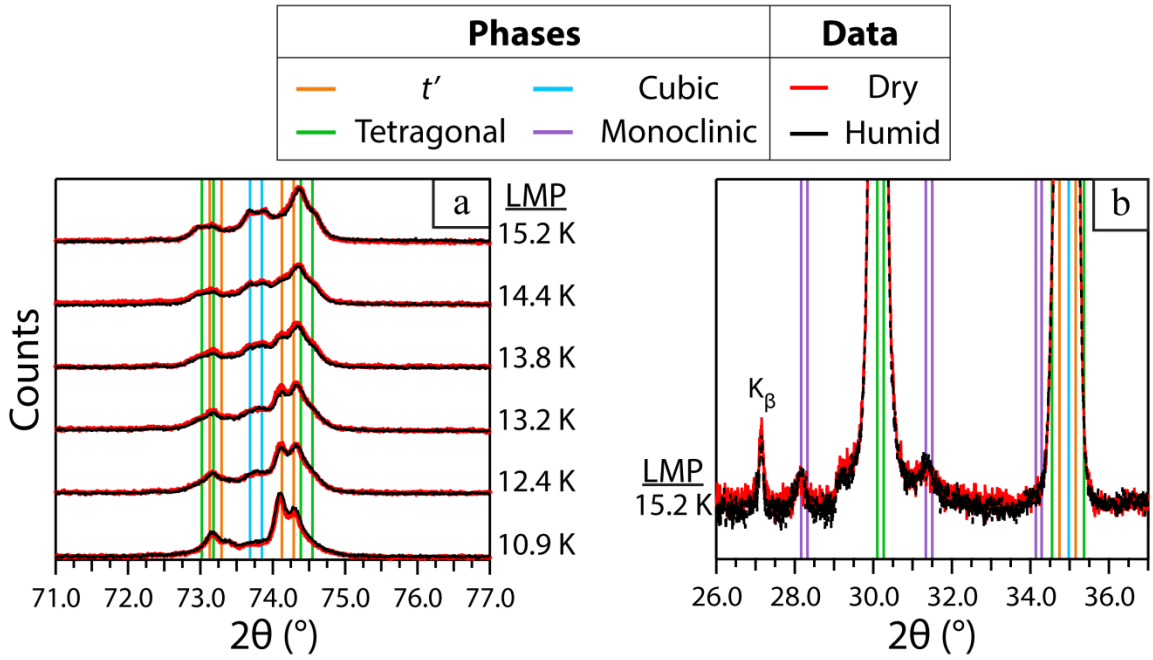


**Figure 4.3 XRD spectra of the dry- and humid-aged APS 8YSZ for: (a) LMP 10.9 – 15.2 K (6 to 88 h) with the (004) and (220) tetragonal planes and the (004) cubic plane and (b) LMP 15.2 K (88 h) showing the tetragonal planes (011), (002), and (110) and the monoclinic planes ($\bar{1}11$), (111), (002). The angular positions as determined from the GSAS model are superimposed for the *t'*, tetragonal, cubic, and monoclinic phases. The $K\alpha_1/K\alpha_2$ doublet is shown by a pair of phase lines for each plane of atoms.**

Figure 4.4 shows the XRD results for the aging of the APS 8YSZ in both dry and humid environments for 15.2 K (88 h) to 18.2 K (570 h) of aging. The trend of increased monoclinic formation for the humid-aged sample has continued after 18.2 K (570 h) of aging, as it did for 15.9 K (140 h) and 16.7 K (224 h) of aging. Also, the monoclinic formation is not the only change that is observed in the evolution of the phases during aging. There are also clear differences in the amount of cubic phase that is formed during the aging. In the humid environment, there is a decrease in the *t'* phase as the amount of the cubic phase increases. The amount of the tetragonal phase is also decreased in the humid environment due to the increased monoclinic formation.

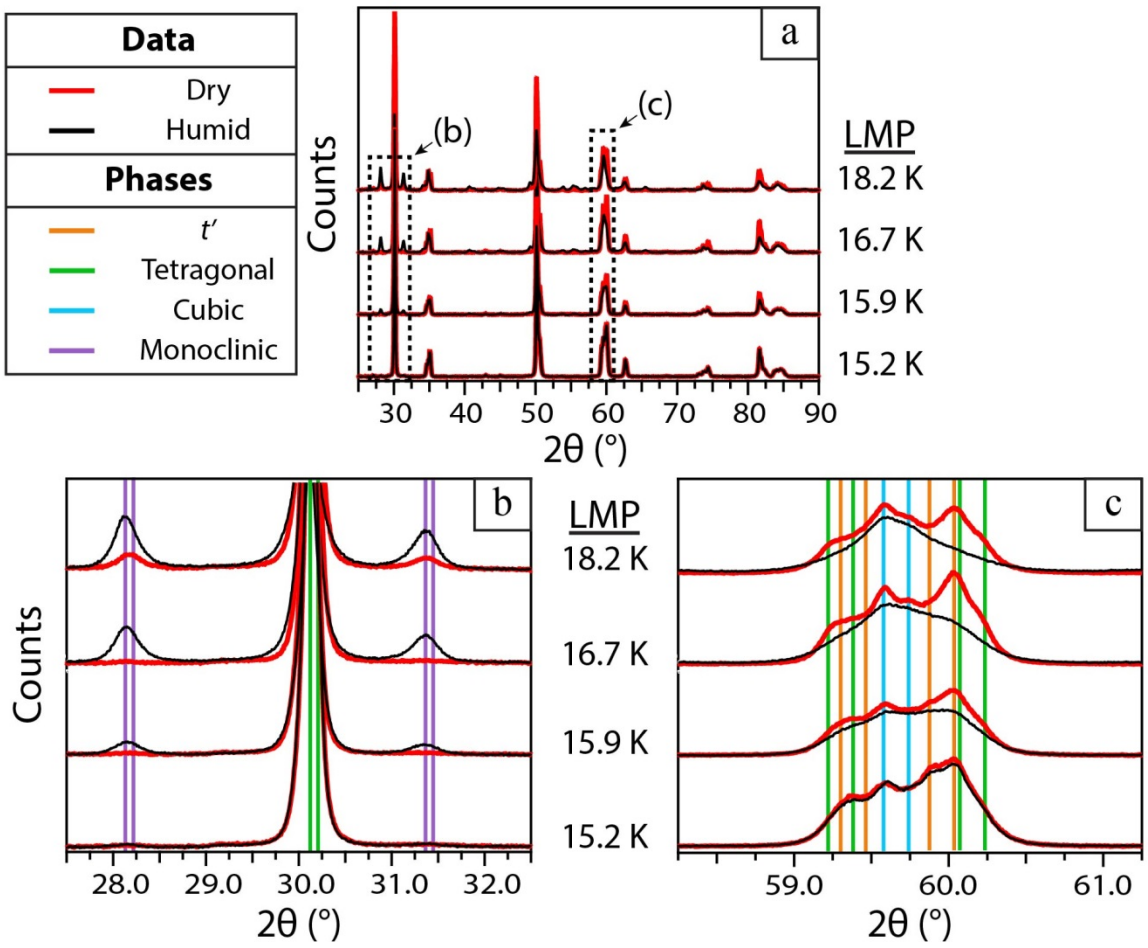


**Figure 4.4 XRD spectra of dry- and humid-aged APS 8YSZ from a LMP of 15.2 to 18.2 K (88 to 570 h) showing (a) the full spectrum, (b) the tetragonal plane (011) and the monoclinic planes ($\bar{1}11$) and (111), and (c) the tetragonal planes (013) and (121) and the (113) cubic plane. The angular positions as determined from the GSAS model are superimposed for the *t'*, tetragonal, cubic, and monoclinic phases. The $K\alpha_1/K\alpha_2$ doublet is shown by a pair of phase lines for each plane of atoms.**

Raman spectra of the as-received and aged APS 8YSZ are shown in Fig. 4.5. The six characteristic Raman modes of tetragonal zirconia can be identified in the as-received condition, as well as in samples aged from 10.9 K (6 h) through 15.2 K (88 h) in both humid and dry environments. After aging in both environments, the initial width of the peak at 260 $cm^{-1}$ narrows and the peak intensity ratio of the 640 $cm^{-1}$ peak to the 260 $cm^{-1}$ peak decreases relative to the as-received condition. There are no observable differences in the peaks obtained for the

two aging environments up to 15.2 K (88 h) exposure times (where the spectra for the dry and humid conditions have been offset in Fig. 4.5 only to avoid overlap of the spectra). However, starting at 15.9 K (140 h) there are many additional peaks in the Raman spectra for the humid-aging condition that are not observed in the dry-aging condition. These peaks are identified as the characteristic monoclinic peaks, and the intensities of these monoclinic peaks grow relative to the tetragonal peaks with further humid aging to 16.7 K (224 h). At this aging time, there are still no discernible monoclinic peaks that can be identified for the dry-aging condition. These Raman spectra results correlate well with the XRD spectra in that there is an increase in the amount of monoclinic phase formed in the samples after a LMP of 15.9 K (88 h) under exposure to the humid environment.

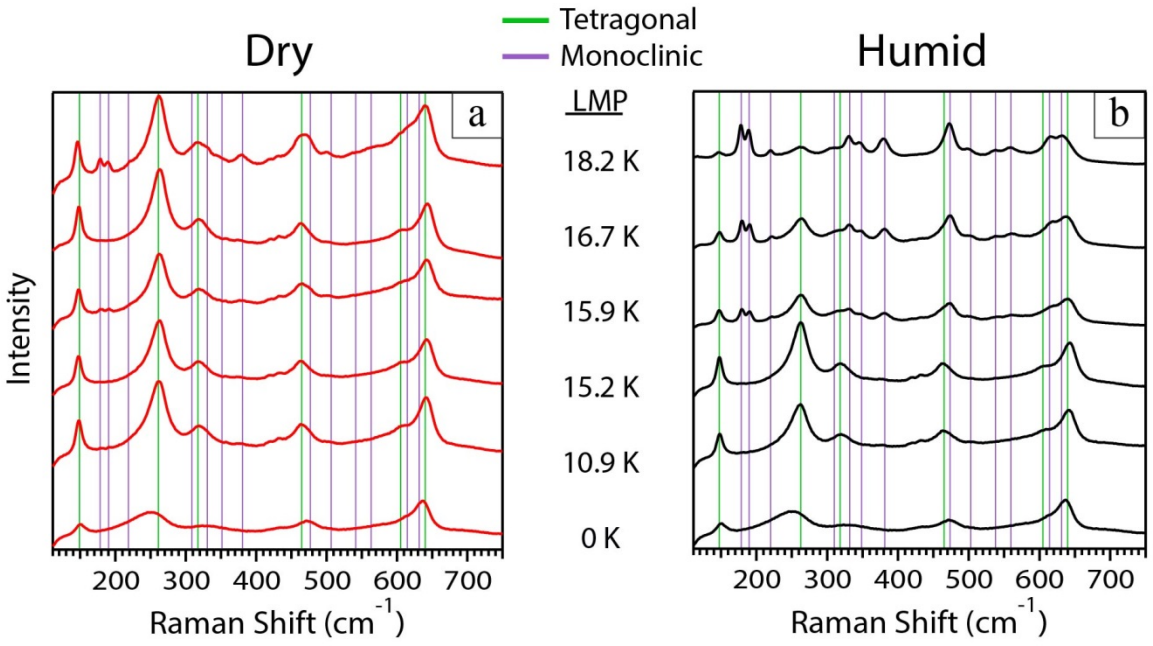


**Figure 4.5 Raman spectra of the dry- and humid-aged APS 8YSZ samples. The locations of the characteristic tetragonal and monoclinic peaks are indicated by different lines.**

Figure 4.6 shows a comparison of the XRD experimental data for the 16.7 K (224 h) dry- and humid-aged samples to the GSAS model. A quantitative metric for the quality of fit – the

weighted profile R value called $R_{wp}$ – gave a value less than 7.0% for both environments, which is consistent with the expectations for a Rietveld fit on data taken from conventional XRD equipment (a $R_{wp}$ of ~10%) [82]. Visual inspection of the quality-of-fit shows that the model accurately reflects both the locations of the peaks, as well as the relative peak intensities – indicating that both the lattice parameters and the atom positions of the model are quite accurate. At 16.7 K (224 h) of aging, there are clear differences in the shape and intensities of the peaks for the different aging environments. This is mostly due to the reduction of the *t'*, tetragonal, and cubic phases in favor of the increased growth of the monoclinic phase in the humid environment.

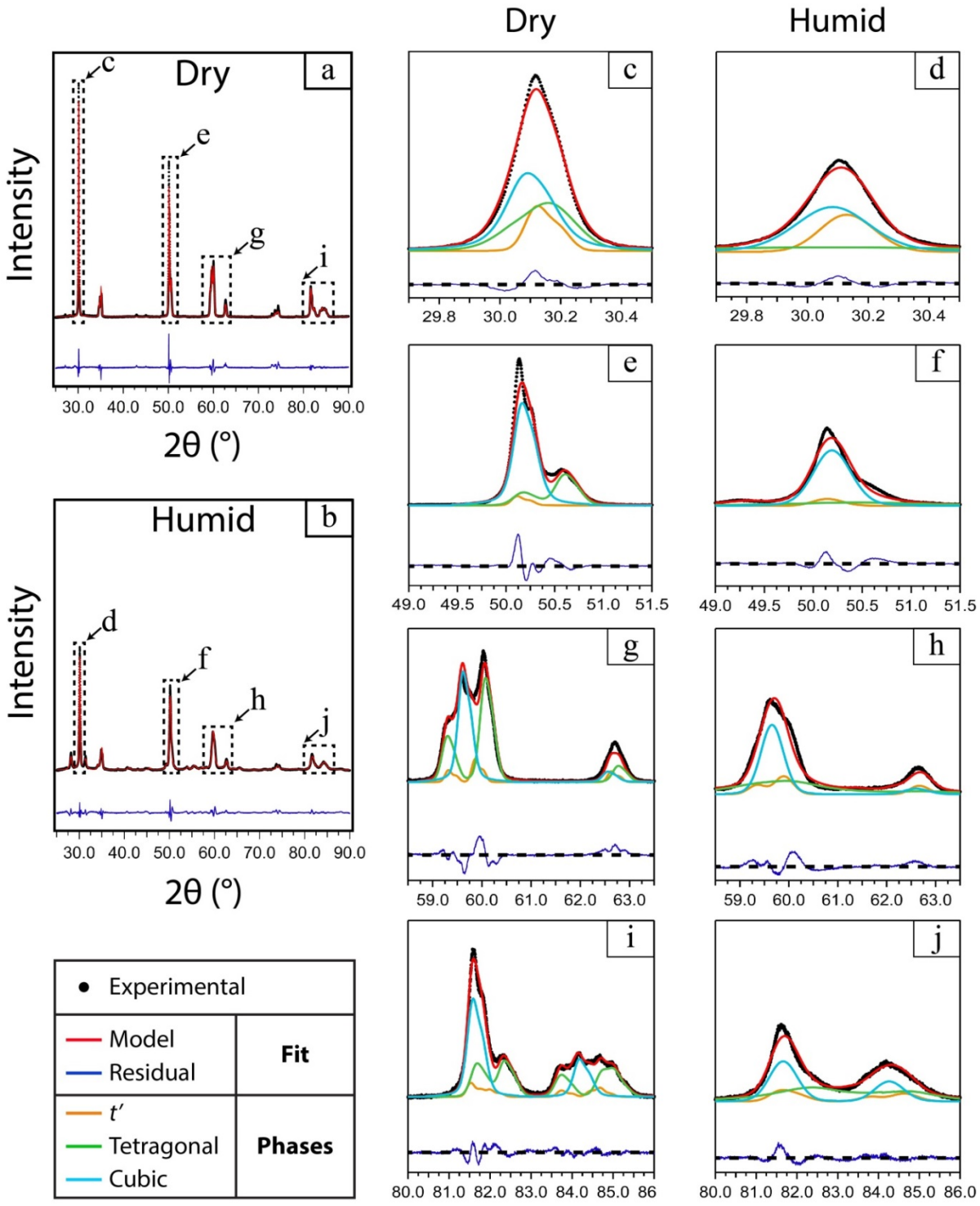


**Figure 4.6 A comparison of the XRD spectra from the 16.7 K (224 h) dry- and humid-aged samples as well as the corresponding 4-phase model from GSAS.**

Figure 4.7 shows the average phase fraction values and standard deviations from the Rietveld analysis performed on XRD spectra from the top, bottom, and polished-top of the 15.2 K (88 h) dry- and humid-aged 8YSZ samples. This was done in order to verify that the enhanced decomposition of the *t'* phase in the humid environment was not a result of yttria volatilization. The "top" refers to the side that faces up when placed in the crucible for aging testing and has a larger roughness than the reverse side – i.e. the "bottom." The "polished-top" refers to a separate sample from the same test that had its top side polished down to P2400 grit size with SiC grinding papers prior to the tube furnace exposure. Two of these samples were run in each aging environment. All XRD spectra of the different surfaces were taken at the same dwell time and step size. For the Rietveld analysis, the same macro was used to determine the phase fractions of each XRD spectrum. The standard deviations for all phase fractions shown are less than 0.015. The differences in the phase fraction values between the aging environments are greater than the standard deviations for three out of the four phases – the exception being the cubic phase. Therefore, the 15.2 K (88 h) humid-aged sample resulted in a faster decomposition of the *t'* phase compared to that of the dry-aged sample and a larger increase in the tetragonal and monoclinic phase fractions. Since the partial pressure of oxygen difference will be non-negligible between the "top" and "bottom" surface in contact with the loose yttria powder, it appears unlikely that volatilization of yttria is the means for the enhanced decomposition of the *t'* phase in humid environments.

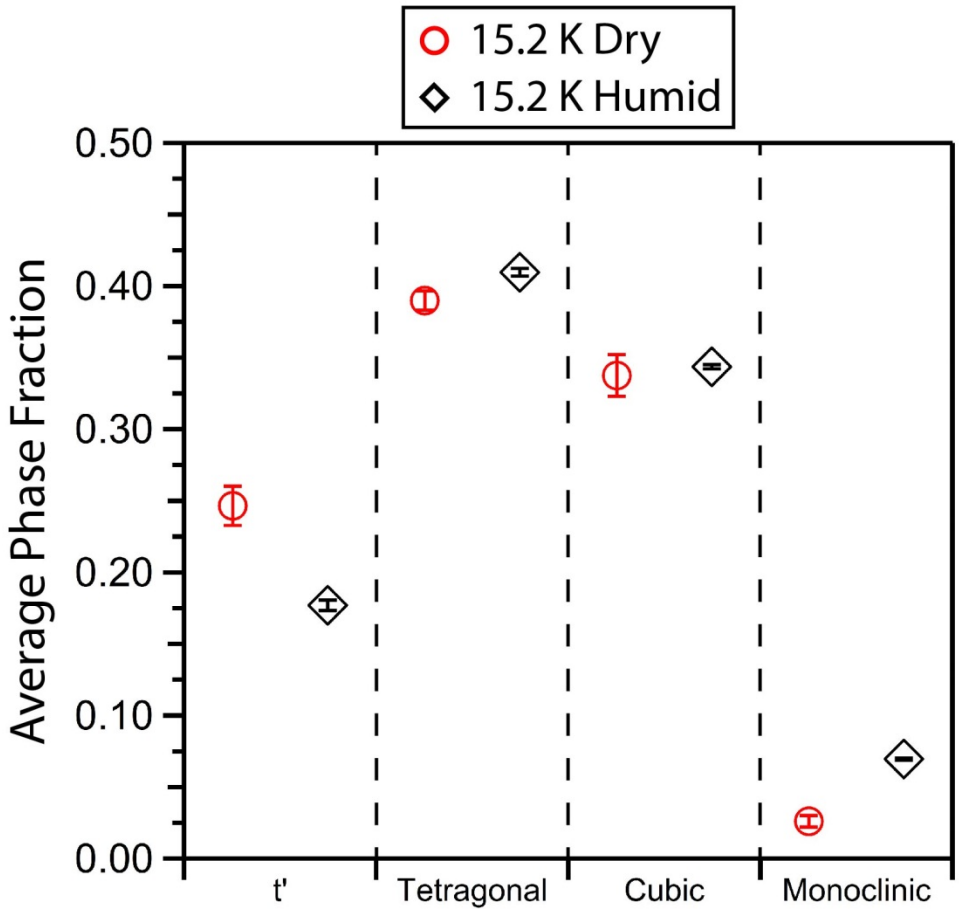


**Figure 4.7 Average phase fraction values and standard deviations from the Rietveld analysis performed on the top, bottom, and polished-top of the 15.2 K (88 h) dry- and humid-Aged 8YSZ samples. The phase fractions of the APS 8YSZ samples in the dry and humid environment were computed using the Rietveld method in GSAS.**

The evolution of the phase fractions of the samples as they age in the different environments, deduced from the GSAS results is shown in Fig. 4.8. As the samples age in both environments, the *t'* phase decreases and the tetragonal, cubic, and monoclinic phases increase with increasing LMP up to 15.2 K (88 h) as expected. The *t''* phase was not included in the Rietveld refinement as it is not expected to form at temperatures around 1330°C [60]. Differences in phase fractions between the environments are slight until a LMP of 13.8 K (37.2 h), where there are noticeable differences in the amount of the cubic and tetragonal phases formed and the amount of the *t'* phase that has been decomposed. At this LMP the amount of the

*t'* phase has decreased for the humid environment and the amount of the cubic and tetragonal phases have increased relative to the dry environment. The trend of the increased decomposition of the *t'* phase to the equilibrium phases for the humid-aging condition continues up to a LMP of 15.2 K (88 h) – prior to significant increases in the monoclinic phase. After 15.2 K (88 h), the trend is different because the tetragonal phase starts to decrease in both environments – more rapidly for the humid environment. This is expected as the monoclinic phase starts to increase significantly at this point for both environments – again at an accelerated rate for the humid environment. The cubic phase trend changes as well, with the humid environment forming less of the cubic phase than the dry one after 15.2 K (88 h). The decrease in the cubic phase formation for the final aging time in the humid environment is consistent with the work from Lipkin, *et al.*[60], where the amount of the cubic phase decreases for a subsequent aging time at large non-dimensional aging parameters. The one trend that continues after a LMP of 15.2 K (88 h) is the accelerated decomposition of the *t'* phase in the humid environment relative to the dry one.

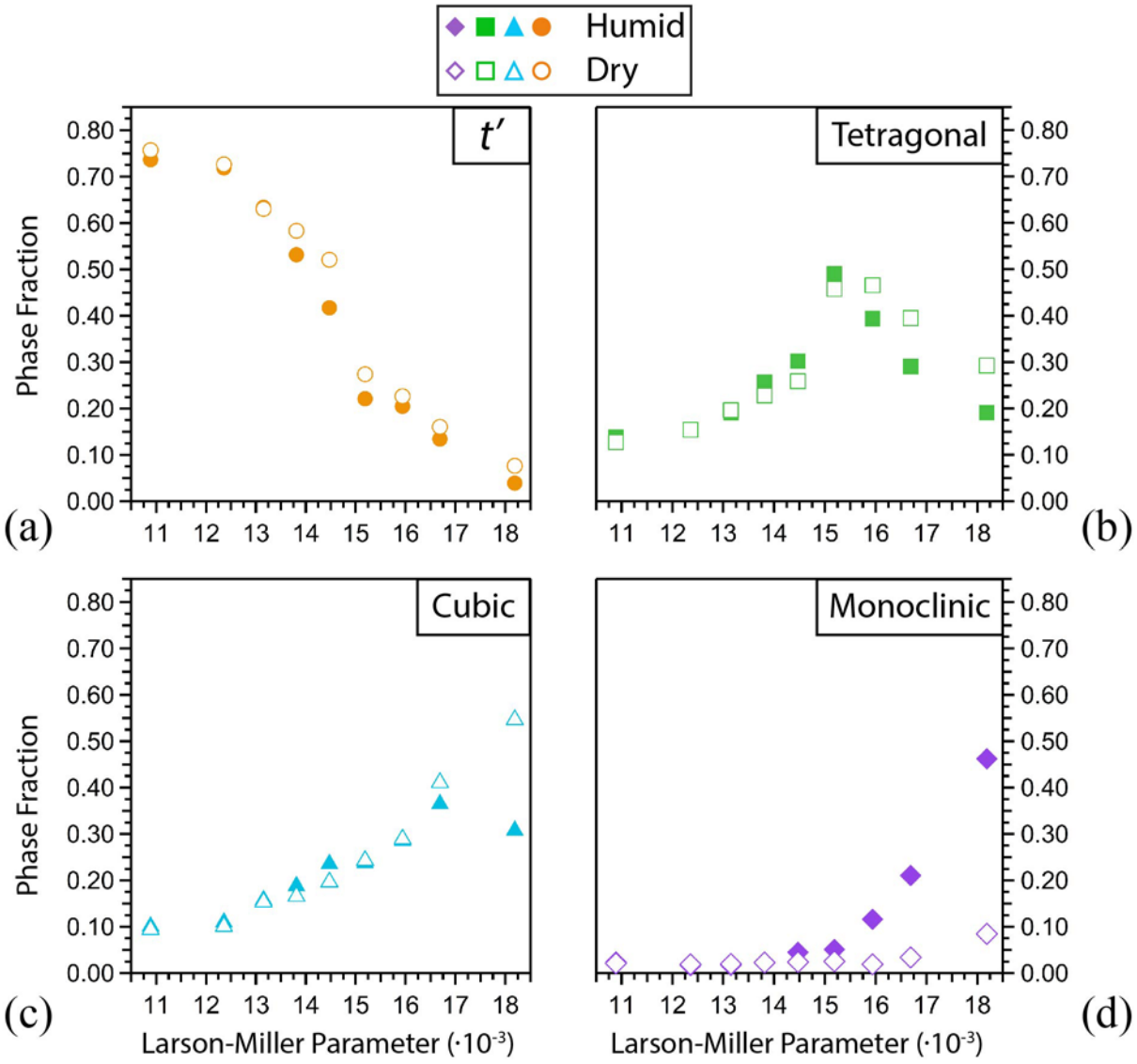


**Figure 4.8 The phase fractions of the APS 8YSZ samples in the dry and humid environment computed using the Rietveld method in GSAS.**

Fig. 4.9 shows the results for fitting the $A_{1g}$ mode of tetragonal zirconia at the 259 $cm^{-1}$ line for both the dry- and humid-aged YSZ. From 10.9 K (6 h) to 15.2 K (88 h), the 259 $cm^{-1}$ line shifts to higher wavenumbers, but there is little difference in the peak shifting between the different aging environments at these LMPs. However, with continued aging to 15.9 K (140 h), the 259 $cm^{-1}$ line shifts to a higher wavenumber for the humid environment, relative to the dry

environment. This increased amount of shifting for the humid aging continues for the longer exposure times of 16.7 K (224 h) and 18.2 K (570 h).

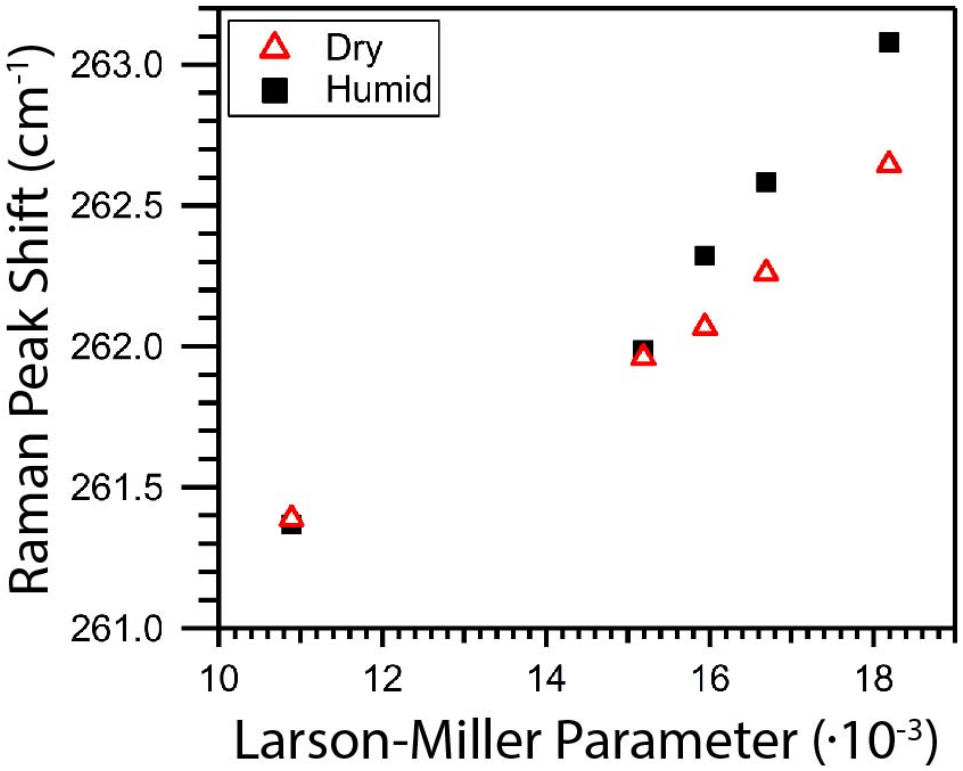


**Figure 4.9 Peak fitting of the $A_{1g}$ (259 $cm^{-1}$) mode of tetragonal zirconia for both the dry- and humid- aged environment.**

XRD data at selected 2θ locations is shown in Fig. 4.10, for increasing LMP in both aging environments. Figure 4.10 (a) shows the XRD data as the LMP increases from 10.9 (6 h) to 15.2 K (88 h) for 2θ values that correspond to some of the tetragonal and cubic peak locations. The tetragonal doublet at a 2θ of 74.3° shifts from a value of 74.32° at 10.9 K (6 h) to 74.37° at 15.2 K (88 h). This contrasts with the monoclinic peaks located at 2θ values of 28.2°, 31.4°, and 34.5° as they grow from a LMP of 15.2 K (88 h) to 16.7 K (570 h) as shown in Fig. 4.10 (b). With a step size of 0.004º, there is no observed shift in the growth of the monoclinic peaks with increasing LMP for the humid aging environment but only an increase in intensity. This

monoclinic growth occurs simultaneously with the decrease in intensity value of the tetragonal peak located at 30.15° as it shifts from 30. 13° at 15.2 K (88 h) to 30.11° at 16.7 K (570 h).

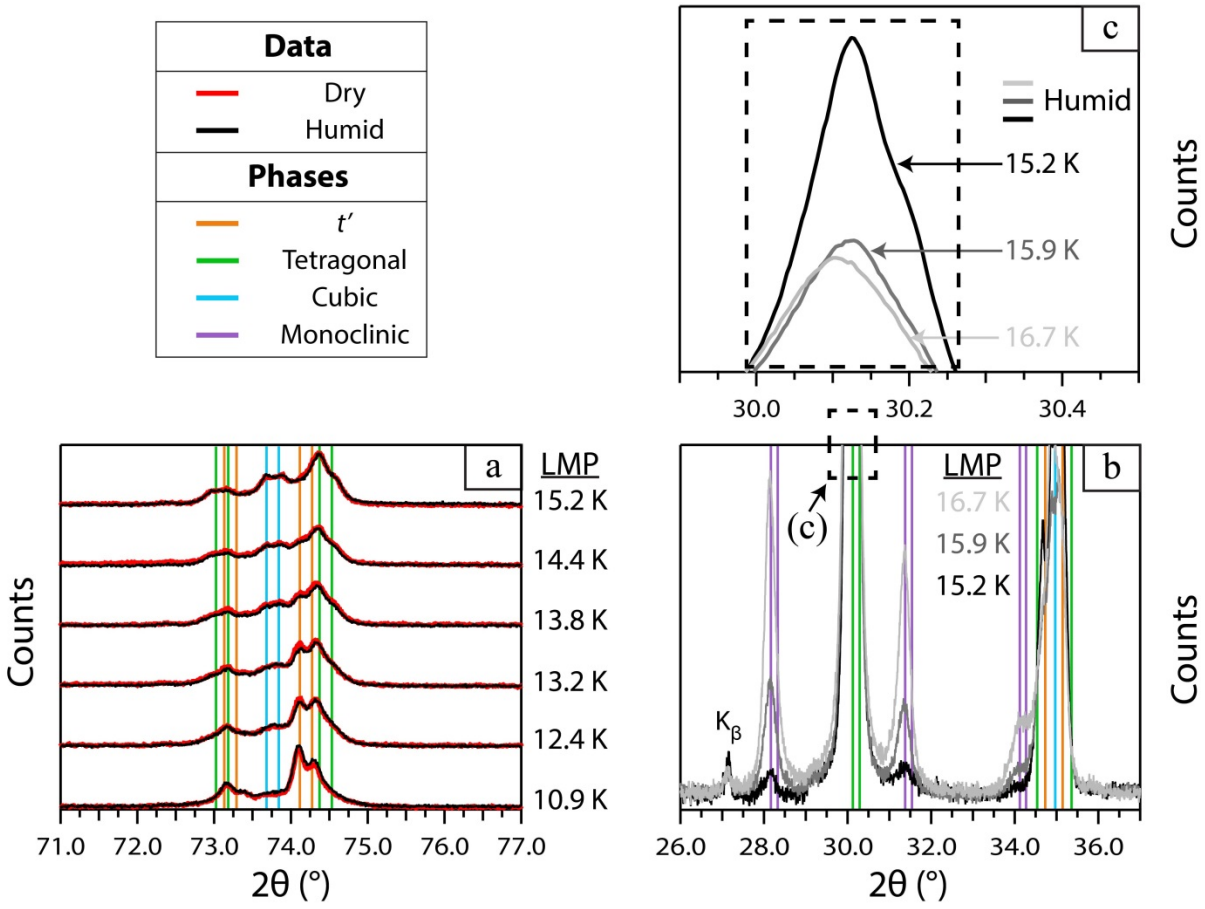


**Figure 4.10 A comparison of the XRD spectra for (a) the dry- and humid-aged samples at low LMPs, (b) the humid-aged samples at high LMPs, and (c) an expanded view of the box in (b). The XRD spectra shows (a) the tetragonal planes (004) and (220) and the cubic plane (004) and (b) the tetragonal planes (011), (002), and (110) and the monoclinic planes ($\bar{1}11$), (111), and (002). The angular positions as determined from the GSAS model are superimposed for the *t'*, tetragonal, cubic, and monoclinic phases. The $K\alpha_1/K\alpha_2$ doublet is shown by a pair of phase lines for each plane of atoms.**

Figure 4.11 shows a comparison of the XRD spectra for a 16.7 K (224 h), humid-aged sample that was cooled in the humid environment as well a sample that was aged for 219.5 h in a humid environment, purged of the humid environment for 2.25 h at the aging temperature, aged for 2.25 h in a dry environment, and then cooled in a dry environment. The entire length of

aging for this hybrid test was still 224 h (termed *hybrid 224 h* hereafter). The purpose of the hybrid 224 h test was to determine whether the monoclinic phase was forming only due to cooling in a humid environment. This transformation of the tetragonal phase to the monoclinic phase occurs at temperatures between 120-300°C in a humid environment due to LTD [71]. Therefore, to confirm that LTD was not the mechanism for the formation of the monoclinic phase in the humid aged sample, the hybrid 224 h test was performed. The 2.25 h purge was to ensure that the environment transitioned from one with 45% vol. of water vapor to one with no partial pressure of water vapor. The additional 2.25 h of dry heating was to confirm that the sample was actually in a dry environment prior to cool down. The XRD spectrum comparison shown in Fig. 4.11 indeed confirms that the aging was not purely in a humid environment. Figure 4.11 shows a difference in the amount of the monoclinic phase formed – (b) – and the evolution of the *t'* phase – (c). In addition, the presence of the monoclinic phase in the XRD spectra of the hybrid 224 h test confirms that LTD is not the means of the monoclinic formation, but is instead due to the conversion of the *t'* phase to the tetragonal phase at the aging temperature – which is then converted to the monoclinic phase by the martensitic transformation [60].

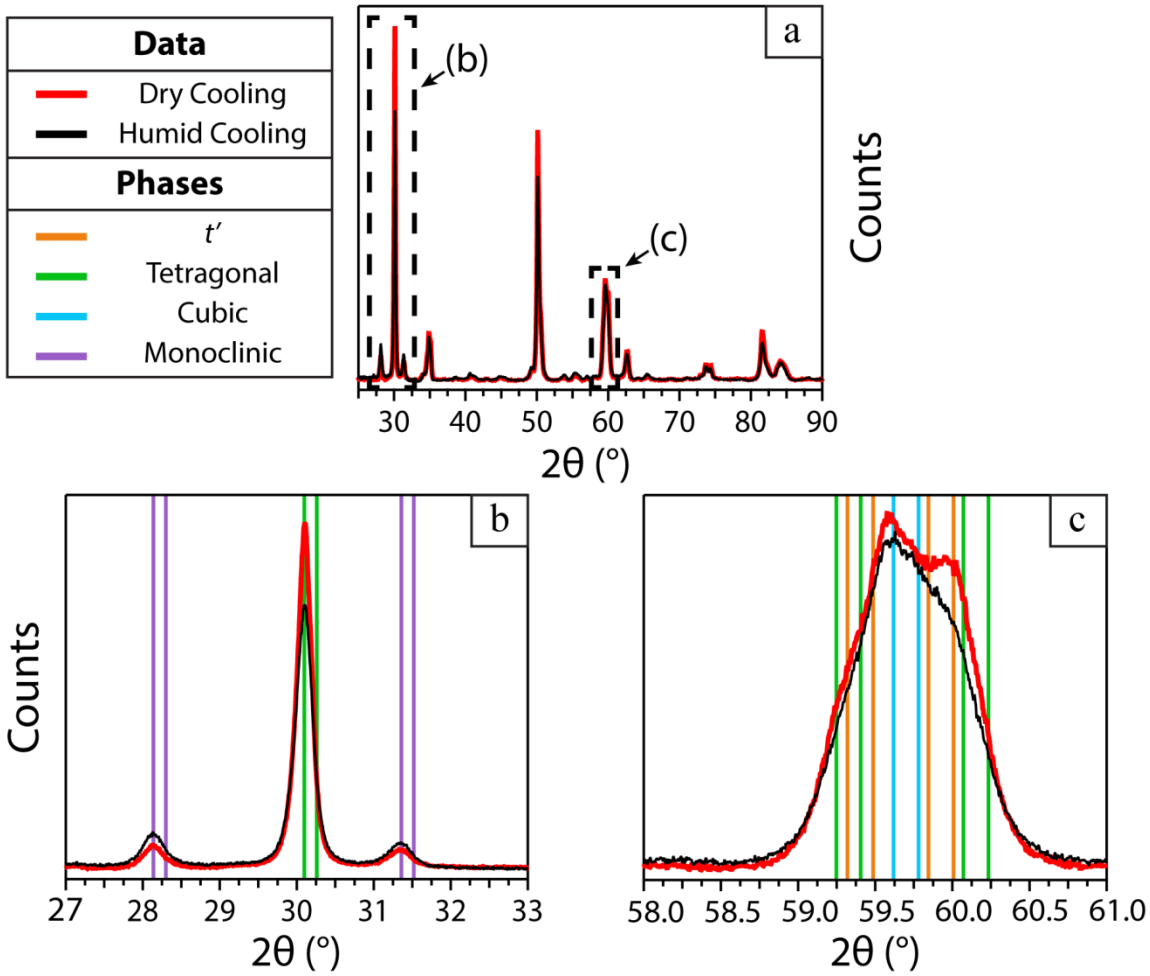


**Figure 4.11 XRD spectra of the APS 8YSZ samples aged for 16.7 K (224 h) in a dry or humid cooling condition showing (a) the full spectrum, (b) the tetragonal plane (011) and the monoclinic planes ($\bar{1}11$) and (111), and (c) the tetragonal planes (013) and (121) and the cubic plane (113). The angular positions as determined from the GSAS model are superimposed for the *t'*, tetragonal, cubic, and monoclinic phases. The $K\alpha_1/K\alpha_2$ doublet is shown by a pair of phase lines for each plane of atoms.**

Figure 4.12 shows the XRD results for the aging of the APS 8YSZ in a dry and humid oxidizing environment as well as a humid reducing environment for 15.9 K (140 h) of aging. The reducing humid environment caused more of the monoclinic phase to form than that of the dry environment. However, the reducing humid environment did not form the same amount of the monoclinic phase as that of the humid oxidizing environment. Also, the monoclinic formation is not the only change that is observed in the evolution of the phases during aging.

There are also clear differences in the amount of tetragonal and cubic phases that are formed during the aging. There is more of the tetragonal and cubic phase in the dry and reducing humid environment than that of the oxidizing humid environment. These results show that the humid reducing environment has an enhanced resistance to the monoclinic transformation compared to that of the humid oxidizing environment. Since a reducing environment without humidity would cause oxygen to be removed from YSZ, the results shown in Fig. 4.12 imply that a local equilibrium is set-up between the sample and the oxygen from the dissociated water vapor. Some of this oxygen is supplied to the sample, but not as much as in the case of the humid oxidizing sample, because oxygen has to be used to form the water that condenses outside of the furnace.

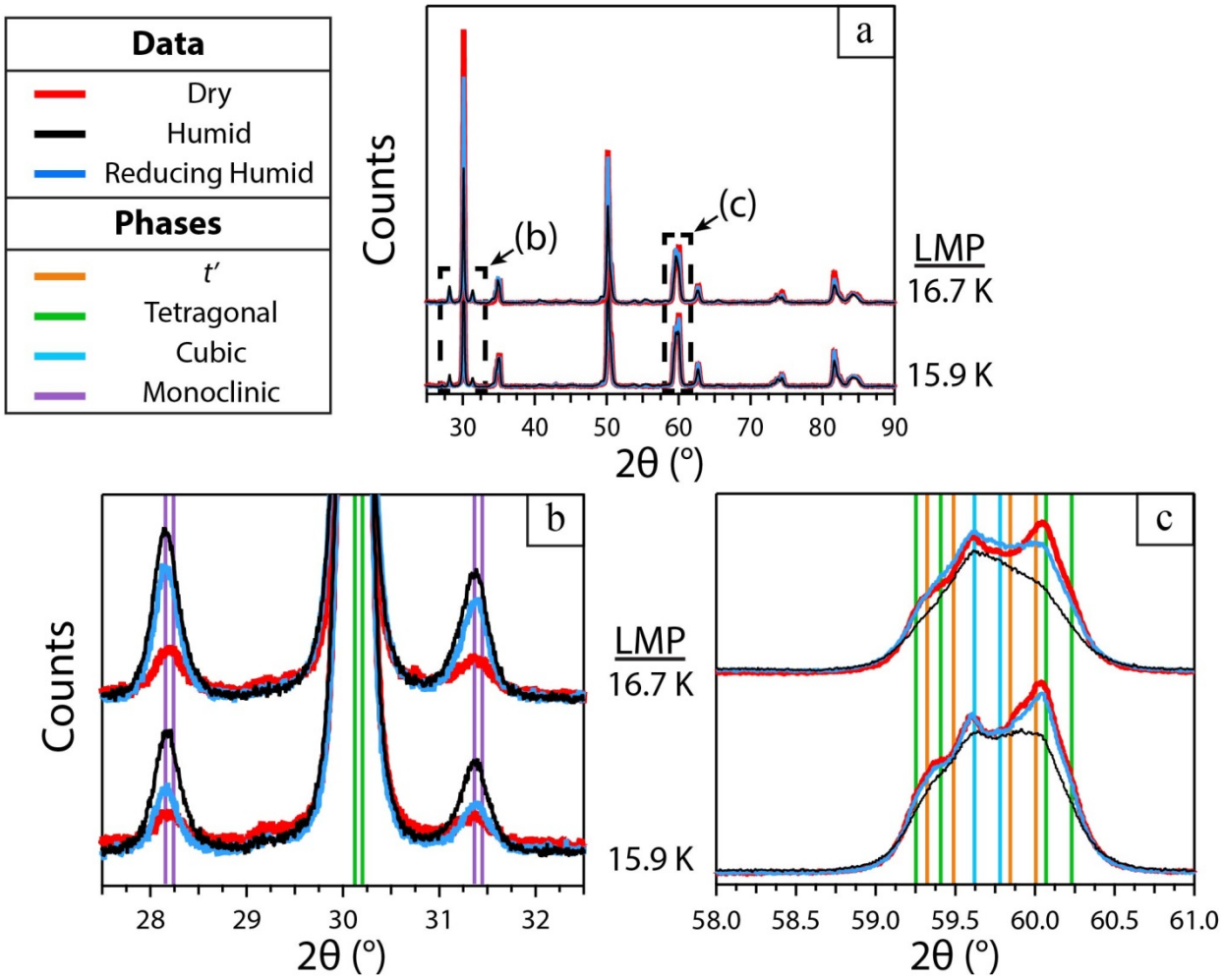


**Figure 4.12 XRD spectra of the APS 8YSZ samples aged for 140 h and 224 h (LMP = 15.9 K and 16.7 K) in an oxidizing or reducing environment showing (a) the full spectrum, (b) the tetragonal plane (011) and the monoclinic planes ($\bar{1}11$) and (111), and (c) the tetragonal planes (013) and (121) and the cubic plane (113). The angular positions as determined from the GSAS model are superimposed for the *t'*, tetragonal, cubic, and monoclinic phases. The $K\alpha_1/K\alpha_2$ doublet is shown by a pair of phase lines for each plane of atoms.**

### 4.4 Discussion

In order to understand the enhanced destabilization of the *t'* phase of 8YSZ in humid environments at high temperatures it is illustrative to examine the diffusion paths of yttrium in the APS microstructure. Previously two possible diffusion paths of yttrium in dry, elevated aging temperatures were postulated for the complex microstructure of APS [61]. The first path is based on the coarsening of the Y-rich and Y-lean domains (Modulated Path), and the second path

is dominated by the coarsening and growth of the cubic phase via depletion of Y from the tetragonal grains (Depletion Path). Both paths were thought to be present in the APS microstructure if there was inhomogeneity in grain size of the initial deposited 8YSZ. The juxtaposition of a large grain next to several small grains would cause equiaxed cubic grains to nucleate at grain boundaries due to the Depletion Path. Once the equiaxed grains are established, the Modulated Path would destabilize the *t'* phase of the adjacent larger grain by the presence of the Y-rich and Y-lean domains. The authors suggested that a larger initial grain size would increase the resistance of the tetragonal to the monoclinic transformation. However, this is at odds with the LTD in humid environments literature that has found that smaller initial grain sizes decreased the tetragonal to monoclinic transformation [65, 70]. This conflicting understanding may in part be explained by differences in destabilization between the *t'* and tetragonal phase. Jue *et al.* [35] found that the *t'* phase had superior resistance to the monoclinic phase transformation than the 3-mol%-yttria tetragonal zirconia – with no monoclinic phase formation after 1000 h at 275°C in air. This is despite the fact that the *t'* polycrystalline material had a large grain size of ~100 um. The authors attributed the difference in resistance between the *t'* and the tetragonal zirconia to differences in the ferroelastic domain size, with the smaller domains of the *t'* phase providing higher resistance. It seems unlikely then that the grain size alone is a factor in the destabilization of the *t'* phase in APS 8YSZ.

There is still uncertainty regarding the nature of how the *t'* phase transforms to the tetragonal and cubic phases in high-temperature, dry aging – i.e. by spinodal decomposition [36, 83] or a nucleation and growth mechanism [84, 85]. The aging XRD results for both the dry and humid environments provide evidence for spinodal decomposition. Before significant growth of the monoclinic phase – 15.2 K (88 h) in both aging environments – there is a gradual shifting of

the XRD peaks away from the *t'* phase and towards the tetragonal and cubic phases as shown in Figure 4.10 (a). The gradual shifting indicates slight changes in the lattice parameters and therefore in the chemistry of the 8YSZ from a metastable, homogenous composition to a more stable, non-uniform mixture of Y-rich and Y-lean composition. This result provides evidence for a spinodal decomposition as opposed to a nucleation and growth transformation, where it would be expected that the intensity of the XRD peaks corresponding to the new phase would come at the expense of the peaks corresponding to the parent phase. However, the nucleation and growth transformation is known to occur for the tetragonal to monoclinic phase transformation that occurs in both LTD [65] and high temperature aging of t-YSZ [86]. This is consistent with the results for the humid aging, as the total aging time is increased beyond 15.2 K (88 h) as shown in Figure 4.10 (b). The XRD and Raman spectroscopy results both show an increase in peaks corresponding to the monoclinic phase at the expense of the tetragonal phase. Therefore, it is concluded that monoclinic grains nucleate from tetragonal ones in high-temperature, humid aging after the *t'* phase has been decomposed to the cubic and tetragonal phases.

### 4.4.1 Evidence for Enhanced Yttrium Redistribution Via Raman Spectroscopy

The quantitative Raman spectroscopy analysis provides evidence that the humid environment is enhancing yttrium diffusion after the formation of the monoclinic phase. Raman spectroscopy was used by Lee *et al.* [87] to show the influence of dopant concentration on the shifting of two characteristic, tetragonal Raman modes – one at 259 $cm^{-1}$ and the second at 609 and 640 $cm^{-1}$. These two modes were singled out among the six tetragonal modes because they are believed to relate directly to the stretching of the two Zr-O bond lengths [87]. Different trends in the shifting of these Raman modes were found based on whether the dopant had an ionic radius that was oversized or undersized relative to zirconium. As the concentration of the

oversized-dopant $Ce^{4+}$ decreased in zirconia, the two Raman modes shifted to a higher wavenumber. $Y^{3+}$ is an oversized ion as well relative to the zirconium ion and will shift the two Raman modes in a similar manner as the $Ce^{4+}$ ion. Peak fitting of the 259 $cm^{-1}$ Raman mode – as shown in Figure 4.9 – indicates that aging of the APS 8YSZ in either environment agrees with the previous findings that a decrease in an oversized dopant causes the wavenumber to shift to a higher value. This indicates that yttrium is leaving the *t'*-parent phase during aging in either environment. However, the fitting also indicates that the shifting to a larger wavenumber is occurring faster for the humid-aged samples than for the dry-aged samples – after the formation of the monoclinic phase. Therefore, the diffusion of yttrium is enhanced by aging in the humid environment after the formation of the monoclinic phase in 8YSZ.

### 4.4.2 Possibility of Silica Impurity Effects

The shifting of the Raman tetragonal modes provides strong evidence that yttrium is leaving the *t'* phase at an accelerated rate in a high-temperature, humid environment, but the role of impurities in enhancing the diffusion of yttrium during humid-aging is unclear. Impurities in commercially available 8YSZ powders were found to play a large role in cation diffusion pathways during the annealing of the powders. Heuer, *et al.* [88] identified an amorphous, silicate phase that was continuous along grain boundaries post-annealing by TEM imaging. This glassy phase was proposed to dissolve the parent microstructure and deposit a yttria-enriched precipitate free zone. A more recent analysis by Krogstad, *et al.* [61] also found pockets of silica at grain boundaries in APS 8YSZ after aging these materials in air. Silica impurities are also likely present in the APS 8YSZ used here, and are expected to have a role in cation diffusion. The question that arises is how do water species affect the silica impurities in enhancing yttrium diffusion? Davis, *et al.*[67] investigated the effect of varying Si content – from 56 to 760 ppm –

on the LTD of zirconia with different yttria compositions in water vapor at 250°C. Although the authors had hypothesized that water vapor would react with the glassy silicates in a stress corrosion mechanism, the authors found no differences in the samples after aging despite the significant variation in Si content.

At temperatures relevant to this study, it is anticipated that some of the silica impurities in APS 8YSZ would volatilize as hydroxyl groups. Jacobson, *et al.* [89] confirmed that silica will volatilize primarily as $Si(OH)_4$ at 1300°C and at a partial pressure of 0.5 bar $H_2O$ – conditions similar to the humid conditions utilized in this study. Therefore, while a glassy silicate phase is important as a yttrium diffusion pathway during the high-temperature aging of APS 8YSZ, it is not likely to enhance the diffusion of yttrium in a humid environments relative to a dry one. The detailed role of silica impurities and microstructure on the humid aging of APS 8YSZ is currently being investigated by TEM analysis.

### 4.4.3 Proposed Mechanism for Water Vapor Enhanced Phase Evolution

The enhanced destabilization of the *t'* phase in high temperature, humid environments is explained in terms of proton incorporation and the enhanced ability to overcome the coherency strains that exist between the tetragonal and cubic domains in 8YSZ. Water molecules can incorporate protons into 8YSZ in a similar manner as that which was proposed by Prinz et al. [76]:

$$H_2O + V_O^{\bullet\bullet} + O_O^X \xrightarrow{YSZ} 2(OH)_O^{\bullet}$$

While incorporation of these ions into the lattice is possible, it is more energetically favorable for them to travel along splat/grain boundaries[16]. The oxygen anions are not anticipated to have a dominant effect here in destabilizing the tetragonal phase as they do in LTD. This is due to the fact that the enhanced destabilization is occurring at a temperature where the

tetragonal phase is at equilibrium for 8YSZ as opposed to LTD where the monoclinic phase is at equilibrium. However, proton incorporation and migration in the 8YSZ is proposed to play a more pivotal role in the high temperature, humid degradation. Although historically YSZ has not been considered a proton-conductor, recent computational studies support the incorporation and long-range transportation of protons in YSZ by "hopping" between close oxygen ions [72, 73]. Furthermore, evidence of proton incorporation via the formation of hydroxyl groups has also been demonstrated in YSZ thin films at temperatures below 450°C [75, 76]. Therefore, there is theoretical and experimental support for protons to be incorporated into the structure of YSZ and influence the destabilization of the tetragonal phase.

However, the fact that there is a delay in seeing the monoclinic phase or significant changes in the evolution of the *t'* phase at exposure times less than 15.9 K (140 h) for the humid environment suggests the presence of an incubation period that needs to be surpassed prior to the tetragonal phase transforming into the monoclinic phase. This incubation period is likely linked to the coherently strained interfaces between the tetragonal and cubic phases in the 8YSZ [36]. A humid environment could decrease the incubation time by causing the size of the oxygen sites to become smaller and effectively hydroxyl groups via the proton "hopping" mechanism. The smaller hydroxyl groups would allow for a larger displacement of the oxygen atoms along the c-axis—or an increase in the tetragonality. This would explain the increased formation of the tetragonal phase during humid aging observed in the Rietveld refinement results of Fig. 4.8. Therefore, it is proposed that aging in a humid environment would allow for the coherency strain to be overcome faster by increasing the rate at which the tetragonal domains coarsen. This enhanced coarsening rate would ultimately cause the tetragonal phase to reach the size at which it is susceptible to monoclinic transformation faster as well. A microstructure investigation is

currently under way to determine if there is an enhanced coarsening of the domain size in humid environments.

There is the possibility that a high temperature, humid environment could be changing the metastable phase boundary line shown in Fig. 4.1 and thus modifying the change in Gibbs free energy associated with the tetragonal and monoclinic phases. Indeed, the comparison of the *hybrid 224 h* test and the humid 224 h test shown in Fig. 4.11 indicate that the humid environment is likely shifting the metastable phase boundary line and causing the tetragonal to monoclinic phase transformation to occur sooner. Figure 4.11 shows that different amounts of the monoclinic phase formed between the tests, even though both tests had identical environmental aging for 219.5 h and only differed for 4.5 h of aging. If the water vapor was affecting only the metastable phase boundary line and otherwise had no difference from that of the dry environment at the aging temperature, then the *hybrid 224 h* test should have different amounts of monoclinic phase form as that of the corresponding 224 h humid test. The differences that are observed in the XRD spectra must be the result of small shifts in the metastable phase boundary line that occur while aging in a different environment for 4.5 h. This is indicative of a phase destabilization that is occurring due to different amounts of associated strain between the coherent tetragonal and cubic interfaces.

## 4.5 Summary and Conclusions

The high-temperature, humid aging of APS 8YSZ has shown an enhanced de-stabilization of the *t'* phase compared to that of a dry environment. X-ray diffraction and Raman spectroscopy characterization show a similar decomposition of the *t'* phase to the thermodynamically stable cubic and tetragonal phases up to 15.2 K (88 h) of aging at 1330°C. However, after 15.9 K (140 h) of aging, the amount of monoclinic phase fomration has increased in the humid environment relative to that of a dry one. In addition, the XRD results provide evidence for a spinodal

decomposition of the *t'* phase as opposed to the nucleation and growth of the tetragonal and cubic phases. The mechanism by which the monoclinic transformation is accelerated is explained by the incorporation of protons via hydroxyl group formation. The hopping of such protons at neighboring oxygen sites would allow these sites to become smaller and increase their distortion in the lattice. Such an increase in tetragonality would allow the coherency strain between bound cubic and tetragonal phases to be overcome faster in a humid environment. The tetragonal phases could thus coarsen faster and reach a size that would cause the monoclinic phase to nucleate faster in this humid environment. The revelation of accelerated monoclinic phase transformation of the *t'* phase by high temperature, humid aging should promote a better understanding of the expected durability of APS 8YSZ coatings used in power generation gas turbines with high-hydrogen content fuels.

# 5 Chapter 5: Accelerated Aging of Yttria-Stabilized Zirconia Thermal Barrier Coatings in High Water Vapor Content, Elevated Temperature Environments: Microstructural Investigation


## Abstract

The microstructure related to the dry- and humid-aging of free-standing APS, 8YSZ coatings is correlated to the phase evolution of the *t'* phase as revealed by XRD and Raman spectroscopy. The FIB pull-out method was employed to extract lamellae from the bulk samples aged in the dry and humid environments for STEM in the SEM and TEM analysis. The high-angle annular dark field (HAADF) detector and EDS were used to determine the ferroelastic domain sizes of the dry- and humid-aged samples. The domains were found to be larger and more numerous for the humid-aged samples than for their dry-aged counterparts at the equivalent amount of aging for three distinct aging times. The size and the amount of the domains are related to the differences in phase evolution observed between the dry- and humid-aging environments. This chapter, therefore, provides a microstructural context for understanding the enhanced destabilization of the *t'* phase in a high temperature, humid-aging environment relative to that of a dry one.


## 5.1 Introduction

The role of the microstructure during the thermal aging of APS 8YSZ in humid and dry environments is described here in relation to the XRD and Raman Spectroscopy results. While APS 8YSZ has been historically stable at temperatures relative to gas-turbine engines, higher efficiency demands have pushed the inlet turbine temperatures to higher values. New concerns have been raised about the phase stability of the metastable *t'* phase at higher operating temperatures in a series of papers [60, 61]. These previous works focused on aging in air or relatively dry environments, while the influence of water vapor on the aging process wasn't explicitly considered. However, the use of high-hydrogen content fuels such as synthetic gas

(syngas) in Integrated Gasification Combined Cycle (IGCC) power plants provides a need to understand the role of water vapor in the aging process. The use of syngas and/or stem injection to suppress $NO_x$ emissions from gas turbines can cause a fourfold increase of the water vapor content in the combustion zone [3]. Therefore, this investigation describes the influence of water vapor in the high-temperature aging of APS 8YSZ while providing insights into the mechanisms driving this aging process.

The XRD and Raman spectroscopy characterization of the high temperature, humid aging (HTD) of the APS samples indicated an enhanced destabilization of the *t'* phase relative to dry aging. A general mechanism was proposed suggesting that protons and oxygen anions derived from water vapor were incorporated into the defect structure of YSZ and thereby altered the destabilization of the *t'* phase. While the quantitative Raman results implied that yttrium was diffusing out of the *t'* phase faster in a humid environment, a more comprehensive mechanism could not be deduced from the phase analysis alone. To better understand the mechanism behind the enhanced destabilization of HTD, this chapter will describe how the microstructural evolution taking place in the APS 8YSZ drives the associated phase evolution.

Electron microscopy has been useful to evaluate the microstructure of YSZ exposed to high temperatures for prolonged periods. The resulting microstructure after exposure is highly dependent upon the phase path taken by the YSZ. For example, rapid cooling from the cubic to *t'* phase (c→*c'*→*t'*) results in a "herringbone" microstructure consisting of twins [90-92], while high temperature aging of the *t'* phase results in a modulated microstructure of alternating Y-rich and Y-lean domains (*t'*→t + c) [61, 83, 93]. This work focuses on the transformation of the *t'* phase to the cubic and tetragonal phases upon cooling from 1330°C and will emphasize previous studies that have evaluated this phase path. Recently the microstructure of both APS and electron

beam physical vapor deposition of (EB-PVD) 8YSZ has been revealed by TEM after high temperature aging [36, 61]. The formation of the modulated microstructure in a thermal barrier coating was first described in relation to the high temperature aging of EB-PVD 8YSZ [36]. Here, the modulating domains were described to coarsen until the domains were no longer coherent—but still left a somewhat uniform distribution of Y-lean domains. However, the APS 8YSZ was described to have a similar but distinct modulating microstructure because of its more complicated initial grain structure [61]. The presence of variable grain sizes in the initial APS 8YSZ was proposed to give rise to two different pathways: 1) coarsening of the modulated structure in the case of large grains like the EB-PVD 8YSZ and 2) coarsening followed by depletion of yttrium from the tetragonal phase in the case of small grains. The formation of tetragonal and cubic grains by the second pathway can destabilize the larger grains having the modulated microstructure. There are, therefore, more inferred routes for the initial *t'* phase to decompose in the APS 8YSZ than in the EB-PVD 8YSZ.

While the evolution of the microstructure with the HTD of APS 8YSZ is currently unknown, previous work has tried to identify the microstructure characteristics for the humid aging of YSZ at *low* temperatures—or low-temperature degradation (LTD). For LTD, the tetragonal phase of YSZ will readily transform to the monoclinic phase at temperatures less than 300ºC in moist air [64]. Smaller grain sizes in YSZ have been purportedly correlated with an increase in the resistance to LTD [66-68]. While this has been a consistent finding, work by Virkar et al. has suggested that the size of the ferroelastic domains in the microstructure is a more precise way for determining the resistance to LTD [35]. The author's subjected *t'* 8YSZ and 3-mol%-yttria tetragonal zirconia (3YSZ) to various grinding and heat treatments followed by LTD exposure. While the 3YSZ readily converted to the monoclinic phase, no monoclinic

phase was detected for the *t'* sample after 1000 h—despite the fact that the *t'* polycrystalline material had a large grain size of ~100 um. However, surface grinding enhanced the resistance of the tetragonal phase to LTD, while having the opposite effect on the *t'* phase. The grinding treatment was said to change the domain size inside the grains—enlarging the domains in the case of the tetragonal phase and thereby increasing the resistance to LTD. A similar influence on the orientation of the domains—or texture—was also more recently found to influence the resistance of YSZ to LTD [94]. These results suggest that the domain size may be a more accurate microstructural feature in determining the resistance of YSZ to LTD.

While there is some understanding of the microstructure evolution for high temperature, dry aging and LTD, none currently exists for HTD. There is a need, therefore, to understand the microstructure as it evolves during HTD and its role in dictating phase transformations. This chapter will detail the microstructure that corresponds to where the rate of phase evolution changes between the dry and humid aging environments. STEM and TEM will be used to determine the domain sizes from lamellae removed from the bulk samples by the FIB pull-out method. The domain sizes for the humid-aged samples will be shown to be larger than the dry-aged samples at the equivalent amount of aging. The larger domain sizes of the humid-aged samples are more easily transformed into the monoclinic phase, providing a microstructural context for the enhanced transformation of the *t'* phase during HTD. This microstructure study will further provide evidence for the pivotal role of domain sizes in the destabilization of the *t'* phase as suggested by some, while also helping to better understand the destabilization of the *t'* phase during high temperature, dry aging.

## 5.2 Experimental

The fabrication details of the free standing, APS 8YSZ coatings and the conditions used for the dry- and humid-aging were described in the previous chapter and will only be described

in brief here. Samples were aged at different times but always at 1330 ºC in order to avoid crossing the $T_0^{(c/t)}$ transformation line and forming the *t''*. This avoided the formation of another tetragonal phase with similar lattice parameters and less uncertainty in designating the three distinct tetragonal phases. A Larson Miller parameter was used to normalize the time and temperature aging conditions as done previously [62]. The samples to be analyzed in this study were chosen according to where striking differences where observed between the dry- and humid-aging environments—an aging time of 15.9 K (140 h). Therefore, samples exposed to this amount of aging time from both environments—as well samples immediately before and after this aging time—were used for analysis. Lamella were removed from the surface of samples that were polished prior to aging through the use of a dual-beam SEM (Quanta 3D; FEI, Hillsboro, OR).

The lamella samples were analyzed by using STEM in a high resolution Magellan 400 XHR SEM (FEI). The HAADF imaging mode of the STEM detector was used in order to identify differences in the chemistry within grains. EDS was performed with the STEM detector in order to verify that the changes in contrast from the HAADF images were due to changes in yttrium content. The lamellae were also analyzed in a CM-20 conventional TEM (FEI) in order to provide complimentary information of the domains and site-specific diffraction information. Dark-field TEM images were used to highlight the domains from the surrounding material by the differences in orientation. Selected area diffraction (SAD) images were taken to identify phases present in the grains of the lamellae and to identify the reflections used to form a bright-field or dark-field image. All imaging and diffraction techniques helped provide evidence for the difference in domain size of the samples aged for the same amount of time but in different environments.

X-ray Photoelectron Spectroscopy was performed on select dry and humid aged samples in order to determine if any water –derived species was being formed on the surface of the samples. A monochromatic x-ray source was used to obtain the spectra with an emission current of 20 mA and a resolution of 0.4 eV. Low energy secondary electrons were passed over the surface of the samples by the use of a charge neutralizer in order to reduce charging on the sample surface. The dwell time for each spectrum was 300 ms and multiple sweeps were averaged together in order to obtain the spectral peaks shown. The chamber in which spectral measurements were made was at a vacuum of $2.0 \bullet 10^{-8}$ Torr or higher.

## 5.3 Results

### 5.3.1 15.2 K (88 h) Aging

Figure 5.1 shows HAADF STEM images of the 15.2 K (88 h) dry- and humid-aged samples. The contrast of these images is directly related to the atomic number. A dark contrast indicates a lower atomic number while a bright contrast indicates a higher atomic number. In both the environments, there is evidence of chemically-modulating domains as indicated by the alternating changes of contrast. However, the domain sizes of the 15.2 K (88 h) dry-aged sample are smaller overall than that of the 15.2 K (88 h) humid-aged sample. For the dry-aged sample, the majority of the domains range from 3 to 7 nm, while for the humid-aged sample the majority of the domains range from 12 to 17 nm. It should be noted that there appear to be larger domains (16 nm) located in the dry sample as shown in the bottom left corner of Fig. 5.1 (b). However, these only appear to be in one grain out of at least three observed in the lamella and are fewer in number than domains of the same size in the 15.2 K (88 h) humid sample. This matches the anticipated result of having the domains be overall slightly larger than that of the dry-aged. Furthermore, there is a difference in the density of domains observed between the two aging environments. In the case of the 15.2 K (88 h) humid sample, there is an entire grain that seems

to consist of chemically modulating domains—as shown in Fig. 5.1 (a)—which is not found in the 15.2 K (88 h) dry-aged sample.

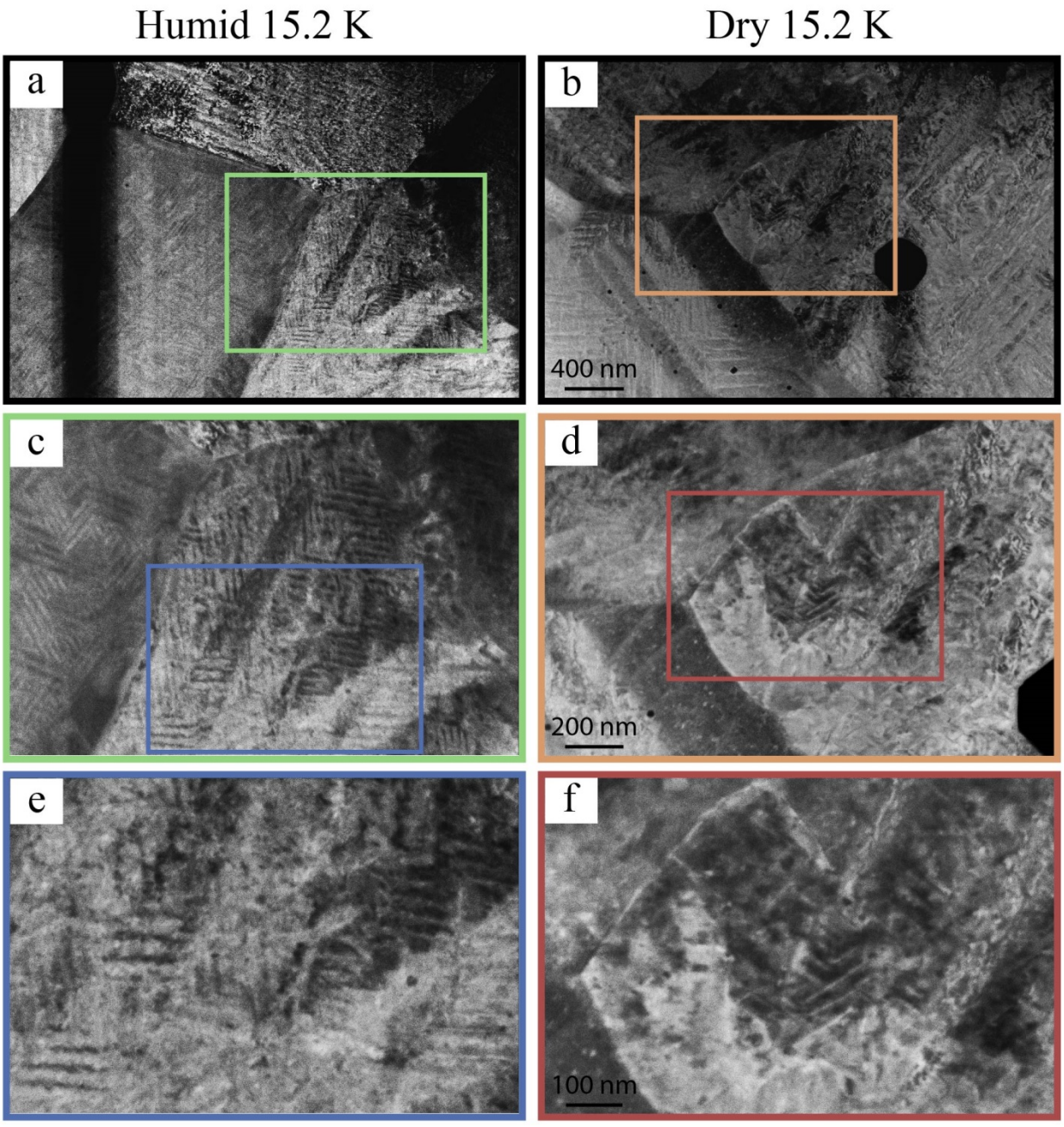


**Figure 5.1 HAADF STEM images of the 15.2 K (88 h) aged samples showing the humid-aged sample in (a), (c), and (e) and the dry-aged sample in (b), (d), and (f).**

Figure 5.2 shows bright-field TEM images of the 15.2 K (88 h) dry- and humid-aged samples. The images in (c), (e), (d), and (f) are higher magnification images of the regions contained in the rectangles of (a), (c), (b), and (d), respectively. There appear to be domains in the 15.2 K (88 h) sample which are not apparent in the regions shown of the 15.2 K (88 h) dry sample. The bright-field images cannot confirm this alone because of the contribution from Bragg-diffraction contrast. However, the dark-field images of the 15.2 K (88 h) humid sample in Fig. 5.3 (b), (d), and (f) provide further evidence that these lamella regions are the domains. Figure 5.3 also shows two SAD patterns from the regions shown in Fig. 5.3 (a) – (d). These two SAD patterns are from the same region but Fig. 5.2 (f) has the beam blocker removed.

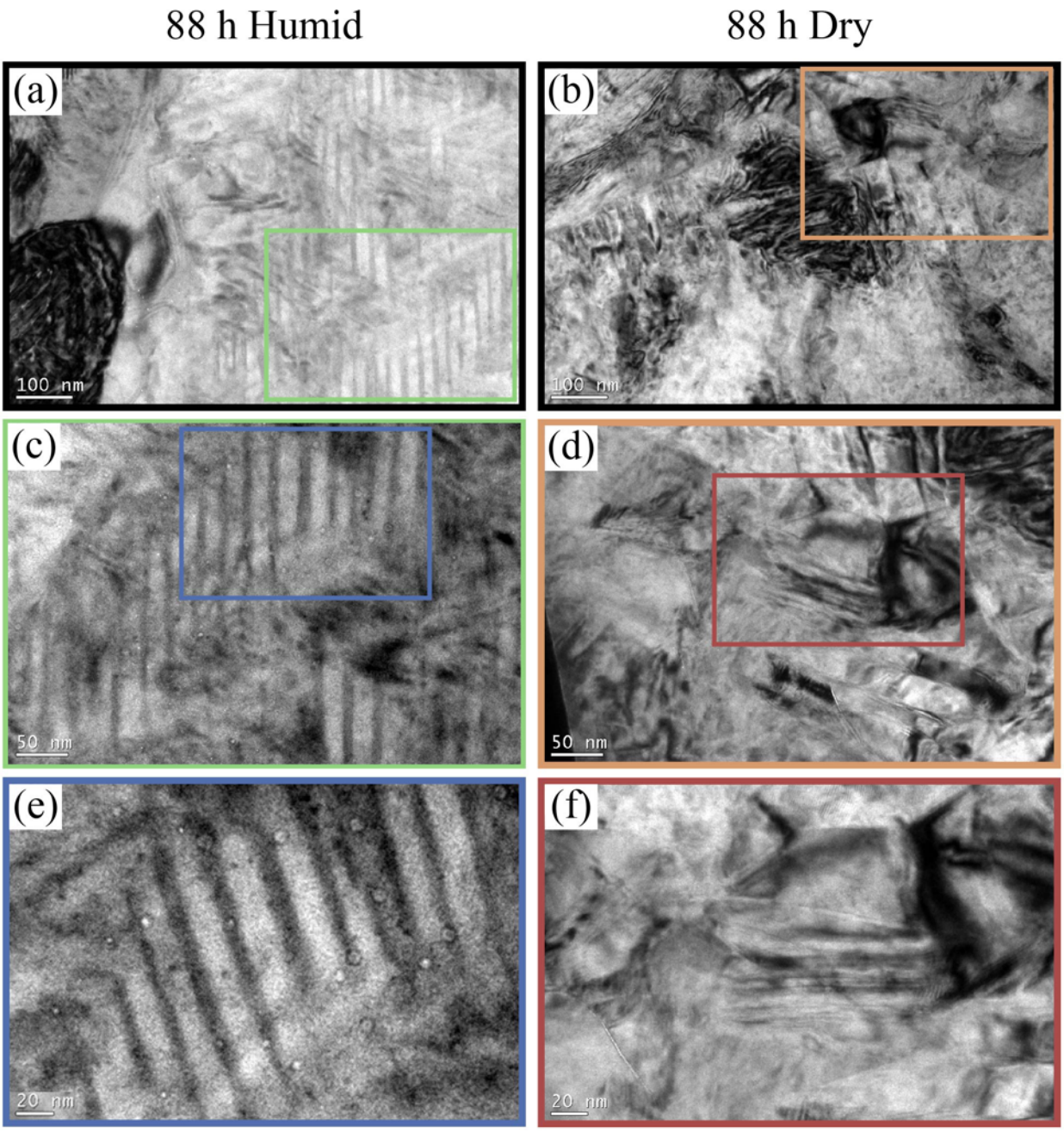


**Figure 5.2 Bright-field TEM images of the 15.2 K (88 h) aged samples showing the dry-aged sample in (a), (c), and (e) and the humid aged-sample in (b), (d), and (f). The higher magnification regions of (c), (e), (d), and (f) are indicated by the rectangles in (a), (c), (b), and (d), respectively.**

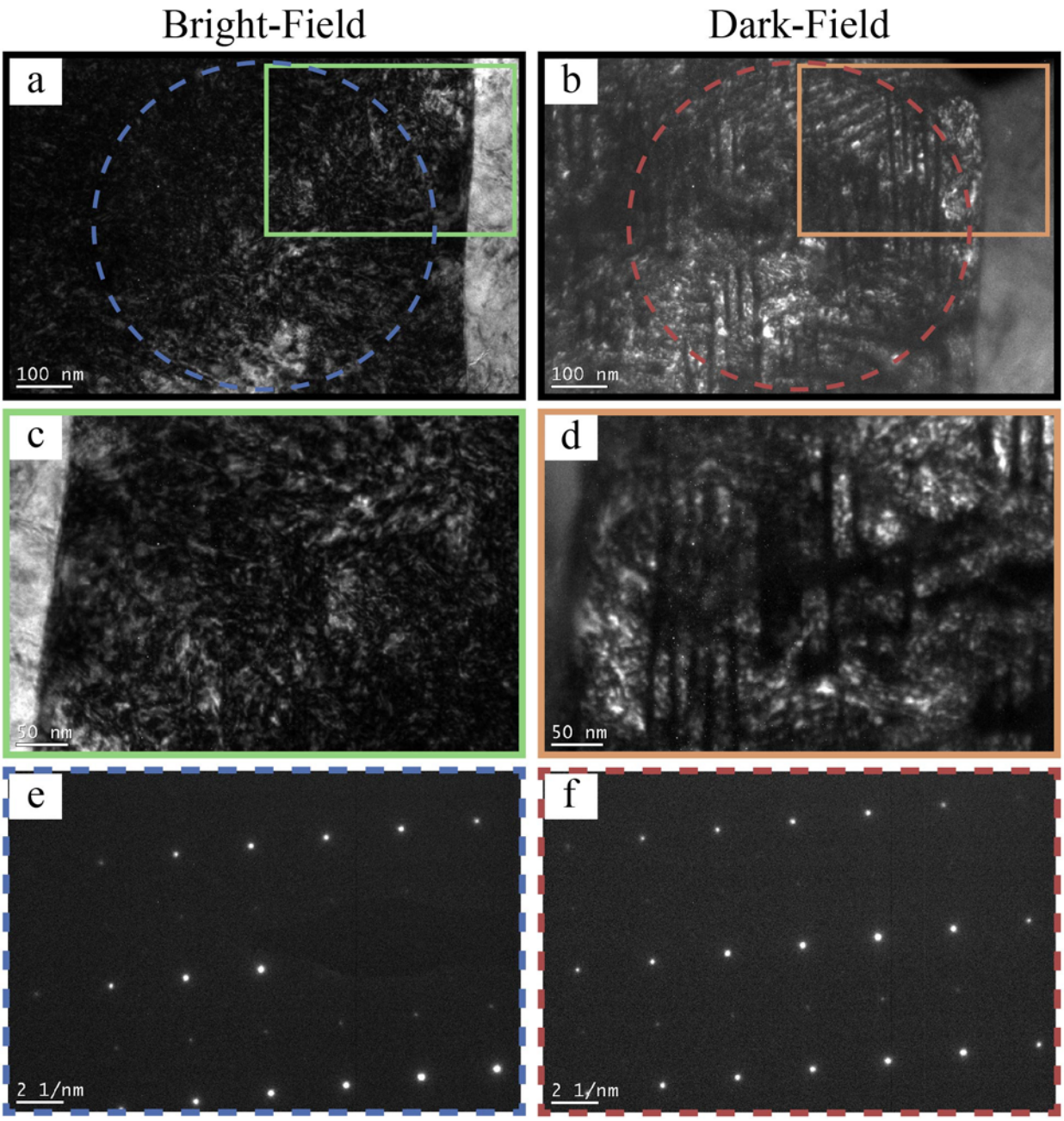


**Figure 5.3 Bright-field and dark-field TEM images of the 15.2 K (88 h) humid-aged samples showing bright field images in (a) and (c), dark-field images in (b) and (d), and SAD patterns in (e)—with the beam blocker—and (f)—without the beam blocker. The higher magnification regions of (c) and (d) are indicated by the rectangles in (a) and (b), respectively.**

### 5.3.2 15.9 (140 h) Aging

Figure 5.4 shows HAADF STEM images of the 15.9 K (140 h) dry and humid-aged samples. As in the case of the 15.2 K (88 h) aged samples, there is evidence of chemically-modulating domains in both environments as indicated by the alternating changes of contrast. However, the domain sizes of the 15.9 K (140 h) humid-aged sample are larger overall than that of the 15.9 K (140 h) dry-aged sample. For the 15.9 K (140 h) humid-aged sample, the majority of the domains range from 22 to 29 nm, while for the corresponding dry-aged sample the domains are 9-14 nm. This matches the anticipated result of having the domains be larger in a humid environment with the same amount of aging. Furthermore, there are more domains present in the humid 15.9 K (140 h) sample than that found in the 15.9 K (140 h) dry sample. In the case of the 15.9 K (140 h) dry sample, there is only one grain that consists of chemically modulating domains—as shown in Fig.5.4 (a). In a different region of the same sample, there is no evidence of any domains as shown in Fig. 5.4 (c). However, for the 15.9 K (140 h) humid sample, the entire region in Fig. 5.4 (b) consists of chemically modulating domains. The fact that there are larger and more domains overall for the 15.9 K (140 h) humid sample is evidence for acceleration of the aging process in a humid-aging environment compared to that of a dry one.

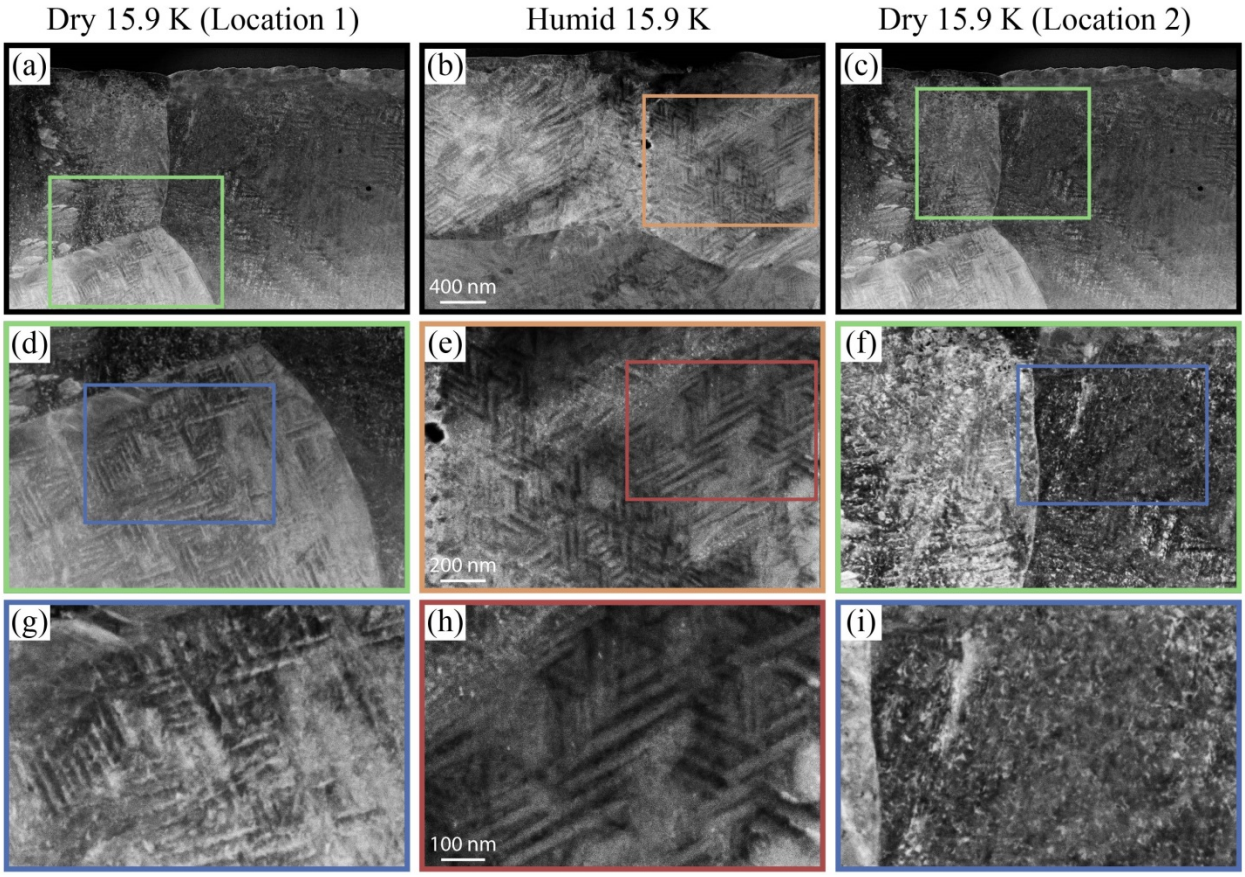


**Figure 5.4 HAADF STEM images of the 15.9 K (140 h) aged samples showing location one of the dry-aged sample in (a), (d), and (g); the humid-aged sample in (b), (e), and (h); and location two of the dry-aged sample in (c), (f), and (i).**

Figure 5.5 shows bright-field and dark-field images of the 15.9 K (140 h) dry- and humid-aged samples. The bright-field images of Fig. 5.5 (c) and (g) suggest the presence of the modulated structure for the humid aged sample, which is further supported by the complementary dark-field images of Fig. 5.5 (d) and (h). The SAD pattern of Fig. 5.6 (e) was taken along the <111> zone axis, while the SAD pattern of Fig. 5.6 (f) was taken along the <101> zone axis. Superimposed on the SAD patterns of Fig. 5.6 (e) and (f) are the simulated SAD tetragonal patterns. The simulated SAD tetragonal pattern matches the SAD pattern well for the 15.9 K (140 h) humid sample. Furthermore, the presence of the (112) reflections in the SAD pattern indicates the presence of the tetragonal phase in this area as found in earlier work

[61]. Therefore, the combination of a well-matched simulated SAD pattern and the presence of the (112) reflections, indicates that this SAD pattern is showing the modulated structure suggested in the bright- and dark-field images.

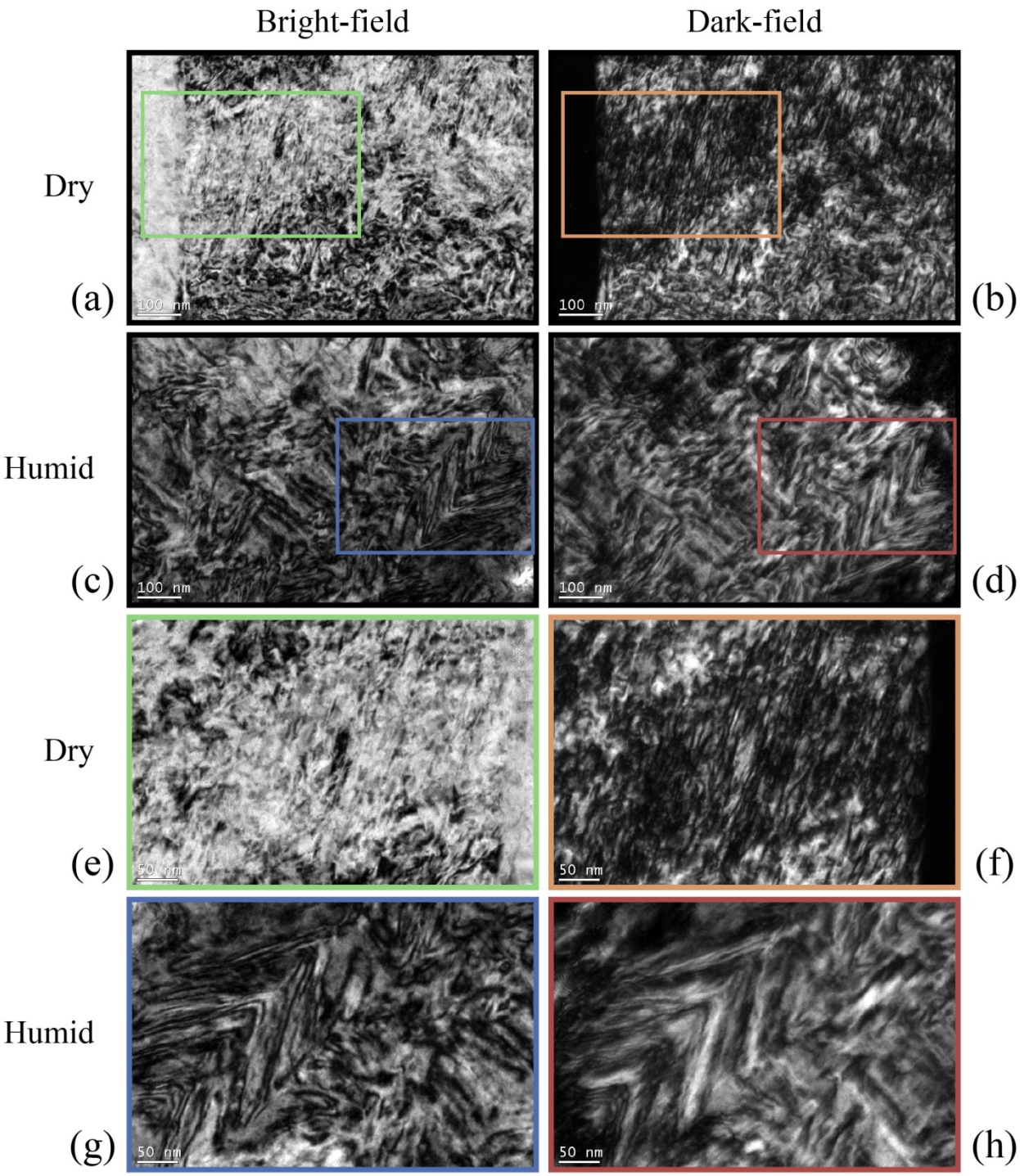

**Figure 5.5 The 15.9 K (140 h) aged samples showing bright-field images in (a), (c), (e), and (g) and dark-field images in (b), (d), (f), and (h).**

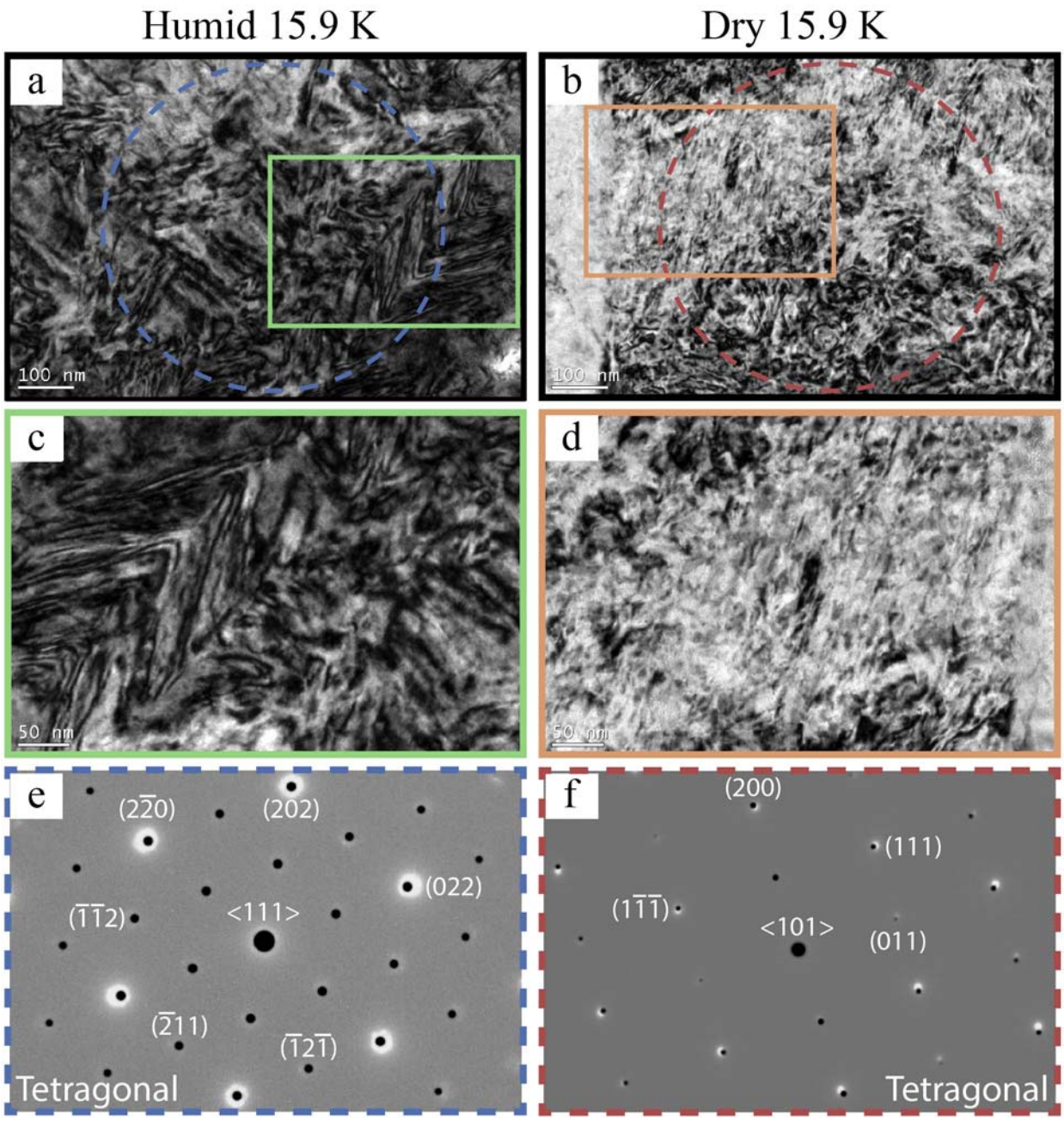


**Figure 5.6 The 15.9 K (140 h)-aged samples showing the humid-aged images in (a) and (c), dry-aged images in (b) and (d), SAD pattern in (e) from (a) and (c) with the superimposed tetragonal pattern, and the SAD pattern in (f) from (b) and (d) with the superimposed tetragonal pattern.**

### 5.3.3 16.7 (224 h) Aging

Figure 5.7 shows HAADF STEM images of the 16.7 K (224 h) dry- and humid-aged samples. In both the dry-and humid-aged samples there is evidence of chemically-modulating domains as indicated by the alternating changes of contrast. However, the domains in the dry-aged sample are of the order of 30 nm while the domains in the humid-aged sample are of the order of 80 nm. Previous work has shown that larger tetragonal domains are more easily transformed into the monoclinic phase [35]. The formation of these larger domains in the humid-aged sample provides a reason for why there is more monoclinic phase detected in the humid-aged sample than the dry-aged sample.

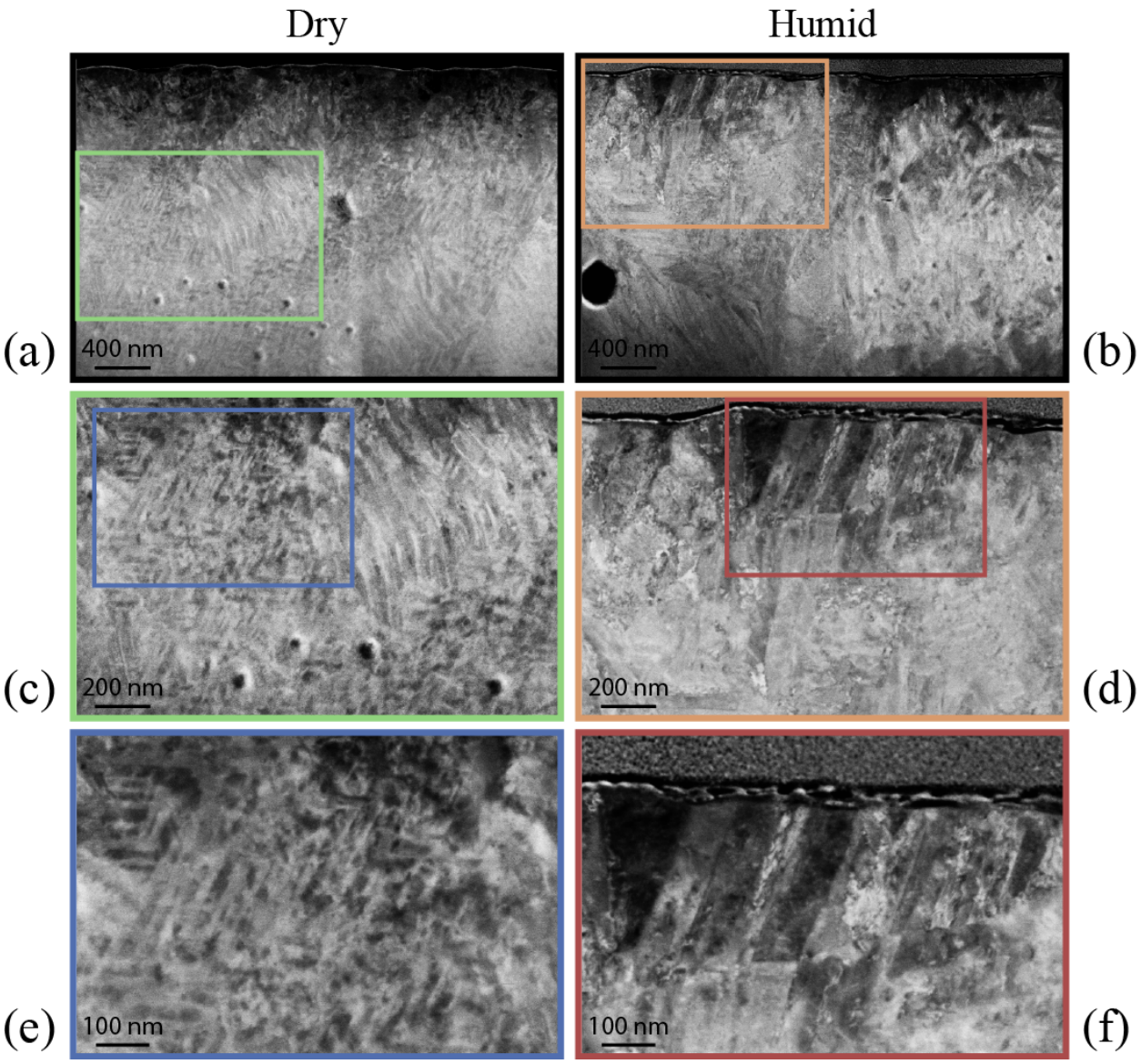


**Figure 5.7 HAADF STEM images of the 16.7 K (224 h) aged samples showing the dry-aged sample in (a), (c), and (e) and the humid-aged sample in (b), (d), and (f).**

Figure 5.8 shows different regions of the same 16.7 K (224 h) dry- and humid-aged samples with corresponding bright- and dark-field images. There are regions of contrast in Fig. 5 8 that correlate well between the dark-field and bright-field. For both the dry- and humid-aged samples, the dark-field images show dark-parallel bands that match the corresponding contrast in the bright-field images. The contrast in a dark-field image corresponds to differences in

orientation. The dry-aged sample shows a similar band structure although the dry-aged bands are less thick. These bands also do not reach or originate from the surface of the material—as in the case of the humid-aged sample—but rather are present 0.5 μm below the surface. As the monoclinic phase is supposed to nucleate from the surface, these bands in the dry-aged sample are not likely twins but more likely the chemically-modulated structure. The corresponding contrast in the bright- and dark-field images support this as the thickness is not likely changing significantly over a lateral distance of ~150 nm where these bands are present.

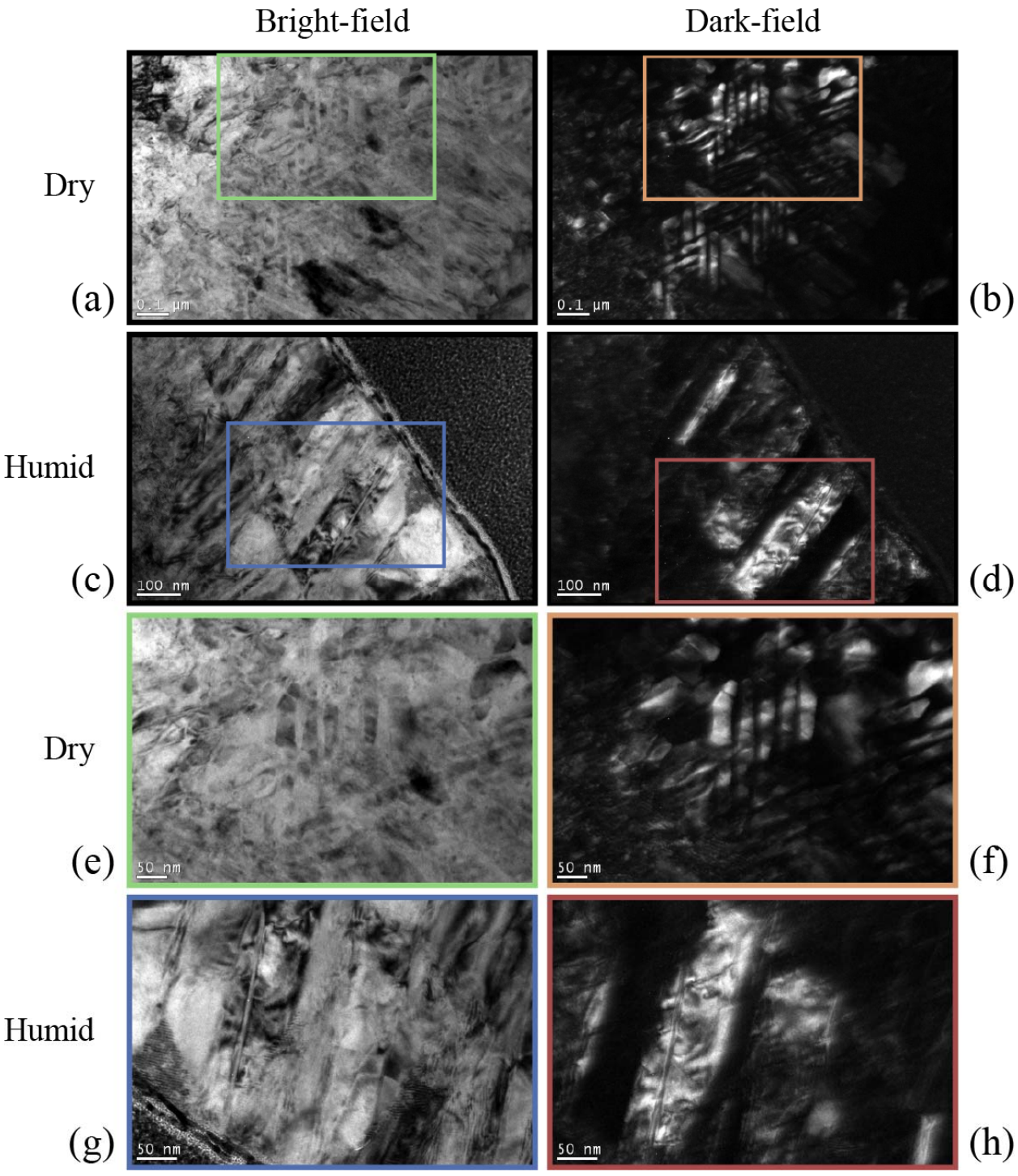


**Figure 5.8 TEM images of the 16.7 K (224 h) dry- and humid-aged samples showing bright-field images in (a), (c), (e), and (g) and dark-field images of the same region in (b), (d), (f), and (h). The higher magnification regions of (e), (f), (g), and (h) are indicated by the rectangles in (a), (b), (c), and (d), respectively.**

### 5.3.4 Chemistry of Domain Structures

Figure 5.9 shows STEM HAADF images of the as-received (AR), 16.7 K (224 h) dry-aged, and 16.7 K (224 h) humid-aged samples as well as the corresponding EDX line scans. The AR sample shows no evidence of ferroelastic domains but does show grains of approximately 300 nm in size. The HAADF images for the dry-aged sample indicate that there are domains present of the order of 30 nm with modulating composition. The humid-aged sample shows a similar chemical modulation except the domains in this sample are of the order of 70 nm. The darker contrast indicates a higher yttrium content as yttrium has a lower atomic mass than zirconium and darker regions correspond to lower mass in HAADF images. The EDX line scan agrees with this chemical correlation of the contrast in the HAADF images as the yttria content is highest in the darker regions of the image. The EDX line scans were composed of three separate lines averaged together in order to verify that the differences in yttria content were consistent along the length of the domain. The three separate lines were spaced 30 nm apart to ensure no overlap between lines for a probe diameter of 50 nm. However, along the length of each line EDX points were spaced 20 nm apart to establish continuity between points. Previous work found chemical modulation ranging between less than 4 to greater than 12 mol% along domains [61]. The yttria values obtained from this EDX analysis are consistent with that work ranging between averaged yttria values of 6.5 to 14.4 mol% for the 16.7 K (224 h) dry-aged sample. The 16.7 K (224 h) humid-aged sample has a similar yttria range with average values between 7.1 to 15.9 mol%. At the aging temperature of 1330 °C, the higher yttria values are at or approaching the cubic phase boundary at 15 mol% while the lower yttria values are approaching the tetragonal phase boundary at 5.5 mol%. In comparison, the AR sample shows no evidence of chemical modulation in yttria when the same EDX line scans are performed across a grain.

Instead, the yttria value shows only a 8% deviation from its average value of 9.38 ± 0.76—as compared with 24% for the dry-aged sample and 29% for the humid-aged sample.

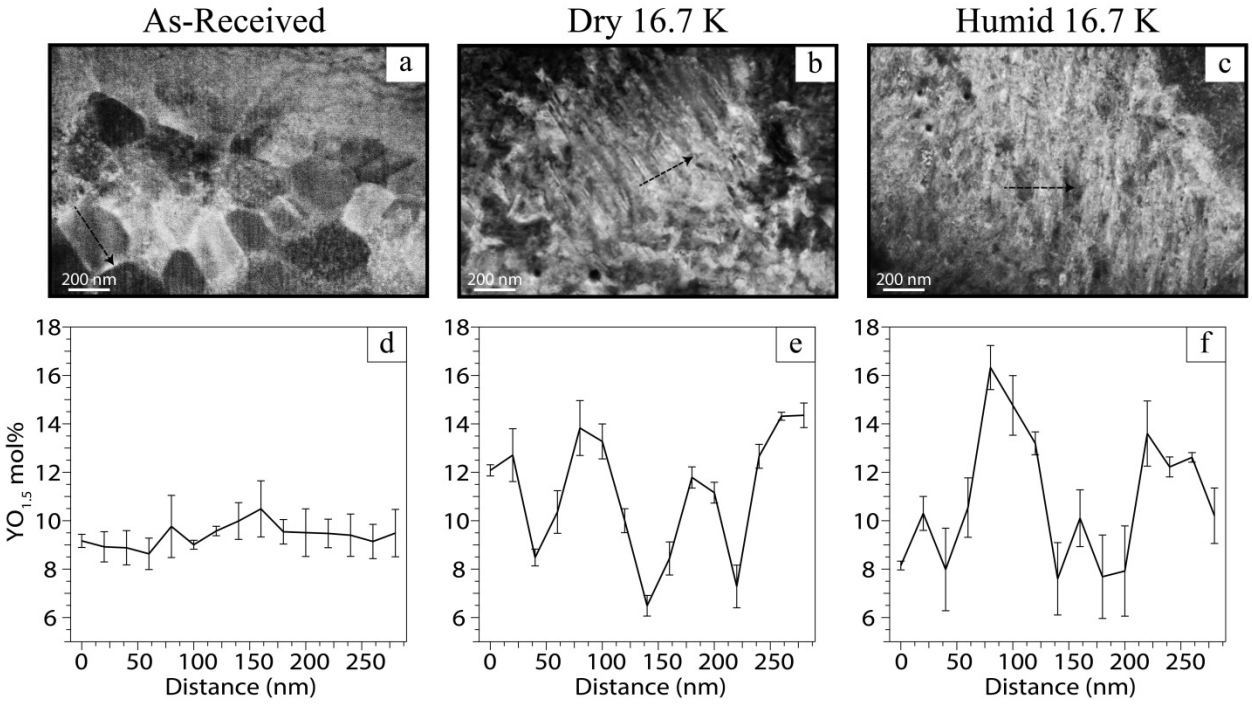


**Figure 5.9 The as-received, 16.7 K (224 h) dry-aged, and 16.7 K (224 h) humid-aged samples showing the STEM HAADF images in (a), (b), and (c) and the corresponding EDX line scans in (d), (e), and (f) across the dotted-lines shown in (a), (b) , and (c).**

### 5.3.5 Comparison of Domains for All Aging Data

Figure 5.10 shows the STEM HAADF images for all the dry- and humid-aged samples used in this study. A steady increase in the domain size can be seen within the grains selected for both environments as the aging increases from 15.2 K (88 h) to 16.7 K (224 h). At the same amount of aging time, the domains for the humid-aged sample are always bigger than that of the dry-aged sample.

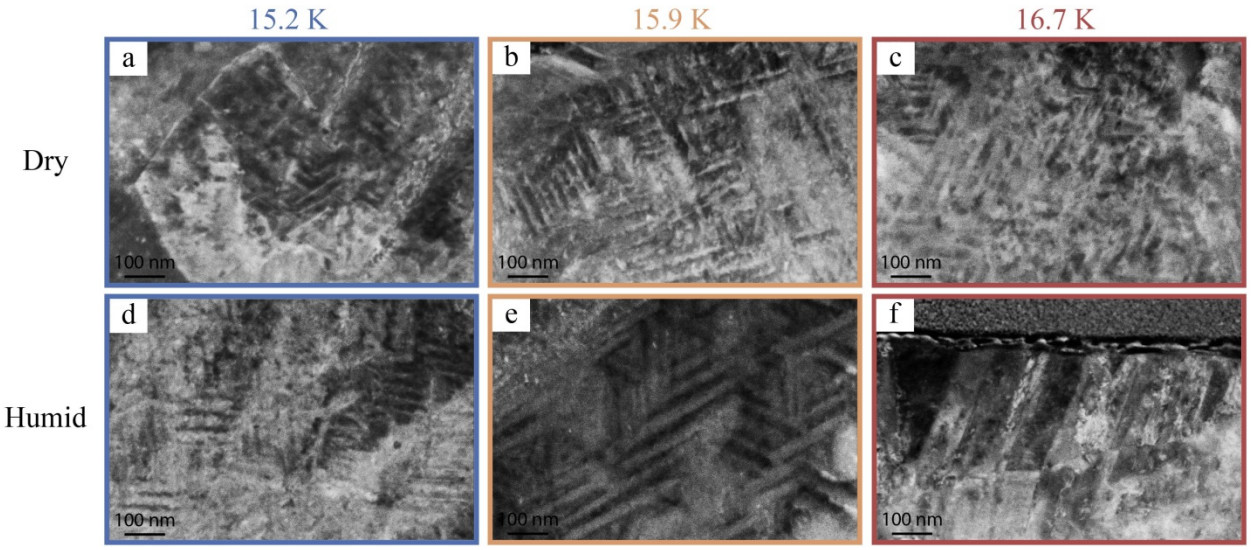


**Figure 5.10 STEM HAADF images showing the dry-aged samples in (a), (b), and (c) and the humid-aged samples in (d), (e), and (f). The aging times are: 15.2 K (88 h) for (a) and (d), 15.9 K (140 h) for (b) and (e), and 16.7 K (224 h) for (c) and (f).**

Figure 5.11 shows XPS spectra taken from the 10.9 K (6 h), 15.2 K (88 h), and 15.9 K (140 h) dry- and humid- aged samples. The area probed was a rectangle with dimensions of 300 um by 700 um on the surface of each sample. The spectra look different between the different aging environments for all the elemental peaks shown after 140 h of aging. The O 1 s signal shows a general shifting of the peaks to higher binding energies for the humid aged sample. This suggests the formation of hydroxyl groups in the humid aged sample although it can't be determined by a qualitative comparison whether there are more oxygen anions present. The Zr 3d line indicates that after 140 h of aging there is the formation of some Zr hydroxyl groups on the surface of the humid aged sample at the expense of zirconia. In agreement with the Zr results, the Y 3d spectra also shows the formation of hydroxyl groups. The Si 2p spectrum indicates that there are Si impurities in both samples but that they have been converted to silica. The humid-aged sample has much less intensity due to silica indicating that the silica volatilized away in this environment.

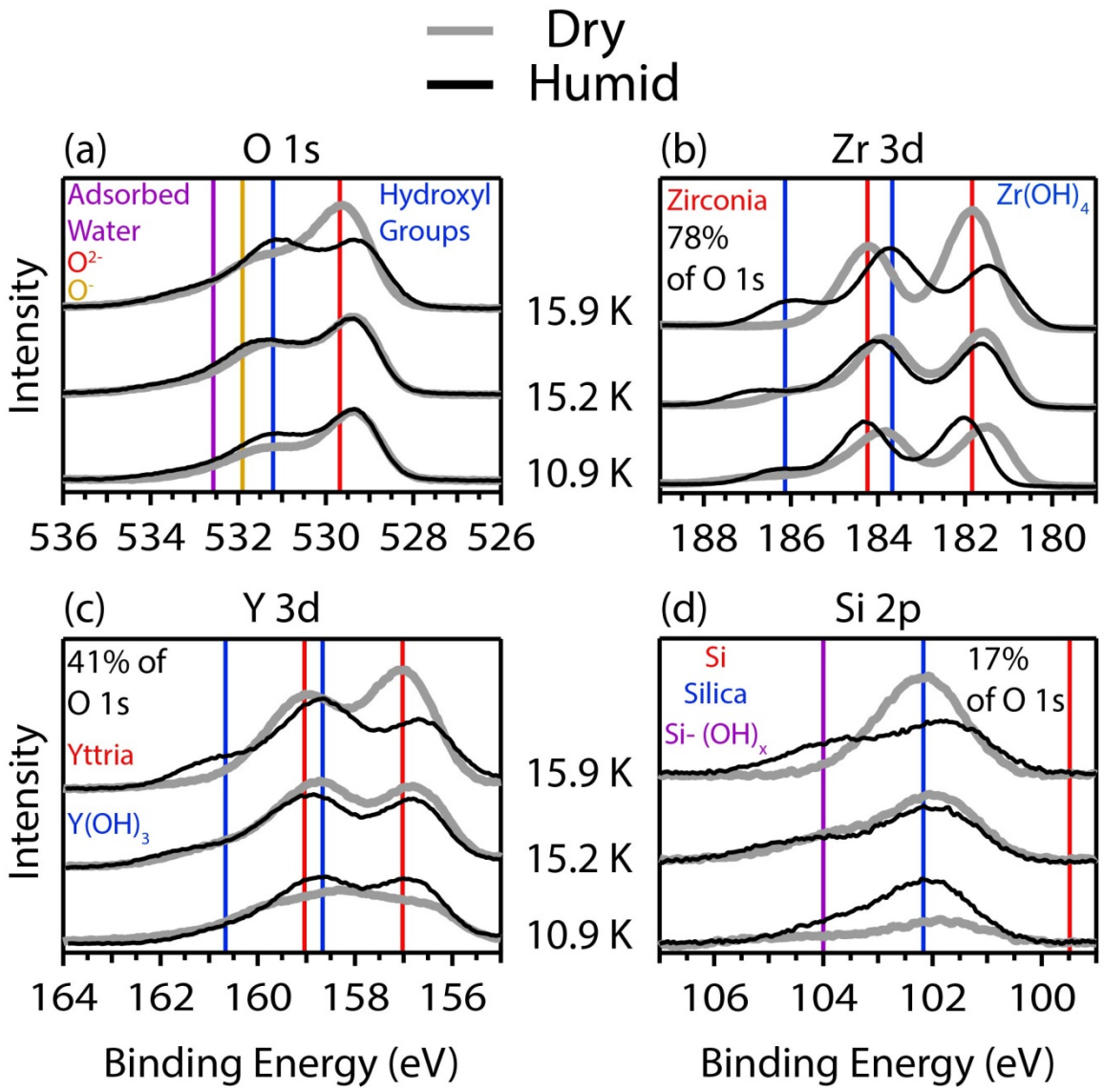


**Figure 5.11 XPS spectra of the 10.9 K (6 h), 15.2 K (88 h), and 15.9 K (140 h) dry- and humid-aged samples showing the O 1 s, Zr 3d, Y 3d, and Si 2p shells.**

## 5.4 Discussion

### 5.4.1 Destabilization Pathway

The detailed analysis of the microstructure provided here supports the previously proposed decomposition of the *t'* phase in APS 8YSZ coatings into chemically modulating domains by high temperature aging [60, 61]. The dry-aged samples show the formation and coarsening of yttria-rich and yttria-lean domains. A similar behavior also occurs for the humid-

aged samples, except that the coarsening of the domains occurs faster than that of the dry-aged samples. In terms of the formation of these domains relative to the surrounding microstructure, this particular APS microstructure is indicative of the destabilization pathway through coarsening of the modulated microstructure as proposed by Levi et al [61]. This is suggested because all of the lamellae for both environments have little difference in grain sizes between neighboring grains. Therefore, in the samples investigated there is no alternative pathway to destabilize the modulated microstructure as in the scenario of smaller equiaxed grains neighboring a larger grain. The destabilization of the *t'* phase in both environments then should be largely governed by the coarsening of the chemically modulating domains—although at a faster rate for the humid-aged samples.

### 5.4.2 Microstructure in Relation to LTD

The microstructure of the humid-aged samples indicates that resistance to water-induced transformation is not dictated by grain size. As was determined in the LTD investigation of the *t'* phase by Virkar et al. [35], the *t'* phase provides resistance to rapidly induced phase transformation by water vapor. The dependence of the tetragonal phase transformation on the domain size proposed by this earlier work is also likely playing out in the HTD of the *t'* phase. There needs to be a certain amount and size of the domains present in order for transformation of monoclinic phase to occur. The phase analysis from the quantitative XRD, showed a small amount of monoclinic phase present up to 15.2 K (88 h) aging for both environments. The monoclinic phase does not increase significantly up to this point and is likely a remnant of the rapidly cooling conditions that occur during the spraying of the APS coatings [61]. At this point in the aging, domains in the humid-aged sample do not appear in all the grains of the lamella as they do in the case of the two subsequent aging times. Furthermore, the domains that do appear

at 15.2 K (88 h) of humid aging are smaller overall compared to the two subsequent aging times. As the humid aging progresses from 15.2 K (88 h), there is a rapid increase in the amount of monoclinic phase formed in the next two aging times (at least 64%). There is also a rapid increase in the domain size from 15.2 K (88 h) aging to subsequent aging times (at least 76%) and the largest increase in domain size occurs with the largest increase in the monoclinic phase from 15.9 to 16.7 K ( 140 to 224 h) of aging. The dry-aged samples also follow a similar trend. The lack of an increase in the monoclinic phase through 16.7 K (224 h) in the dry environment is accompanied by a much smaller increase in the domain size—(329% vs. 429%)—from 15.2 to 16.7 K (88 to 224 h). Therefore, there is strong evidence for a larger domain size allowing for an easier transformation to the monoclinic phase.

### 5.4.3 Role of Impurities in Humid Aging

Impurities have been known to influence the aging process of YSZ for both LTD and at high temperatures. Earlier work by Heuer et al. showed that impurities present in commercially available 8YSZ influence the cation diffusion during annealing [88]. TEM imaging indicated that after the heat treatment an amorphous, Si phase was continuous along grain boundaries and was thought to be responsible for precipitating a yttria-enriched region, free of precipitates in the nearby region. Levi et al. also detected glassy Si pockets in the grain boundaries of APS 8YSZ but did not explicitly incorporate the role of these glassy phases in their aging mechanism [61]. Yttrium and other cations doped into YSZ have been found to segregate along grain boundaries after high temperature annealing [88, 95]. These authors have proposed that the transformation of the tetragonal phase originates at the grain boundaries and then causes transformations to occur in the grain interiors. Glassy phases that form at the grain boundaries due to the presence

of impurities have enhanced the diffusion of yttrium out of the parent phase and hasten the decomposition of the *t'* phase in dry environments [96].

What is less clear, is how the impurities present in APS 8YSZ will behave in the presence of increased water vapor. There is the possibility that amorphous silica impurities can become hydrated and further enhance the yttrium diffusion relative to a dry environment. However, the work that has been done on the behavior of Si and other impurities in YSZ exposed to LTD suggests a different role. No influence was found on the LTD behavior by varying the Si content in YSZ from 56 to 760 ppm [67]. Recent work that doped 3YSZ with lanthana and alumina found a segregation of these dopants to the grain boundaries—along with yttrium—when exposed to LTD conditions [97]. However, the dopants actually delayed the phase transformation to the monoclinic phase and reduced the total amount of monoclinic phase formed relative to the undoped material. As this work is the first known to the authors to investigate the role of humidity on the high temperature aging of 8YSZ, no other studies have been identified in showing the influence of impurities on yttrium diffusion in humid environments at temperatures relevant to gas turbines. However, silica is known to volatilize above 1300 °C in environments with a partial pressure of 0.5 bar $H_2O$—conditions similar to those used in the humid-aging performed here [89]. This implies that the amount of Si impurities in the APS 8YSZ coatings should be less in the humid-aged samples than those of the dry-aged samples due to volatilization. The images and EDX of the lamella support this, as little evidence of a glassy phase was seen at grain boundaries of the humid-aged samples. Although there are Si impurities in the APS 8YSZ, the fact that enhanced domain coarsening occurs in grains devoid of impurities near their boundaries in humid environments implies a less influential role. Therefore, the

dominant mechanism by which the domains coarsen in the humid-aged samples is not likely due to the role of Si or other impurities.

### 5.4.4 Proton Migration in Relation to Domain Coarsening

While there are certain similarities to the LTD, the HTD must have a distinct mechanism in regards to how domains coarsen. While it has already been mentioned that the *t'* phase has superior resistance to LTD than the tetragonal phase due to differences in domain size [35], it is clear from this microstructural investigation that the commonly invoked stress corrosion mechanism [66, 68] of LTD cannot explain the way in which domains coarsen for HTD. In the stress corrosion mechanism, the monoclinic phase transformation brought about by water vapor generates stress in the neighboring grains due to the volume expansion. The stress can lead to cracking and can expose more of the material interior to the water vapor thereby repeating the process. In the images shown of the humid-aged samples, there is little evidence of extensive cracking in the vicinity is which large domains are present. While it is certainly expected that the volume expansion of the monoclinic grains will cause sufficient stresses to induce cracking, the coarsening of the domains up to the point in which they induce the monoclinic phase transformation does not seem directly related to the formation of cracks.

The role of water vapor in causing the domains to coarsen faster at higher temperatures is not clear. The proposed mechanism is that the enhanced destabilization of the *t'* phase during HTD is due to the incorporation of protons and oxygen anions into YSZ. Recent computational work showed that the energy associated with proton incorporation into YSZ is favorable and that the migration energies are similar to other proton conductors [72]. A separate investigation by the same group concluded that proton migration is more favorable along grain boundaries than in the lattice [73]. Protons can then travel along the grain boundaries of YSZ during HTD and be

incorporated into local grains. The incubation time observed prior to the rapid increase of the monoclinic phase at 15.9 K (140 h) for the humid-aging may be a result of the slow accumulation of protons and anions into the lattice. Once the protons are incorporated into the lattice, it is most favorable for the protons to "hop" between neighboring oxygen atoms [72]. As a hydroxyl group is known to be smaller than an oxygen anion, the incorporation of protons would reduce the size of the oxygen anions as they travel through the lattice [98]. This size reduction would help drive the tetragonal phase to its equilibrium lattice position and in the process cause an increased rate of domain coarsening. Therefore, this would be a means for the *t'* phase to be depleted of yttrium faster through coarsening of the modulated domains within the lattice. The preliminary XPS work performed here indicates the presence of hydroxyl groups on the surface of the humid-aged samples while showing the absence of these groups for the dry-aged samples. The formation of the hydroxyl groups at the same time at which the monoclinic phase starts to increase significantly in the humid-aged samples suggests that protons are being incorporated into the YSZ and enhancing the destabilization of the *t'* phase by this increased coarsening mechanism.

## 5.5 Conclusion

A microstructural analysis was conducted to complement a macro-scale phase analysis of the high temperature, dry- and humid-aging of APS 8YSZ shown in the previous chapter. The FIB was employed to make lamellae samples for each environment from three sets of aging times. These aging times were chosen to track the microstructural changes before, during, and after significant changes in the phase content between the two environments. The lamellas were analyzed using a HAADF STEM detector in the SEM and a conventional TEM. The HAADF images and STEM EDX indicate the presence of chemically modulated domains in APS 8YSZ after high temperature aging in both a dry and humid environment. Dark-field imaging and SAD

patterns in the TEM confirm a modulated microstructure in both environments. This complementary analysis has determined that the ferroelastic domains coarsen faster and are more numerous in a humid-aging environment than that of a dry one. The microstructural evidence presented here helps explain why the monoclinic phase started to increase more rapidly for the humid-aging environment than for that of the dry one as shown by the XRD and Raman spectroscopy results. This work supports the theory that a larger domain size will lead to an earlier transition of the tetragonal phase to the monoclinic. The microstructural insights provided in this chapter can help determine an optimal initial microstructure for APS 8YSZ to resist the enhanced destabilization of the *t'* phase when this coating is used in gas turbine environments with high water vapor.

# 6 Chapter 6: Summary and Future Work

## 6.1 Summary

The degradation of hot section gas turbine materials for propulsion and power generation has been investigated in alternative environments. For propulsion applications, alloy coatings used in shipboard turbines were evaluated in two combustion environments using a custom built experimental apparatus known as the LVBR. The first combustion environment was established by combusting a traditional F76 fuel while the second was caused by combusting a Blend fuel consisting of a 50/50 mixture of the F76 fuel and a hydroprocessed renewable diesel fuel derived from algae. After exposure to these two different environments, the same phases and similar microstructures developed but there are differences in the rates of the alloy evolution between the two combustion environments. These differences were most notable in the NiAl and Pt-modified NiAl coatings. Within some regions of the alloy coatings for the Blend test, thick scales have developed that contain sulfides and residual coating. EDS line profiles beneath these scales indicate a much more rapid depletion of Al as compared with regions of the coating from the F76 test. To explain the enhanced depletion in the Blend test, it was proposed that the basicity at the scale/deposit was increased due to changes in the combustion characteristics of the fuel. The increased basicity would dissolve the scale faster due to being more soluble in the molten deposit. These results highlight that subtle differences in the fuel can alter the combustion environment and can cause differences in the degradation characteristics of the hot section components that are material dependent. Therefore, it is important to fully understand the material evolution of these coatings in different combustion environments prior to implementation, as the premature failure of these coatings in-service would be catastrophic for the propulsion application.

Alternative environments in the form of increased humidity were also shown to influence the degradation of the ceramic coatings commonly used to protect the hot section components of power generation turbines. 8YSZ APS coatings were aged at temperatures relevant to gas turbines in dry and humid environments. The material evolution of these exposed coatings was characterized by XRD and Raman spectroscopy. For up to 88 h of aging, there was an incubation period where only minute differences in the phase evolution could be observed between the aging environments. After this initial incubation period, XRD showed that the parent *t'* phase of the APS coatings transformed more rapidly to the tetragonal phase—and then to the monoclinic phase—in a humid environment than for that of a dry one. In a much smaller probing volume, Raman spectroscopy confirmed these results and also showed that yttrium was leaving the parent phase faster in the humid environment after the incubation period had elapsed. The enhanced destabilization was proposed to occur due to protons being incorporated into the 8YSZ and reducing the size of oxygen sites in the lattice by effectively becoming hydroxyl groups. This size change in the oxygen atoms would allow the lattice to distort faster to the equilibrium phase and overcome the coherency strains binding it to the adjoining cubic phase.

The incubation period in the aging of the APS coatings prior to the observed differences between the two environments can not be understated. Although no publication could be found of a similar type of experiment, undoubtedly a previous investigation into the role of humidity in the high temperature aging of APS was attempted. However, the use of lower temperatures or shorter timespans in the aging likely showed no differences in the phase evolution for a humid environment and the role of water vapor on the enhanced destabilization of APS coatings was missed.

In order to verify that water vapor was influencing the structure of the parent phase in APS coatings, a detailed investigation into the evolution of the microstructure in the different aging environments was performed. By the use of a FIB, lamella samples were extracted from the bulk APS coatings exposed in both environments to be used in STEM and TEM analysis. HAADF images in the STEM revealed the ferroelastic domain structure formed in both environments. The chemical modulation among neighboring domains of samples from both environments was verified by EDS and SAD patterns in the TEM confirmed the formation of the equilibrium phases. The analysis confirmed that for a given aging time, the ferroelastic domains coarsen faster in a high temperature humid environment than compared to that of a dry environment. A faster coarsening rate for the humid samples would mean that the tetragonal domains would reach the critical size necessary to transform to the monoclinic phase faster—helping to explain the more rapid appearance of the monoclinic phase in the humid environment. The observed enhanced coarsening rate also gave credence to the proposed mechanism that a water vapor derived species is allowing the parent *t'* phase to move towards the tetragonal phase faster and overcome the strains coherency binding them to the neighboring cubic domains. This microstructural analysis proved critical in better understanding how the water vapor was altering the domains and allowing for an enhanced destabilization of the parent phase in the APS coatings. Revealing the expedited domain coarsening in the humid environment provides groundwork for future work in establishing a connection between the domains and some water-derived species.

## 6.2 Future Work

Based on the findings presented in this dissertation in relation to the degradation of hot section materials in alternative gas turbine environments, some future work can be suggested to

better verify or reject the proposed mechanisms. In regards to the metal alloys used in shipboard propulsion, the following is suggested:

1. In order to verify or reject the connection between increased basicity at the scale/deposit interface with increased depletion in the alloy coating, an experimental set-up similar to that done by Jose et al. [47] should be assembled and used to test the NiAl and Pt-modified NiAl coatings. Here the basicity at the scale/deposit interface can be finely controlled by inclusion of more $Na_2O$ into the molten deposit. The corresponding solubility of the scale in the molten deposit can then be measured for each change in basicity. The resulting exposed samples can then be prepared for EDX analysis to determine the extent of aluminum depletion within the alloy coatings for each one. For a range of basicity's, a trend in the Al depletion within the alloy coatings should be apparent, and the proposed connection between basicity and Al depletion within the alloy can be verified or rejected.

In regards to the APS coatings used in power generation, the following is suggested:

1. In order to explain the incubation period during which the dry and humid aging environments appear to give similar phase evolution, it is proposed that the ferroelastic domains be altered to either change the strain state or to change the size of the domains at the interfaces between the tetragonal and cubic phases. The current proposed mechanism assumes that no changes are observed between the different environments during the incubation period because the coherency strains hinder the coarsening of the domains up to this point. In order to alter the strain state and/or change the domain size, it is suggested to mechanically grind the samples—but not polish them—to induce domain switching within the APS coatings prior to exposing them to a humid environment. If

more/less monoclinic phase transformation is observed for a given amount of aging time than without grinding, this would better link the strain/size of the domains to the cause of the observed incubation time.

2. To better determine how water derived species is incorporated into APS coatings, it is suggested to run the humid aging exposure with deuterated water as opposed to DI water. The use of deuterium would allow the different derived water species—protons, hydroxyl groups, oxygen anions—to be isotopically labeled and tracked in the APS post exposure. The current proposed mechanism suggests protons are migrating through the APS citing evidence from literature, but if the isotope markers could be tracked via a SIMS analysis post exposure then the proposition of proton incorporation into APS could be either verified or rejected.
3. One limitation of the current aging analysis is that all the characterization techniques were done at ambient temperature. This makes it difficult to interpret results as it is thought that the lattice parameters of the *t'* phase are different as a consequence of performing XRD after the sample has cooled down to ambient temperature and the associated coherency strains have been introduced into the sample. So at the temperature that the sample is being aged there is expected to be two sets of lattice parameters that correspond to each of the equilibrium phases at the aging temperature. Therefore, it is advantageous to perform the XRD *in-situ* at the aging temperature and there is certainly equipment at UCI to perform an elevated temperature XRD experiment. However, it is not configured to run water vapor so that is a limitation, but insights may still be gained by performing high temperature XRD on samples that were already exposed in a dry and humid environment. For example, perform high temperature XRD on samples after they

have been aged for 140 h in a dry or humid environment. This would allow for a comparison of the lattice parameters at ambient and elevated temperatures for both environments.

## References


[1] D.R. Clarke, M. Oechsner, N.P. Padture. Thermal-barrier coatings for more efficient gas-turbine engines, Mrs Bulletin 37 (2012) 891-902.

[2] C.T. Sims, N.S. Stoloff, W.C. Hagel. Superalloys II, Wiley, New York, 1987.

[3] R.W.A., B. M. White, and P. Burke. Conditions in advanced turbines for IGCC power plantswith carbon capture, Proceedings of the ASME Turbo Expo 2013 TE2013 (2013).

[4] M.H. Sullivan, D.R. Mumm. Vapor-Phase-Mediated Phenomena Associated with High Temperature, High Water Content Oxidation of MCrAlX Bond Coats, Oxidation of Metals 82 (2014) 1-20.

[5] M.T. MacKinnon, J.D. Shaw, M. Quinones. Combustion Assessment of a 50% Algae-Based HRD76 Fuel and 50% Conventional F76 Military Diesel Fuel Blend, Journal of Engineering for Gas Turbines and Power-Transactions of the Asme 134 (2012) 8.

[6] N.P. Padture, M. Gell, E.H. Jordan. Materials science - Thermal barrier coatings for gas-turbine engine apptications, Science 296 (2002) 280-284.

[7] B. Gleeson, N. Mu, S. Hayashi. Compositional factors affecting the establishment and maintenance of $Al_2O_3$ scales on Ni-Al-Pt systems, Journal of Materials Science 44 (2009) 1704-1710.

[8] D.J. Young. High temperature oxidation and corrosion of metals, Elsevier, Amsterdam; Boston; London, 2008.

[9] T.E. Strangman. Thermal barrier coatings for turbine airfoils, Thin Solid Films 127 (1985) 93-105.

[10] A.G. Evans, D.R. Mumm, J.W. Hutchinson, G.H. Meier, F.S. Pettit. Mechanisms controlling the durability of thermal barrier coatings, Progress in Materials Science 46 (2001) 505-553.

[11] H.B.C. Allison, L.A. Hawkins. Cahrising : A protective treatment for metals, General Electric Review 17 (1914) 947-951.

[12] B.M. Warnes, D.C. Punola. Clean diffusion coatings by chemical vapor deposition, Surface & Coatings Technology 94-5 (1997) 1-6.

[13] A.B. Smith, A. Kempster, J. Smith. Vapour aluminide coating of internal cooling channels, in turbine blades and vanes, Surface & Coatings Technology 120 (1999) 112-117.

[14] G.W. Goward. Progress in coatings for gas turbine airfoils, Surface & Coatings Technology 108 (1998) 73-79.

[15] F.S. Pettit. Oxidation Mechanisms For Nickel-Aluminum Alloys At Temperatures Between 900 Degrees And 1300 Degrees C, Transactions of the Metallurgical Society of Aime 239 (1967) 1296-&.

[16] J.D. Oberstar, B.G. Streetman, J.E. Baker, P. Williams. Iron and Chromium Redistribution in Semi-Insulating InP, Journal of the Electrochemical Society 128 (1981) 1814-1817.

[17] C. Jiang, D.J. Sordelet, B. Gleeson. Site preference of ternary alloying elements in $Ni_3Al$: A first-principles study, Acta Materialia 54 (2006) 1147-1154.

[18] B.A. Pint. Experimental observations in support of the dynamic-segregation theory to explain the reactive-element effect, Oxidation of Metals 45 (1996) 1-37.

[19] U. Schulz, M. Menzebach, C. Leyens, Y.Q. Yang. Influence of substrate material on oxidation behavior and cyclic lifetime of EB-PVD TBC systems, Surface & Coatings Technology 146 (2001) 117-123.

[20] C. Mennicke, M.Y. He, D.R. Clarke, J.S. Smith. The role of secondary oxide inclusions ("pegs") on the spalling resistance of oxide films, Acta Materialia 48 (2000) 2941-2949.

[21] E.A. Jarvis, E.A. Carter. Importance of open-shell effects in adhesion at metal-ceramic interfaces, Physical Review B 66 (2002) 4.

[22] E.A.A. Jarvis, E.A. Carter. An atomic perspective of a doped metal-oxide interface, Journal of Physical Chemistry B 106 (2002) 7995-8004.

[23] K.M. Carling, E.A. Carter. Effects of segregating elements on the adhesive strength and structure of the alpha-$Al_2O_3$/beta-NiAl interface, Acta Materialia 55 (2007) 2791-2803.

[24] K.H. Stern. Metallurgical and ceramic protective coatings, Chapman & Hall, London; New York, 1996.

[25] C. Mercer, J.R. Williams, D.R. Clarke, A.G. Evans. On a ferroelastic mechanism governing the toughness of metastable tetragonal-prime (t ') yttria-stabilized zirconia, Proceedings of the Royal Society a-Mathematical Physical and Engineering Sciences 463 (2007) 1393-1408.

[26] D. Apelian, M. Paliwal, R.W. Smith, W.F. Schilling. Melting and solidification in plasma spray deposition-phenomenological review, International Metals Reviews 28 (1983) 271-294.

[27] C.H. Hsueh, P.F. Becher, E.R. Fuller, Jr., S.A. Langer, W.C. Carter. Surface-roughness induced residual stresses in thermal barrier coatings: computer simulations. Materials Science Forum, vol. 308-311. Trans Tech Publications, 1999. pp. 442-449.
[28] K.L. Luthra, D.A. Shores. Mechanism of $Na_2SO_4$ Induced Corrosion at 600°–900°C, Journal of the Electrochemical Society 127 (1980) 2202-2210.
[29] N. Otsuka, R.A. Rapp. Hot Corrosion of Preoxidized Ni by a Thin Fused $Na_2SO_4$ Film at 900°C, Journal of the Electrochemical Society 137 (1990) 46-52.
[30] J.A. Goebel, F.S. Pettit. $Na_2SO_4$-induced accelerated oxidation (hot corrosion) of nickel, Metallurgical Transactions 1 (1970) 1943-&.
[31] K.L. Luthra. Kinetics of the Low Temperature Hot Corrosion of Co-Cr-Al Alloys, Journal of the Electrochemical Society 132 (1985) 1293-1298.
[32] L.Q. Shi, Y.S. Zhang, S.T. Shih. The low temperature hot corrosion of iron and iron-aluminum alloys, Corrosion Science 33 (1992) 1427-1438.
[33] R.A. Rapp, Y.S. Zhang. Hot Corrosion Of Materials - Fundamental-Studies, Jom-Journal of the Minerals Metals & Materials Society 46 (1994) 47-55.
[34] P.M. Kelly, L.R.F. Rose. The martensitic transformation in ceramics - its role in transformation toughening, Progress in Materials Science 47 (2002) 463-557.
[35] J.F. Jue, J. Chen, A.V. Virkar. Low-temperature aging of t'-zirconia: the role of microstructure on phase stability, Journal of the American Ceramic Society 74 (1991) 1811-1820.
[36] J.A. Krogstad, S. Kramer, D.M. Lipkin, C.A. Johnson, D.R.G. Mitchell, J.M. Cairney, C.G. Levi. Phase Stability of t '-Zirconia-Based Thermal Barrier Coatings: Mechanistic Insights, Journal of the American Ceramic Society 94 (2011) S168-S177.
[37] J.R. Ferraro, K. Nakamoto, C.W. Brown. Introductory Raman spectroscopy, (2003).
[38] V. Lughi, D.R. Clarke. Transformation of electron-ream physical vapor-deposited 8 wt% yttria-stabilized zirconia thermal barrier coatings, Journal of the American Ceramic Society 88 (2005) 2552-2558.
[39] H.J. Bunge. Texture analysis in materials science : mathematical methods, Butterworths, London; Boston, 1982.
[40] D.B. Williams, C.B. Carter. Transmission electron microscopy a textbook for materials science, (2009).
[41] J.X. Fu, S.Q. Turn. Characteristics and Stability of Neat and Blended Hydroprocessed Renewable Diesel, Energy & Fuels 28 (2014) 3899-3907.
[42] J. Liu, Y.J. Shi, L.P. Ma, Y. Yang. Device performance and polymer morphology in polymer light emitting diodes: The control of device electrical properties and metal/polymer contact, Journal of Applied Physics 88 (2000) 605-609.
[43] N.S. Bornstein, M.A. Decrescente. Relationship Between Compounds Of Sodium And Sulfur And Sulfidation, Transactions of the Metallurgical Society of Aime 245 (1969) 1947-&.
[44] G. Romeo, H.S. Spacil, W.J. Pasko. The Transport of Chromium in $Cr_2O_3$ Scales in Sulfidizing Environments, Journal of the Electrochemical Society 122 (1975) 1329-1333.
[45] J.A. Goebel, F.S. Pettit, G.W. Goward. Mechanisms for the hot corrosion of nickel-base alloys, Metallurgical transactions 4 (1973) 261-278.
[46] D.K. Gupta, R.A. Rapp. The Solubilities of NiO, $Co_3O_4$, and Ternary Oxides in Fused $Na_2SO_4$ at 1200°K, Journal of the Electrochemical Society 127 (1980) 2194-2202.
[47] P.D. Jose, D.K. Gupta, R.A. Rapp. Solubility of $\alpha$ - $Al_2O_3$ in Fused $Na_2SO_4$ at 1200 K, Journal of the Electrochemical Society 132 (1985) 735-737.
[48] M.L. Deanhardt, K.H. Stern. Solubility of Yttrium Oxide in $Na_2SO_4$ and NaCl Melts, Journal of the Electrochemical Society 129 (1982) 2228-2232.
[49] M.N. Task, B. Gleeson, F.S. Pettit, G.H. Meier. Compositional effects on the Type I hot corrosion of beta-NiAl alloys, Surface & Coatings Technology 206 (2011) 1552-1557.
[50] C. Leyens, I.G. Wright, B.A. Pint. Hot corrosion of nickel-base alloys by alkali-containing sulfate deposits, High Temperature Corrosion and Protection of Materials 5, Pts 1 and 2 369-3 (2001) 571-578.
[51] N. J. Simms. Solid fuel composition and power plant fuel flexibility, (2011) 3-37.
[52] A. Encinas-Oropesa, N.J. Simms, J.R. Nicholls, J.E. Oakey, L. Heikinheimo, S. Tuurna. Effect of biofuel-derived contaminants on coated industrial gas turbines blade materials, Materials and Corrosion-Werkstoffe Und Korrosion 65 (2014) 206-216.
[53] C.S. Lee, S.W. Park, S.I. Kwon. An experimental study on the atomization and combustion characteristics of biodiesel-blended fuels, Energy & Fuels 19 (2005) 2201-2208.

[54] T.G. Smagala, E. Christensen, K.M. Christison, R.E. Mohler, E. Gjersing, R.L. McCormick. Hydrocarbon Renewable and Synthetic Diesel Fuel Blendstocks: Composition and Properties, Energy & Fuels 27 (2013) 237-246.
[55] P.Y. Hsieh, J.A. Widegren, T.J. Fortin, T.J. Bruno. Chemical and Thermophysical Characterization of an Algae-Based Hydrotreated Renewable Diesel Fuel, Energy & Fuels 28 (2014) 3192-3205.
[56] M. Quinones, R. Leung, S. Williams. Algae Based Hydroprocessed Fuel Use on a Marine Gas Turbine, Journal of Engineering for Gas Turbines and Power-Transactions of the Asme 134 (2012).
[57] D.A. Shifler. Evaluating Materials and Fuels Using an Atmospheric-Pressure Low-Velocity Burner Rig, High Temperature Corrosion and Materials Chemistry 9 - a Symposium in Honor of Professor Robert a. Rapp 41 (2012) 85-102.
[58] N. Birks, G. H. Meier, F. S. Pettit. Introduction to the high-temperature oxidation of metals, Cambridge University Press, Cambridge, UK; New York, 2006.
[59] R.D. Reitz, F.V. Bracco. Mechanism of atomization of a liquid jet, Physics of Fluids 25 (1982) 1730-1742.
[60] D.M. Lipkin, J.A. Krogstad, Y. Gao, C.A. Johnson, W.A. Nelson, C.G. Levi. Phase Evolution upon Aging of Air-Plasma Sprayed t'-Zirconia Coatings: I Synchrotron X-Ray Diffraction, Journal of the American Ceramic Society 96 (2013) 290-298.
[61] J.A. Krogstad, R.M. Leckie, S. Kramer, J.M. Cairney, D.M. Lipkin, C.A. Johnson, C.G. Levi. Phase Evolution upon Aging of Air Plasma Sprayed t'-Zirconia Coatings: II-Microstructure Evolution, Journal of the American Ceramic Society 96 (2013) 299-307.
[62] A.M. Limarga, J. Iveland, M. Gentleman, D.M. Lipkin, D.R. Clarke. The use of Larson-Miller parameters to monitor the evolution of Raman lines of tetragonal zirconia with high temperature aging, Acta Materialia 59 (2011) 1162-1167.
[63] G. Di Girolamo, C. Blasi, L. Pagnotta, M. Schioppa. Phase evolution and thermophysical properties of plasma sprayed thick zirconia coatings after annealing, Ceramics International 36 (2010) 2273-2280.
[64] K. Kobayashi, H. Kuwajima, T. Masaki. Phase change and mechanical properties of $ZrO_2$-$Y_2O_3$ solid electrolyte after ageing, Solid State Ionics 3-4 (1981) 489-493.
[65] J. Chevalier, B. Cales, J.M. Drouin. Low-temperature aging of Y-TZP ceramics, Journal of the American Ceramic Society 82 (1999) 2150-2154.
[66] T. Sato, M. Shimada. Transformation of Yttria-Doped Tetragonal ZrO2 Polycrystals by Annealing in Water, Journal of the American Ceramic Society 68 (1985) 356-359.
[67] F.F. Lange, G.L. Dunlop, B.I. Davis. Degradation During Aging of Transformation-Toughened $ZrO_2$-$Y_2O_3$ Materials at 250°C, Journal of the American Ceramic Society 69 (1986) 237-240.
[68] M. Yoshimura, T. Noma, K. Kawabata, S. Somiya. Role of $H_2O$ on the degradation process of Y-TZP, Journal of Materials Science Letters 6 (1987) 465-467.
[69] D.J. Kim, H.J. Jung, D.H. Cho. Phase transformations of $Y_2O_3$ and $Nb_2O_5$ doped tetragonal zirconia during low temperature aging in air, Solid State Ionics 80 (1995) 67-73.
[70] A.E. Hughes, F.T. Ciacchi, S.P.S. Badwal. Role of $O^{2-}$, $OH^-$ and anion vacancies in the degradation of Y-TZP in moist environments, Journal of Materials Chemistry 4 (1994) 257-263.
[71] J. Chevalier, L. Gremillard, A.V. Virkar, D.R. Clarke. The Tetragonal-Monoclinic Transformation in Zirconia: Lessons Learned and Future Trends, Journal of the American Ceramic Society 92 (2009) 1901-1920.
[72] J.A. Dawson, H.R. Chen, I. Tanaka. Protonic defects in yttria stabilized zirconia: incorporation, trapping and migration, Physical Chemistry Chemical Physics 16 (2014) 4814-4822.
[73] J.A. Dawson, I. Tanaka. Proton incorporation and trapping in ZrO2 grain boundaries, Journal of Materials Chemistry A 2 (2014) 1400-1408.
[74] T. Duong, A.M. Limarga, D.R. Clarke. Diffusion of Water Species in Yttria-Stabilized Zirconia, Journal of the American Ceramic Society 92 (2009) 2731-2737.
[75] B. Scherrer, M.V.F. Schlupp, D. Stender, J. Martynczuk, J.G. Grolig, H. Ma, P. Kocher, T. Lippert, M. Prestat, L.J. Gauckler. On Proton Conductivity in Porous and Dense Yttria Stabilized Zirconia at Low Temperature, Advanced Functional Materials 23 (2013) 1957-1964.
[76] J.S. Park, Y.B. Kim, J.H. Shim, S. Kang, T.M. Gur, F.B. Prinz. Evidence of Proton Transport in Atomic Layer Deposited Yttria-Stabilized Zirconia Films, Chemistry of Materials 22 (2010) 5366-5370.
[77] B.H. Toby. EXPGUI, a graphical user interface for GSAS, Journal of Applied Crystallography 34 (2001) 210-213.
[78] G. Teufer. The crystal structure of tetragonal $ZrO_2$, Acta Crystallographica 15 (1962) 1187-&.
[79] C.J. Howard, R.J. Hill, B.E. Reichert. Structures of $ZrO_2$ polymorphs at room temperature by high-resolution neutron powder diffraction, Acta Crystallographica Section B-Structural Science 44 (1988) 116-120.

[80] P. Thompson, D.E. Cox, J.B. Hastings. Rietveld refinement of Debye–Scherrer synchrotron X-ray data from $Al_2O_3$, Journal of Applied Crystallography 20 (1987) 79-83.
[81] C.J. Howard, R.J. Hill. The polymorphs of zirconia: phase abundance and crystal structure by Rietveld analysis of neutron and X-ray diffraction data, Journal of Materials Science 26 (1991) 127-134.
[82] L.B. McCusker, R.B. Von Dreele, D.E. Cox, D. Louer, P. Scardi. Rietveld refinement guidelines, Journal of Applied Crystallography 32 (1999) 36-50.
[83] T. Sakuma, Y.I. Yoshizawa, H. Suto. The modulated structure formed by isothermal ageing in $ZrO_2$-5.2 mol % $Y_2O_3$ alloy, Journal of Materials Science 20 (1985) 1085-1092.
[84] J. Ilavsky, J.K. Stalick, J. Wallace. Thermal spray yttria-stabilized zirconia phase changes during annealing, Journal of Thermal Spray Technology 10 (2001) 497-501.
[85] J. Ilavsky, J.K. Stalick. Phase composition and its changes during annealing of plasma-sprayed YSZ, Surface & Coatings Technology 127 (2000) 120-129.
[86] D.J. Kim, H.J. Jung, I.S. Yang. Raman spectroscopy of tetragonal zirconia solid solutions, Journal of the American Ceramic Society 76 (1993) 2106-2108.
[87] D.J. Kim, J.W. Jang, H.L. Lee. Effect of tetravalent dopants on Raman spectra of tetragonal zirconia, Journal of the American Ceramic Society 80 (1997) 1453-1461.
[88] R. Chaim, A.H. Heuer, D.G. Brandon. Phase Equilibration in $ZrO_2$-$Y2O_3$ Alloys by Liquid-Film Migration, Journal of the American Ceramic Society 69 (1986) 243-248.
[89] E.J. Opila, D.S. Fox, N.S. Jacobson. Mass spectrometric identification of Si-O-H(g) species from the reaction of silica with water vapor at atmospheric pressure, Journal of the American Ceramic Society 80 (1997) 1009-1012.
[90] A.H. Heuer, R. Chaim, V. Lanteri. The displacive cubic → tetragonal transformation in $ZrO_2$ alloys, Acta Metallurgica 35 (1987) 661-666.
[91] A.H. Heuer, V. Lanteri. Crystallographic Analysis of the Cubic-to-Tetragonal Phase Transformation in the ZrO2–Y2O3 System - Comment, Journal of the American Ceramic Society 71 (1988) C170-C171.
[92] V. Lanteri, R. Chaim, A.H. Heuer. On the Microstructures Resulting from the Diffusionless Cubic→Tetragonal Transformation in $ZrO_2$-$Y_2O_3$ Alloys, Journal of the American Ceramic Society 69 (1986) C258-C261.
[93] T. Sakuma, Y. Yoshizawa, H. Suto. The metastable two-phase region in the zirconia-rich part of the $ZrO_2$-$Y_20_3$ system, Journal of Materials Science 21 (1986) 1436-1440.
[94] J.A. Munoz-Tabares, M. Anglada. Hydrothermal degradation of ground 3Y-TZP, Journal of the European Ceramic Society 32 (2012) 325-333.
[95] K. Matsui, H. Yoshida, Y. Ikuhara. Phase-transformation and grain-growth kinetics in yttria-stabilized tetragonal zirconia polycrystal doped with a small amount of alumina, Journal of the European Ceramic Society 30 (2010) 1679-1690.
[96] S. Kramer, J. Yang, C.G. Levi, C.A. Johnson. Thermochemical interaction of thermal barrier coatings with molten CaO-MgO-Al2O3-SiO2 (CMAS) deposits, Journal of the American Ceramic Society 89 (2006) 3167-3175.
[97] A.A. Nogiwa-Valdez, W.M. Rainforth, P. Zeng, I.M. Ross. Deceleration of hydrothermal degradation of 3Y-TZP by alumina and lanthana co-doping, Acta Biomaterialia 9 (2013) 6226-6235.
[98] R.D. Shannon. Revised effective ionic radii and systematic studies of interatomic distances in halides and chalcogenides, Acta Crystallographica Section A 32 (1976) 751-767.